INFORMATION TO USERS

This manuscript has been reproduced from the microfilm master. UMI films the text directly from the original or copy submitted. Thus, some thesis and dissertation copies are in typewriter face, while others may be from any type of computer printer.

The quality of this reproduction is dependent upon the quality of the copy submitted. Broken or indistinct print, colored or poor quality illustrations and photographs, print bleedthrough, substandard margins, and improper alignment can adversely affect reproduction.

In the unlikely event that the author did not send UMI a complete manuscript and there are missing pages, these will be noted. Also, if unauthorized copyright material had to be removed, a note will indicate the deletion.

Oversize materials (e.g., maps, drawings, charts) are reproduced by sectioning the original, beginning at the upper left-hand corner and continuing from left to right in equal sections with small overlaps.

Photographs included in the original manuscript have been reproduced xerographically in this copy. Higher quality 6" x 9" black and white photographic prints are available for any photographs or illustrations appearing in this copy for an additional charge. Contact UMI directly to order.

Bell & Howell Information and Learning
300 North Zeeb Road, Ann Arbor, MI 48106-1346 USA
800-521-0600

UMI®

ELECTROMAGNETIC SCATTERING BY SPHEROIDAL PARTICLES: APPLICATIONS TO THE ATMOSPHERE

A

THESIS

Presented to the Faculty

of the University of Alaska Fairbanks

in Partial Fulfillment of the Requirements

for the Degree of

DOCTOR OF PHILOSOPHY

By

Hans A. Eide, M.S.

Fairbanks, Alaska

December 2000

Bell & Howell Information and Learning Company
300 North Zeeb Road
P.O. Box 1346
Ann Arbor, MI 48106-1346

ELECTROMAGNETIC SCATTERING BY SPHEROIDAL PARTICLES: APPLICATIONS TO THE ATMOSPHERE

By

Hans A. Eide

RECOMMENDED:

Advisory Committee Chair

Department Head

APPROVED:

Dean, College of Science, Engineering and Mathematics

Dean of the Graduate School

11-27-00

Date

Abstract

An efficient and reliable method is presented for computing the expansion coefficients in the eigenfunction series representing the prolate and oblate spheroidal functions. While the traditional method is based on recurrence relations, infinite continued fractions, and a variational procedure, the new method is based on reformulating the computational task as an eigenvalue problem. In contrast with the traditional method, the new method requires no initial estimates of the eigenvalues, and the computations can be performed using readily available computer library routines. The new method is shown to produce accurate expansion coefficients for the spheroidal functions required to study scattering by particles with a wide range of shapes, sizes, and complex refractive indices [1].

In a previous study in which the scattering characteristics of Polar Stratospheric Clouds (PSCs) were calculated using randomly oriented monodispersions of prolate spheroids [2], the scattering signature of the main types of PSC particles was related to particles of a certain shape and size range. Here these results are used as a reference for testing a new method for calculating the scattering characteristics of PSC like clouds. The method is based on finding the single scattering solution for spheroids using the rigorous Separation of Variables Method (SVM), and then from it obtain the so called **T**-matrix.

The following question is addressed: Can the backscatter depolarization returns be used together with other remote sensing techniques to determine either basic shape (degree of needle- or disc-like asphericity) or size information of ice cloud particles? To this end the SVM is again utilized to obtain the T-matrix for a variety of size, shape, and size-shape distributions of ensembles of randomly oriented spheroidal particles. The results indicate that single-wavelength depolarization lidar returns are insufficient to uniquely determine both the size and the shape of the particles in an ice cloud. However, a combination of an NIR depolarization lidar and additional information obtained by complementing instruments - from which either size or shape can be estimated - has the potential for determining the mean size and shape of particles in an ice cloud.

Contents

List of Figures

List of Tables

Acknowledgements

When writing the acknowledgments there are basically two ways of doing it. One requires a lot of writing and name dropping, but will eventually make you painfully aware that you forgot someone anyway. The other is much shorter and assumes that people know where credit is due. This acknowledgment is of the latter type.

I would like to thank in particular my committee chair Knut Stamnes for giving me this opportunity. In my years working for Knut I have had a lot of interesting experiences and challenges, both through working on the projects that has become my thesis, and through numerous other projects for which I will perhaps never get a diploma, but that has taught me skills and given me experiences I wouldn't want to be without. This gratitude extends also to Knut's brother, Jakob Stamnes, my advisor during my master degree at University of Bergen, Norway, who started me on this track. I look forward to be working with both for many years to come. I would also like to thank my committee members, Brenton Watkins, Glenn Shaw, and Dave Sentman for helpful discussions, valuable inputs, and for reviewing the manuscript.

Parts of the single scattering model developed in this work incorporates routines from the separation of variables code by Shoji Asano (MRI, Japan) and Makoto Sato (NASA GISS), the T-matrix code by Michael Mishchenko (NASA GISS), and routines to glue it all together by my colleague F. Michael Kahnert (now University of Bergen, Norway). I also had the good fortune to be working with Rich L. Collins for parts of this thesis. All are gratefully acknowledged.

Special thanks go to my parents who have always been supporting me in so many ways.

To everybody else: thank you! You know who you are.

This work has been supported by the Environmental Science Division of the U.S. Department of Energy as part of the Atmospheric Radiation Measurement (ARM) program through DOE Contract 091574-A-Q1 to the University of Alaska.

Chapter 1

Introduction

With small liquid drops being the only exception, nonspherical particles "rule" in the atmosphere-ocean system. Common examples are aerosols, hydrosols, air bubbles and brine pockets in sea ice, and ice cloud particles. Accurate modeling of their light scattering properties is important for many applications of radiative transfer models and remote sensing retrieval algorithms.

Several exact and approximate theories are used in the study of light scattering by particles. For particles large compared to the wavelength of the incident light, it is customary to consider the light as rays and not as waves, and this method is generally referred to as the ray-tracing technique. In principle it is possible to study light scattering from any kind of particle with this technique provided that the particle has spatial dimensions that are large compared to the wavelength of the light. This technique goes back to Gallilei and further, but it is very much in use today, although often in a much more complicated form f.ex. [3, 4, 5, 6]. For particles small compared to the wavelength a general solution was presented by Lord Rayleigh in 1897 [7]. With this theory Lord Rayleigh was able to explain in scientific terms why the sky is blue. The particle size region between those scattering events that can be best described with Rayleigh theory and those that can be treated using ray-tracing techniques is called the resonance region. It is called the resonance region because the electromagnetic wave (the light) has a finite

number of (significant) modes that can be supported (superimposed) as steady state solutions when interacting with a particle of size comparable to the wavelength. The field that accounts for the perturbation of the incident field, i.e. the field required together with the incident field to yield the observed total field, is called the scattered field. For certain configurations, often seen for spheres or when particles are lined up in regular ways, spectacular features can become visible for our viewing pleasure. Solving the electromagnetic scattering problem in this region involves taking into account the number of ways an electromagnetic field can interact with the surface and interior of a particle. For spheres this is relatively simple because of the very simple geometry of the problem.

On the other side of the scale we have non-spherical particles for which a closed solution often does not exist at all. In 1908, only a few years after Lord Rayleigh solved the electromagnetic scattering problem for particles small compared to the wavelength, Gustaf Mie [8] solved the problem for electromagnetic scattering by spherical particles comparable to the wavelength of the incident radiation. Although the Mie theory has been put to practical use only in recent years with the advent of powerful computational tools, it is fair to say that **for spherical particles** the Rayleigh theory for light scattering by small particles and the ray-tracing technique for large particles, was bridged by the formulation of the Mie theory.

For the case of non-spherical particles the situation is much more complicated. Unfortunately, the majority of the particles in the atmosphere-ocean system (not including the molecular level) are in the resonance region for the visible and infrared wavelengths. A major portion of the Suns' radiant energy that enters our atmosphere is in the visible part of the spectrum. The earth radiates into space thermal energy in the infrared. The balance between the two determines our climate. This is why the field of electromagnetic scattering by small particles and radiative transfer has received increasing attention in the recent years.

It has been established through theoretical and laboratory studies that the scattering

and absorption characteristics of nonspherical particles are fundamentally different from those of spherical particles [9, 10, 11, 12]. Further studies show that spherical particle models are inadequate for modeling the optical properties of ice clouds and aerosol layers [9, 13]. An important question is: considering the multitude of dissimilar particles in our environment, is there a way to account for the shape as well as size in a general way? Or, put another way: It is impractical to solve the scattering problem for each individual non-spherical particle (for example every snow-flake), but, since such particles seldom make a great impact when they are alone, can we study the impact of an ensemble of such particles by using a simpler model that describe them with a few parameters, or ideally, with only one extra parameter over that needed for spheres, namely a shape parameter? Hence, in order to adequately account for particle shape in climate models and remote sensing retrieval algorithms, the development of suitable nonspherical particle models has become an important field of atmospheric research. The development of shape parameterization schemes for cirrus clouds [14] or aerosols can also greatly benefit from the development of accurate models that are based on first principles. Similar parameterization schemes could be useful for GCMs to account for different cloud radiative feedback based on cloud types. Not only climate related studies need accurate descriptions of light and energy transport in a medium containing non-spherical particles. Remote sensing applications are highly dependent on theories for non-spherical particle scattering, and analysis of depolarization lidar backscatter returns would be of little value in the absence of a firm theoretical basis for scattering by non-spherical particles.

In studies of scattering by nonspherical particles the spheroid is attractive for modeling light scattering by particles of size comparable to the wavelength of light (particles with equal radius sphere or equal area sphere size-parameters less than about 100). The reason is that the spheroidal shape can be changed from mildly aspherical to needle-like (prolate) or disk-like (oblate) by varying just one parameter, the ratio of the major to the minor axis or the aspect ratio. Therefore the spheroidal particle becomes a natural choice when one wants to extend studies of scattering phenomena from simple spherical

particles to nonspherical particles.

Several theories and models deal with the problem of scattering by spheroids [15]. In this work a new model is presented that, in analogy to the Mie theory, rigorously solves the electromagnetic scattering problem by separating the Helmholtz wave equation in the basis coordinate system and then solves the boundary value problem of matching the external and internal electromagnetic field on the surface of the particle. The basis coordinate system used is the spheroidal coordinate system. The method is commonly referred to as the Separation of Variables Method, or SVM.

In Chapter 2 the details of the method are described. Two major difficulties with this approach have prevented the use of this method earlier. The first is related to the evaluation of the expansion coefficients, or eigenvectors, needed in the eigenvalue expansion for the spheroidal radial and angular functions. The present work deals with this issue. The second stems from the difficulty in utilizing the single scattering results obtained for the spheroids with the SVM, because the spheroidal vector wave functions do not readily lend themselves to efficient orientational averaging of the scattering matrices. Schulz et al. [16] developed in work parallel to this an SVM approach that overcomes these shortcomings by using the SVM for calculating the particles' T-matrix in spheroidal coordinates. This T-matrix can then be transformed into spherical coordinates and used to calculate the ensemble-averaged optical properties analytically and thus very efficiently. How the T-matrix is obtained is reviewed briefly in Chapter 2. Chapter 2 is for the most part devoted to the problem of obtaining accurate expansion coefficients for the spheroidal eigenfunctions used in the SVM. The new method for calculating the expansion coefficients is reported here and also in Ref. [1].

Until recently very little was known about the shape-dependence of the radiance and polarization of the radiation emanating from a medium containing size-shape distributions of moderately and highly aspherical particles. It has been shown that the averaged phase function of a size-shape distribution of randomly oriented *mildly* aspherical spheroids has a smooth featureless variation with the scattering angle. It shows

none of the characteristics typical for spheres and it qualitatively resembles the phase function of natural aerosols [17]. One of the few methods efficient enough to model size-shape distributions of randomly oriented particles is the Extended Boundary Condition Method (EBCM). However, this method is limited to modeling particles that do not depart too much from spherical shape. The new SVM approach [16, 1] is capable of producing accurate results for spheroidal particles of extreme shapes, including flat oblate disks and elongated prolate needles. Since the method also provides efficient and accurate averaging over orientational angles through the use of the analytical method developed by Mishchenko [18], originally used only in connection with the EBCM, recent applications of the new SVM approach has shown that the single scattering optical properties of size-shape distributions of randomly oriented moderately and highly aspherical prolate spheroids are generally quite sensitive to variations in the effective aspect ratio of the shape-distribution [19].

Phase functions obtained with the new SVM have been published [16, 19] for size parameters up to $x = 10$, and aspect ratios up to $\epsilon = 12$. The size parameter x is defined as $x = 2\pi r_A/\lambda$, where r_A is the radius of an area-equivalent sphere, and λ is the wavelength of the incident light. The aspect ratio of a spheroid is defined as $\epsilon = a/b$ where a is the major and b is the minor axis of the spheroid. The improvements in the algorithms for computing the expansion coefficients for the prolate and oblate spheroidal eigenfunctions [1] have enabled us to extend the validity of the new SVM to larger size parameters. Examples of phase functions for ensembles of randomly oriented size distributions of moderately large spheroids with various aspect ratios are presented in Chapter 3. An important feature of these phase functions is that they are very similar to those that are often observed in nature. The assumption is that averaging over orientations, size and/or shape will smear out the characteristic features of pristine shapes. The new SVM should hence provide a useful tool for applications in which one wants to include the effect of nonsphericity for an ensemble of particles with a distribution of shapes. Then special features in the phase function of individual particles tend to be

averaged out.

In lidar studies of the atmosphere the role of nonspherical particles are of great importance. It is well known that nonspherical particles will depolarize the light from a polarized lidar beam, whereas spherical particles will not. Aside from this, information about the size and shape of the particles is carried in the lidar backscatter return since, as shown here, the backscattering from nonspherical particles varies greatly with their size, shape, and composition. Efforts have been made to develop retrieval algorithms based on the polarization lidar backscatter return. So far it seems that a single-wavelength lidar system is insufficient for providing unambiguous information about the scattering particles. The situation is further complicated by the fact that the naturally occurring clouds consist of particles of varying shape and size. Modeling efforts should therefore take into account particle size-shape distributions. A common lidar application is the study of Polar Stratospheric Clouds (PSCs). PSCs play an important role in the destruction of stratospheric ozone, especially at high latitudes. PSCs are optically thin clouds which appear regularly in the winter polar stratosphere. The crucial role of PSCs in polar ozone depletion by heterogeneous chlorine activation on the PSC particle surfaces is well known. In Chapter 4 the results of Toon et al. [2, 20] are used as a reference for testing the method for scattering by spheroidal particles presented in the previous chapters. Results for the backscatter from various size, shape, and size-shape distributions of randomly oriented spheroidal particles at different wavelengths are presented. Due to the finite gate time of the lidar instrumentation, a lidar bin will have a finite length on the order of tens of meters. A simple application in which we utilize a vector radiative transfer code together with the results for the scattering matrix of ensembles of nonspherical particles obtained earlier is presented in Chapter 4 as well.

Chapter 5 contains a summary of the findings in the present work and suggests problems for further investigation.

Chapter 2

Electromagnetic Scattering by Spheroidal Particles

The Helmholtz equation is separable in the spheroidal coordinate system, and its exact solution, which is the basis for rigorous scattering by a spheroidal particle, has been known for some time [21]. However, the exact solution of the Helmholtz equation is expressed in terms of series of eigenfunctions with coefficients that do not readily lend themselves to numerical computations. This is the major reason why the Separation of Variables Method (SVM) has not been widely used in acoustic or electromagnetic scattering by spheroids. Another reason why the SVM has been of limited use in scattering by ensembles of particles is that in the conventional use of this method [22, 23], the calculation of ensemble-averaged optical properties of size-shape distributions of randomly oriented spheroids is very inefficient and computer-time intensive. However, Schulz et al. [16] recently developed an SVM approach that overcomes these shortcomings by using the SVM for calculating the particles' T-matrix in spheroidal coordinates. The T-matrix can then be used to calculate the ensemble-averaged optical properties analytically and thus very efficiently.

This work has revitalized the question of whether the traditional method developed by Bouwkamp [24, 25] is accurate and versatile enough for automatic machine computation

of the expansion coefficients for the spheroidal functions required to study scattering by particles of extreme shapes and a wide range of sizes and refractive indices. Is it perhaps possible to develop a better method for computing the expansion coefficients? To answer this question we first point out that Stamnes and Spjelkavik [26] recently developed a new method for efficient and reliable computation of the eigenfunctions series associated with scattering by elliptical cylinders. In that case the classical method developed by Ince [27, 28, 29] was based on recurrence relations and infinite continued fractions, while the new method was based on reformulating the computational task as an eigenvalue problem. Second, we point out that the traditional method of Bouwkamp [24] for computing the expansion coefficients of the spheroidal functions is based on recurrence relations, infinite continued fractions, and a variational procedure. Thus the question arises whether we also can develop for the spheroidal functions a new computational method by reformulating the computational task as an eigenvalue problem. The answer is affirmative, and in contrast with the traditional method, the new method requires no initial estimates of the eigenvalues, and the computations can be performed using readily available computer library routines.

2.1 Introduction

A lot of work on scattering by non-spherical particles has been focused on particles with a certain geometry. The work on scattering by various versions of regular ice crystals is an example of this [30, 31, 32, 33, 34, 35]. While many of these theories are useful for special applications like explaining various types of halos or other special effects, it is much more commonly found in nature that the shapes in an ensemble of non-spherical particles are highly variable [36]. Not only that, the particles in nature are often randomly oriented as well. Such naturally occurring ensembles have been shown to yield smooth, featureless phase functions unlike the phase functions obtained for ensembles of regular shapes [37, 17]. Since it is impractical to try to account for the variation in shape by calculating the scattering properties of each shape in an ensemble individually,

it is highly desirable to achieve a good representation of the ensemble averaged optical properties by performing the single scattering calculations on a simple type of particle that has one additional parameter compared to spheres, namely a shape parameter. The spheroidal particle is one possible choice.

Several methods can be used to solve the problem of light scattering by a spheroidal particle. The two most commonly used methods are the Extended Boundary Condition Method (EBCM) and the Separation of Variables Method (SVM). The reason for this is mainly that the other methods, like the Geometric Optics Approximation (GOA) or Discrete Dipole Approximation (DDA), are restricted in their range of validity when it comes to the size of the spheroids, and, as mentioned earlier, the region of interest is often the resonance region where these methods in general are not applicable.

The EBCM is not restricted to scattering problems involving spheroids, but solves the electromagnetic scattering problem for a variety of other types of particles [38]. The EBCM produces accurate results for particles with size parameters up to about 150 depending on the particle shape. This is enough to establish a good overlap with the GOA in most cases. A problem with the EBCM is that it requires that the particles do not deviate too much from spherical shape or else the numerical calculations will become ill-conditioned. This ill-conditioning stems from the EBCM requiring that the fields in the boundary value problem be expanded in terms of Vector Spherical Wave Functions (VSWF) which are not well suited for this kind of particles. This limits the applicability of the EBCM in many cases where the scattering properties of highly aspherical particles are desired.

The SVM exploits the fact that the Helmholtz wave equation is separable in certain coordinate systems (14 in all). Examples of such coordinate systems are the spherical coordinate system (Mie theory), the infinite cylindrical or elliptical coordinate systems (2D), the cubic coordinate system, and the spheroidal coordinate system. However, the computational effort involved in this method is often quite high. For example, only in recent years did the computational algorithms involved in the Mie theory become effective

and accurate enough to be of practical use as an integral part of radiative transfer codes. This is especially true for large spheres or multi sphere (layered) configurations. Another drawback with the SVM has been that the T-matrix could not until recently be obtained from it for geometries other than the spherical one.

The solution to an electromagnetic single scattering problem is, at least for applications involving radiative transfer, most conveniently expressed in terms of the T-matrix. This is because the T-matrix greatly facilitates the computation of the optical properties of randomly oriented particles. The T-matrix is traditionally computed with the EBCM, and often the EBCM is referred to as the T-matrix Method for this reason.

The scattering problem for ensembles of particles of varying shape and/or size is normally solved in two steps. First the scattering problems for single particles representing discrete sub-sets of the different particle types of the ensemble are solved, and then the single particle solutions are used to obtain the scattering properties for the ensemble as a whole. Finding the light scattering properties of the ensemble involves an integration over particle orientations. When using the SVM this integration was traditionally done numerically which is computationally very expensive, especially for complex distributions of particles. When using the EBCM this integration can be carried out analytically using the T-matrix for particles that are axially symmetric. This method is therefore much more efficient. The integration over orientational angles yields not only the absorption and extinction coefficients of the ensemble, but also the expansion coefficients of the Stokes scattering matrix.

In work closely related to this, a new method for calculating the T-matrix for spheroidal particles was developed [16]. In this method the SVM is used to solve the electromagnetic scattering problem for a spheroidal particle. This solution is then used to find the equivalent of the T-matrix in the spherical coordinate system. We shall denote this matrix the $\mathcal{T}$-matrix with a caligraphic T in order to distinguish it from the T-matrix in spherical coordinates. A subsequent transformation of the $\mathcal{T}$-matrix into the spherical coordinate system yields the standard T-matrix. The advantage of this

approach is that the computation of the $\mathcal{T}$-matrix in the particle's natural coordinate system circumvents the ill-conditioning that hampers the EBCM approach for particles that are far from spherical. The development of a method to find the T-matrix using the SVM thus lets us combine the best part of the EBCM and the SVM: by using the SVM we avoid the ill-conditioning that arises in the EBCM when studying highly aspherical particles, while by obtaining the T-matrix we can compute the optical properties of the ensembles of randomly oriented particles more efficiently.

From the above it is obvious that the SVM scattering code consists of many complex steps. The success of the new method as a whole critically depends on the accuracy and speed of the calculations of the spheroidal functions, and accurate calculation of the expansion coefficients is a prerequisite for this step.

This chapter is organized as follows: In the first and bigger part, the SVM for spheroidal particles is presented with a strong emphasis on the new computational procedure for calculating the coefficients needed in the spheroidal eigenfunction expansions. Results are presented and discussed. In the second part the EBCM is briefly reviewed together with the method for obtaining the $\mathcal{T}$-matrix and how it subsequently can be transformed into the T-matrix. The chapter is concluded with a summary, again with an emphasis on the computational procedures developed here.

2.2 The spheroidal coordinate system

Spheroids can be constructed by rotating an ellipse around its major or minor axis. The result will be an prolate spheroid in the former case, and a oblate spheroid in the latter. By varying the ratio of the minor axis to the major axis the aspect ratio, or eccentricity, of the spheroid will vary. The size and shape of a spheroid is determined by its interfocal distance d and the eccentricity. The shape of a spheroid can thus be varied from spherical to an infinitely thin (prolate) needle or (oblate) disk. In all cases it is possible to define a spheroidal coordinate system that coincides with the particle surface.

In a prolate spheroidal system the formulas connecting Cartesian and curvilinear

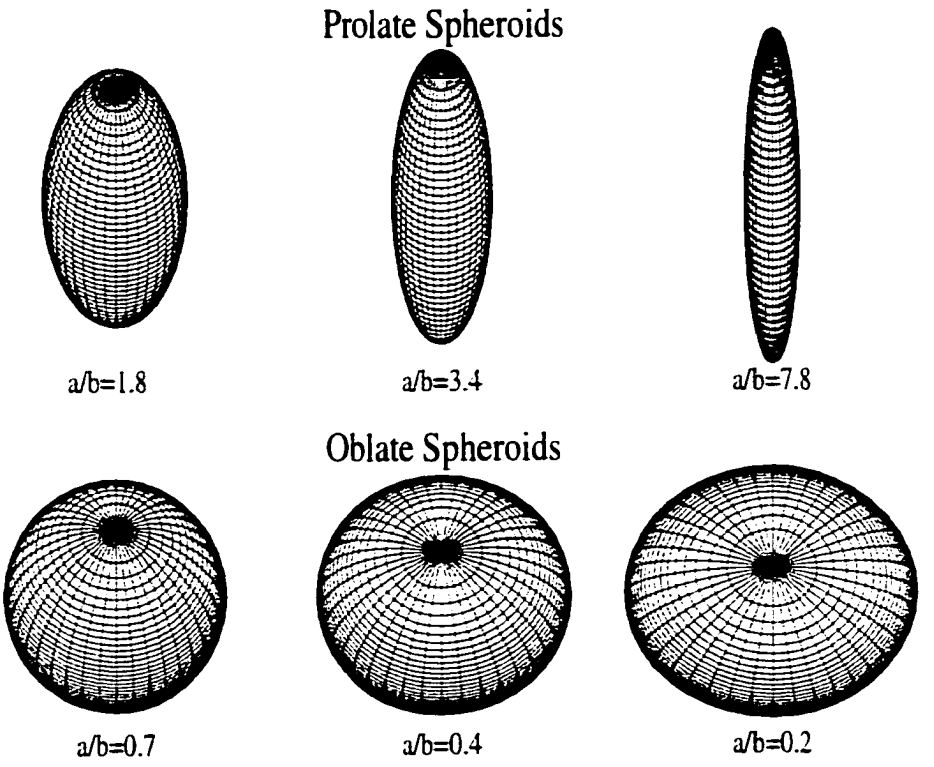

Figure 2.1. An example of spheroidal particles.

coordinates are given by

$$\begin{aligned} x &= \frac{d}{2}\left[(\xi^2-1)(1-\eta^2)\right]^{1/2}\cos\phi\,, \\ y &= \frac{d}{2}\left[(\xi^2-1)(1-\eta^2)\right]^{1/2}\sin\phi\,, \\ z &= \frac{d}{2}\,\xi\,\eta\,, \end{aligned} \tag{2.1}$$

in which d represents the inter-focal distance of the generating ellipse. The valid ranges of the variables are

$$0 \leq \phi < 2\pi\,,$$

$$1 \leq \xi < \infty , \tag{2.2}$$
$$-1 \leq \eta \leq 1 .$$

In the oblate spheroidal system the factor $(\xi^2 - 1)$ in Eq. 2.2 is replaced by $(\xi^2 + 1)$

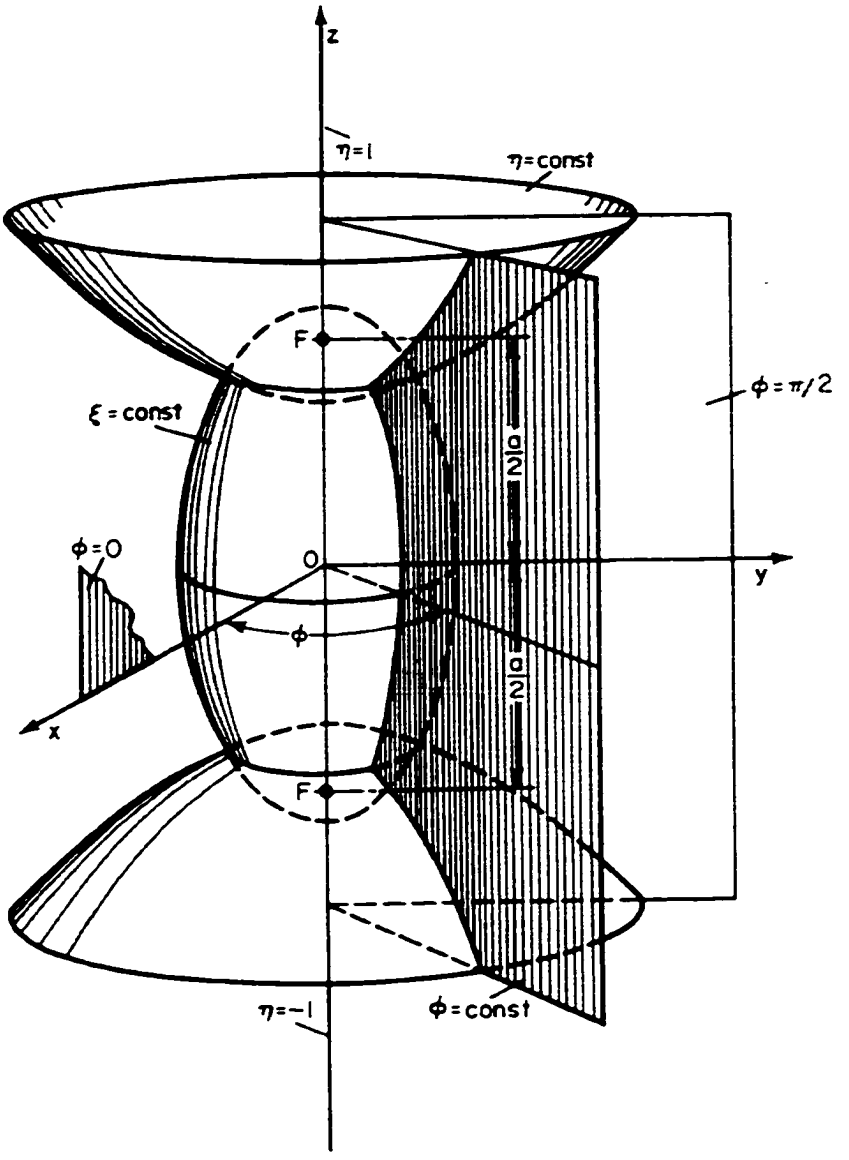

Figure 2.2. The prolate spheroidal coordinate system.

everywhere. and there is two valid ranges of the variables. These are

$$\begin{aligned} &\text{range(a)}: \qquad 0 \le \xi < \infty\ ,\ -1 \le \eta \le 1\ ,\ 0 \le \phi < 2\pi\ . \\ &\text{range(b)}: \qquad -\infty < \xi < \infty\ ,\ 0 \le \eta \le 1\ ,\ 0 \le \phi < 2\pi\ . \end{aligned} \tag{2.3}$$

In range (a) the surface $\xi = 0$ is a circular area of radius $d/2$ representing a degenerate (2D) ellipsoid located in three-dimensional space. In range (b) the quantity $\xi = 0$ corresponds to a circular hole of radius $d/2$ located in a plane infinite screen. While the first range is the one we shall use for scattering by oblate spheroidal particles. the latter is useful in diffraction problems involving circular apertures. For any finite value of the interfocal distance d. the spheroidal hypersurfaces approach spherical shape as $\xi \to \infty$. and

$$\begin{aligned} c\xi &\to kr \\ \eta &\to \cos\theta \end{aligned} \tag{2.4}$$

where (r, θ, ϕ) are spherical coordinates. The unit vectors show the following asymptotic behavior as $\xi \to \infty$

$$\begin{aligned} \hat{\xi} &\to \hat{r} \\ \hat{\eta} &\to -\hat{\theta} \end{aligned} \tag{2.5}$$

where the sign in (2.5) is due to the cosine being monotonically decreasing in the interval $0 \le \theta \le \pi$. The spheroidal hypersurfaces will also approach spherical shape as the interfocal distance goes to zero. With $\hat{r} \times \hat{\theta} = \hat{\phi}$. it follows that $(\hat{\eta}, \hat{\xi}, \hat{\phi})$ is a right-handed coordinate system, i.e. $\hat{\eta} \times \hat{\xi} = \hat{\phi}$. In both the oblate and prolate case the eccentricity. ε. is defined as the ratio of major axis, a, to the minor axis, b. In terms of the surface parameter ξ_0, i.e. the value $\xi_0 = \text{const}$ defines the surface of the spheroid, the eccentricity is given by

$$\varepsilon = \frac{\xi_0}{(\xi_0^2 - 1)^{1/2}} \qquad ; \qquad \xi_0 > 1 \tag{2.6}$$

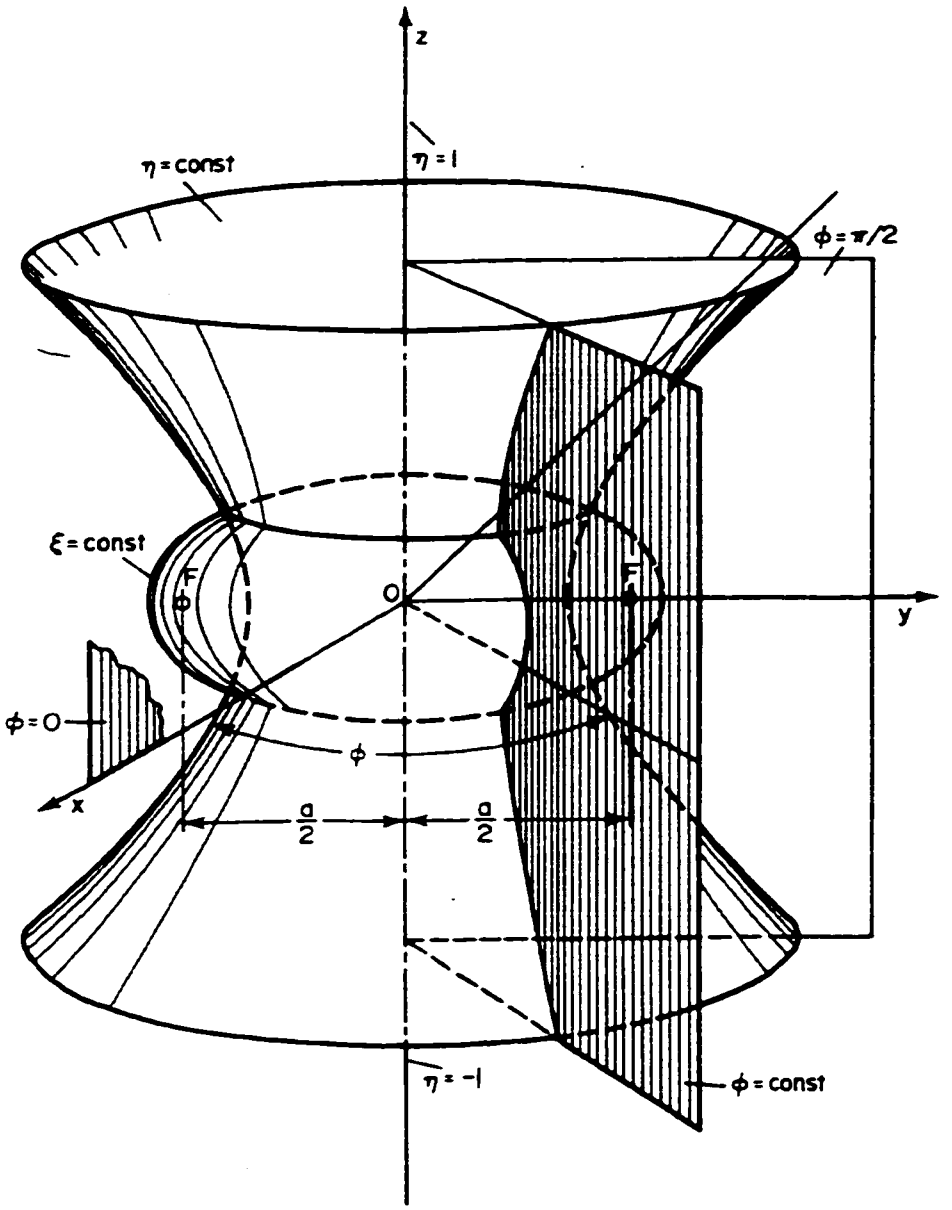

Figure 2.3. The oblate spheroidal coordinate system.

for the prolate system, and

$$\varepsilon = \frac{\xi_0}{(\xi_0^2 + 1)^{1/2}} \quad ; \quad \xi_0 > 0 \tag{2.7}$$

for the oblate system. For a more detailed description of the spheroidal coordinate system we refer to Ref. [39].

2.2.1 The Separation of Variables Method

Assuming electromagnetic wave propagation in an isotropic, homogeneous, charge-free medium, solutions to the vector wave equations

$$\nabla \mathbf{E} + k^2 \mathbf{E} = 0 \quad : \quad \nabla \mathbf{H} + k^2 \mathbf{H} = 0 \tag{2.8}$$

can be formed from the scalar wave (Helmholtz) equation $(\nabla^2 + k^2)\Psi = 0$. The parameter $k = k_0 \tilde{n}$ is the wave number with k_0 being the wave number in vacuum and $\tilde{n}$ the refractive index of the medium in which the wave is propagating. The Helmholtz equation is separable in the spheroidal coordinate system, and a set of solutions are given by [40]

$$\Psi_{m,n}(c, \eta, \xi, \phi) = S_{m,n}(c, \eta) R_{m,n}(c, \xi) \Phi_m(\phi). \tag{2.9}$$

Here m and n are integers, and η and ξ are the angular and radial spheroidal coordinates, respectively. The parameter c is given by

$$c = \frac{1}{2} k d, \tag{2.10}$$

where d is the inter-focal distance of the family of confocal ellipsoids and hyperboloids of revolution that define the spheroidal coordinate system. The azimuthal function $\Phi_m(\phi)$ is either $\cos m\phi$ or $\sin m\phi$, where $m \geq 0$, and the functions $S_{m,n}(c, \eta)$ and $R_{m,n}(c, \xi)$ are the angular and radial prolate spheroidal functions, respectively, of order m and degree n. The azimuthal function can also be expressed in terms of exponential functions, but we shall not use these here.

When solving the scattering problem for spheroids the laws of electromagnetic fields and wave propagation requires (a), that the fields are finite inside the particle, and (b), that the scattered field obey the radiation condition in the far-field, i.e. that the radiated

field converges at infinity. In practical terms this implies the use of the radial functions of the first kind inside the particles because these are finite and regular everywhere in the $c\xi$ plane, including $c\xi = 0$. By a similar argument we only need to consider the the angular functions of the first kind both inside and outside the particle. From the asymptotic behavior of the radial functions

$$R^{(1)}_{m,n}(c,\xi) \rightarrow \frac{1}{c\xi}\cos\left(c\xi - \frac{n+1}{2}\pi\right), \tag{2.11}$$

$$R^{(2)}_{m,n}(c,\xi) \rightarrow \frac{1}{c\xi}\sin\left(c\xi - \frac{n+1}{2}\pi\right), \tag{2.12}$$

$$R^{(3)}_{m,n}(c,\xi) \rightarrow \frac{1}{c\xi}\exp\left[i\left(c\xi - \frac{n+1}{2}\pi\right)\right]. \tag{2.13}$$

$$R^{(4)}_{m,n}(c,\xi) \rightarrow \frac{1}{c\xi}\exp\left[-i\left(c\xi - \frac{n+1}{2}\pi\right)\right], \tag{2.14}$$

it is seen that we need to use the radial functions of the third kind outside the spheroid since, for large distances from the spheroid, the scattered wave must approach a spherical diverging wave. But, since

$$R^{(3)}_{m,n}(c,\xi) = R^{(1)}_{m,n}(c,\xi) + iR^{(2)}_{m,n}(c,\xi), \tag{2.15}$$

we need to calculate the radial functions of the second kind as well as the radial functions of the first kind in order to obtain the radial functions of the third kind. Since the radial functions of the second kind converges very slowly for small arguments ξ one has to pay special attention to these functions [22, 39, 41, 42]. These functions are therefore also particularly sensitive to the accuracy of the expansion coefficients.

When Eq. 2.9 is substituted into the Helmholtz equation, we obtain the following differential equations for $S_{m,n}(c,\eta)$ and $R_{m,n}(c,\xi)$

$$\frac{d}{dz}\left[(1-z^2)\frac{du}{dz}\right] + \left[\lambda_{m,n} - c^2z^2 - \frac{m^2}{1-z^2}\right]u_{m,n}(c,z) = 0, \tag{2.16}$$

where $u_{m,n}(c,z)$ stands for either $S_{m,n}(c,\eta)$ or $R_{m,n}(c,\xi)$ and z correspondingly stands for either η or ξ, and where the separation constants or prolate eigenvalues $\lambda_{m,n}(c)$ are to be determined such that the solutions $u_{m,n}(c,z)$ are finite at $z = \pm 1$. Note that the angular and radial prolate spheroidal functions satisfy the same differential equation for different ranges of the variable, i.e. $-1 \leq \eta \leq 1$ and $1 \leq \xi < \infty$.

By replacing c by $-ic$ and ξ by $i\xi$ in Eq. 2.16, we get the differential equations associated with the oblate spheroidal coordinate system. The solutions are the angular and radial oblate spheroidal functions $S_{m,n}(-ic,\eta)$ and $R_{m,n}(-ic,i\xi)$ associated with the oblate eigenvalues $\lambda_{m,n}(-ic)$. The allowed ranges for the variables η and ξ are now $-1 \leq \eta \leq 1$ and $0 \leq \xi < \infty$.

We may expand the solution for $S(c,\eta)$ in a series of associated Legendre functions of the first kind with unknown expansion coefficients. The corresponding solutions are called angular spheroidal functions of the first kind. Alternatively, we may expand the solution for $S(c,\eta)$ in a series of associated Legendre functions of the second kind to obtain angular spheroidal functions of the second kind, but these functions play no role in the physical problems considered here. Hence we shall only discuss angular functions of the first kind from here on, and to simplify the terminology we call them just angular functions hereafter. The radial spheroidal functions $R(c,\xi)$ (hereafter called radial functions) may be expanded in a series of spherical Bessel or Hankel functions with the same coefficients as in the series for the angular functions. By substituting these series expansions for $S(c,\eta)$ or $R(c,\xi)$ into Eq. 2.16, we get recurrence relations between the expansion coefficients [40, 39]. It can be shown that these series expansions converge only for certain values of λ, denoted by $\lambda_{m,n}$ and called eigenvalues. We are interested only in solutions for $S(c,\eta)$ or $R(c,\xi)$ that are single-valued and finite at the poles $\eta = \pm 1$ or $\xi = \pm 1$, respectively. For this to be true the constants m and n must be integers [43]. The values of m can be restricted to be zero or positive.

The angular functions in the prolate coordinate system are given by [40, 39]

$$S_{m,n}(c,\eta) = \sum_{k=0,1}^{\infty\,\prime} d_k^{(m,n)}(c)\, P_{m+k}^{(m)}(\eta). \tag{2.17}$$

where $0 \leq m \leq n$. Here $d_k^{(m,n)}(c)$ are expansion coefficients, $P_{m+k}^{(m)}(\eta)$ are associated Legendre functions, and the primed sum extends over even (odd) indices k if $n-m$ is even (odd). Once the expansion coefficients $d_k^{(m,n)}(c)$ have been determined, they can be normalized so that

$$S_{m,n}(c,0) = P_n^{(m)}(0). \tag{2.18}$$

This is the normalization used by Flammer [39] and the explicit expression can be found in [39] or [40].

The radial functions are of four different kinds, and the function of the first kind in the prolate coordinate system is given by

$$\begin{aligned} R_{m,n}^{(1)}(c,\xi) = & \left(\sum_{k=0,1}^{\infty\,\prime} \frac{(2m+k)!}{k!} d_k^{(m,n)}(c) \right)^{-1} \left(\frac{\xi^2-1}{\xi^2} \right)^{m/2} \\ & \cdot \sum_{k=0,1}^{\infty\,\prime} i^{k+m-n} d_k^{(m,n)}(c) \frac{(2m+k)!}{k!} j_{m+k}(c\xi), \end{aligned} \tag{2.19}$$

where $j_{m+k}(c\xi)$ are the spherical Bessel functions. The normalization of the radial functions is arbitrary, but we have chosen here the normalization of Flammer [39] which ensures that the radial functions asymptotically approaches the same value as the function they are expanded in when the argument approaches infinity. The radial functions of the second kind are obtained by replacing the spherical Bessel functions in Eq. 2.19 by spherical Neumann functions, and the radial functions of the third and the fourth kind are obtained by replacing the spherical Bessel functions in Eq. 2.19 by spherical Hankel functions of the first and second kind, respectively.

In a scattering problem the parameter c in Eq. 2.17 and Eq. 2.19 is given by

$$c = \frac{1}{2} d\, k_0\, \tilde{n}, \tag{2.20}$$

where k_0 is the wave number in vacuum, and $\tilde{n}$ is either the refractive index of the homogeneous medium inside or outside the spheroidal particle. In general the refractive

index $\tilde{n}$ and hence the parameter c are complex. Thus c is real only when the particle is non-absorbing.

In Eq. 2.17 the angular prolate functions $S(c,\eta)$ of the first kind are expanded in terms of associated Legendre functions of the first kind with expansion coefficients $d_k^{(m,n)}(c)$, and in Eq. 2.19 the radial prolate functions of the first kind, $R_{m,n}^{(1)}(c,\xi)$, are expanded in terms of spherical Bessel functions $j_{m+k}(c\xi)$ with the same expansion coefficients. The angular oblate functions of the first kind are obtained by replacing c by $-ic$ in Eq. 2.17, and the radial oblate functions of the first kind are obtained by replacing c by $-ic$ and ξ by $i\xi$ in Eq. 2.19.

2.3 Expansion coefficients

Accurate determination of both the angular and radial functions depends critically on the accuracy of the expansion coefficients $d_k^{(m,n)}(c)$ in the prolate case and on $d_k^{(m,n)}(-ic)$ in the oblate case. In this section we focus on how to compute these expansion coefficients accurately, reliably, and efficiently.

2.3.1 Recurrence relations

By substituting the solution in Eq. 2.17 into the differential equation Eq. 2.16, we get the following recurrence relation between the coefficients $d_k^{(m,n)}$ in the eigenvalue problem [39, 40]

$$\alpha_k^{(m)} d_{k+2}^{(m,n)} + (\beta_k^{(m)} - \lambda_{m,n}) d_k^{(m,n)} + \gamma_k^{(m)} d_{k-2}^{(m,n)} = 0, \tag{2.21}$$

where the quantities $\alpha_k^{(m)}$, $\beta_k^{(m)}$, and $\gamma_k^{(m)}$ are given by

$$\alpha_k^{(m)} = \frac{(2m+k+2)(2m+k+1)c^2}{(2m+2k+3)(2m+2k+5)}, \tag{2.22a}$$

$$\beta_k^{(m)} = (m+k)(m+k+1) + \frac{2(m+k)(m+k+1) - 2m^2 - 1}{(2m+2k-1)(2m+2k+3)} c^2, \tag{2.22b}$$

$$\gamma_k^{(m)} = \frac{k(k-1)c^2}{(2m+2k-3)(2m+2k-1)} . \tag{2.22c}$$

This recurrence relation is a second-order difference equation with two possible non-trivial independent solutions [39]. By examining the two solutions as k tends to infinity, one finds that in one of the solutions the fraction $d_k^{(m,n)}/d_{k-2}^{(m,n)}$ increases as $-4k^2/c^2$, while it tends to zero in the other solution. The latter solution must be chosen in order to obtain a convergent series expansion for the functions. This solution enables us to obtain a transcendental equation between $\lambda_{m,n}$ and c. If we define

$$\mu_k^{(m)} = (m+k)(m+k+1) + \frac{1}{2}c^2\left(1 - \frac{4m^2-1}{(2m+2k-1)(2m+2k+3)}\right) , \ (k \geq 0) . \tag{2.23a}$$

$$\nu_k^{(m)} = \frac{k(k-1)(2m+k)(2m+k-1)c^4}{(2m+2k-1)^2(2m+2k-3)(2m+2k+1)} , \ (k \geq 2) . \tag{2.23b}$$

and combine this with Eq. 2.21 the transcendental equation for $\lambda_{m,n}$ can be written [39, 40]

$$U(\lambda_{m,n}) = U_1(\lambda_{m,n}) + U_2(\lambda_{m,n}) = 0 . \tag{2.24a}$$

where U_1 and U_2 are the infinite continued fractions

$$U_1(\lambda_{m,n}) = \mu_k^{(m)} - \lambda_{m,n} - \cfrac{\nu_k^{(m)}}{\mu_{k-2}^{(m)} - \lambda_{m,n} - \left(\cfrac{\nu_{k-2}^{(m)}}{\mu_{k-4}^{(m)} - \lambda_{m,n} - \left(\cfrac{\nu_{k-4}^{(m)}}{\mu_{k-6}^{(m)} - \lambda_{m,n} - (\cdots)}\right)}\right)} . \tag{2.24b}$$

where the last partial denominator is equal to $\mu_0^{(m)} - \lambda_{m,n}$ if $n-m$ is even and is equal to $\mu_1^{(m)} - \lambda_{m,n}$ if $m-n$ is odd, and

$$U_2(\lambda_{m,n}) = -\cfrac{\nu_{k+2}^{(m)}}{\mu_{k+2}^{(m)} - \lambda_{m,n} - \left(\cfrac{\nu_{k+4}^{(m)}}{\mu_{k+4}^{(m)} - \lambda_{m,n} - \left(\cfrac{\nu_{k+6}^{(m)}}{\mu_{k+6}^{(m)} - \lambda_{m,n} - (\cdots)}\right)}\right)} . \tag{2.24c}$$

2.3.2 Bouwkamp's method for obtaining eigenvalues and expansion coefficients

From the transcendental equation and the infinite continued fractions defined above an approximate method can be developed by which both the eigenvalues $\lambda_{m,n}$ and the corresponding coefficients $d_k^{(m,n)}(c)$ can be computed by an iterative scheme to the accuracy required. This method, which is named after Bouwkamp [24] (the method was independently developed by Blanch [44] for the similar problem involving elliptical cylinders and Mathieu functions), works as follows. First one finds an initial estimate for each eigenvalue $\lambda_{m,n}$ to be determined, either by using a power-series or an asymptotic expansion [39, 40, 41] or by reformulating the recurrence relation as an algebraic eigenvalue problem [22, 45] and solving for the eigenvalues $\lambda_{m,n}$. When $n - m$ is even, the latter approach is equivalent to finding the zeros of the determinant of the matrix

$$\begin{bmatrix}
(\beta_0^{(m)}-\lambda_m) & \alpha_0^{(m)} & 0 & 0 & \cdots & 0 & 0 & 0 \\
\gamma_2^{(m)} & (\beta_2^{(m)}-\lambda_m) & \alpha_2^{(m)} & 0 & & 0 & 0 & 0 \\
0 & \gamma_4^{(m)} & (\beta_4^{(m)}-\lambda_m) & \alpha_4^{(m)} & & 0 & 0 & 0 \\
\vdots & & & & & & & \vdots \\
0 & 0 & 0 & 0 & \cdots & \gamma_{2N-2}^{(m)} & (\beta_{2N-2}^{(m)}-\lambda_m) & \alpha_{2N-2}^{(m)} \\
0 & 0 & 0 & 0 & \cdots & 0 & \gamma_{2N} & (\beta_{2N}-\lambda_m)
\end{bmatrix} \tag{2.25}$$

where the matrix has been truncated to the size $N \times N$. By setting the determinant of this matrix equal to zero, we obtain N different solutions for $\lambda_{m,n}$, namely the eigenvalues $\lambda_{m,0}$, $\lambda_{m,2}$, $\lambda_{m,4}$, $\cdots$, $\lambda_{m,2N-2}$, $\lambda_{m,2N}$. Each of these eigenvalues corresponds to a particular eigenvector or set of coefficients. Thus for each value of n, where $n = 0, 2, 4, \cdots, 2N-2, 2N$, we have $d_0^{m,n}$, $d_2^{m,n}$, $d_4^{m,n}$, ... $d_{2N-2}^{m,n}$, $d_{2N}^{m,n}$.

In practice the value of N is determined by the number of terms required in order to get a desired accuracy in the summation over even values of k in the series expansion in Eq. 2.17 for the angular function or in the series expansion in Eq. 2.19 for the radial function. In general N should be chosen larger than the truncation number in the expansions to ensure that the computed estimate of each eigenvalue $\lambda_{m,n}$ is not influenced

too much by the truncation of the infinite eigenvalue problem. It turns out that one needs to extend the eigenvalue problem by only a few terms in order to get good accuracy for the first N eigenvalues. This algebraic approach for finding initial estimates for the eigenvalues was used by Asano et al. [10. 22].

Once good initial estimates for $\lambda_{m.n}$ have been found. Bouwkamp's iterative procedure can be applied. It consists of obtaining a correction $\delta\lambda_{m.n}$ to an approximate value $\lambda_{m.n}^{(1)}$ of the eigenvalue $\lambda_{m.n}$, i.e.

$$\lambda_{m.n} = \lambda_{m.n}^{(1)} + \delta\lambda_{m.n} . \tag{2.26}$$

Using the transcendental equation (cf. Eq. 2.24a) this can be rewritten as [40]

$$\delta\lambda_{m.n} = \frac{U_1(\lambda_{m.n}^{(1)}) + U_2(\lambda_{m.n}^{(1)})}{\Delta_1 + \Delta_2} . \tag{2.27}$$

where

$$\Delta_1 = 1 + \frac{\nu_k^{(m)}}{(B_k^{(m)})^2} + \frac{\nu_k^{(m)}\nu_{k-2}^{(m)}}{(B_k^{(m)}B_{k-2}^{(m)})^2} + \frac{\nu_k^{(m)}\nu_{k-2}^{(m)}\nu_{k-4}^{(m)}}{(B_k^{(m)}B_{k-2}^{(m)}B_{k-4}^{(m)})^2} + \cdots . \tag{2.28a}$$

$$\Delta_2 = \frac{(B_{k+2}^{(m)})^2}{\nu_{k+2}^{(m)}} + \frac{(B_{k+2}^{(m)}B_{k+4}^{(m)})^2}{\nu_{k+2}^{(m)}\nu_{k+4}^{(m)}} + \frac{(B_{k+2}^{(m)}B_{k+4}^{(m)}B_{k+6}^{(m)})^2}{\nu_{k+2}^{(m)}\nu_{k+4}^{(m)}\nu_{k+6}^{(m)}} + \cdots . \tag{2.28b}$$

and

$$B_k^{(m)} = \frac{(2m+k)(2m+k-1)c^2}{(2m+2k-1)(2m+2k+1)} \frac{d_k^{(m.n)}}{d_{k-2}^{(m,n)}} \; (k \geq 2) . \tag{2.28c}$$

The factors $B_k^{(m)}$ are found by iteration of

$$B_{k+2}^{(m)} = \mu_k^{(m)} - \lambda_{m.n} - \frac{\nu_k^{(m)}}{B_k^{(m)}} . \tag{2.29a}$$

where

$$B_2^{(m)} = \mu_0^{(m)} - \lambda_{m,n} \; ; \; B_3^{(m)} = \mu_1^{(m)} - \lambda_{m.n} . \tag{2.29b}$$

Once the quantities $B_n^{(m)}$ in (2.29b) have been determined, the ratios between coefficients can be found using

$$\frac{d_0^{(m,n)}}{d_{2k}^{(m,n)}} = \left(\frac{d_0^{(m,n)}}{d_2^{(m,n)}}\right)\left(\frac{d_2^{(m,n)}}{d_4^{(m,n)}}\right)\cdots\left(\frac{d_{2k-2}^{(m,n)}}{d_{2k}^{(m,n)}}\right) . \tag{2.30a}$$

$$\frac{d_1^{(m,n)}}{d_{2k+1}^{(m,n)}} = \left(\frac{d_1^{(m,n)}}{d_3^{(m,n)}}\right)\left(\frac{d_3^{(m,n)}}{d_5^{(m,n)}}\right)\cdots\left(\frac{d_{2k-1}^{(m,n)}}{d_{2k+1}^{(m,n)}}\right) . \tag{2.30b}$$

in combination with Eq. 2.29a. The corrected eigenvalue $\lambda_{m,n}^{(1)} + \delta\lambda_{m,n}$ determined in this manner is in general closer to the true value $\lambda_{m,n}$. Once good eigenvalues have been determined, the coefficients or eigenvectors are found by repeated use of the recurrence relation in Eq. 2.21 within an arbitrary constant, which can be determined by the use of a suitable normalization, such as that given in Ref. [39].

This traditional iterative procedure works well as long as one is able to compute accurate initial estimates for the eigenvalues. If the initial estimate for an eigenvalue is inaccurate, the iteration scheme may converge to the wrong eigenvalue, and the final set of eigenvalues and associated coefficients will then be erroneous. Sinha et al. [41] overcame this problem by utilizing an algorithm that calculates a starting value by successive extrapolation from eigenvalues computed without an initial guess.

2.3.3 The new approach

Our new procedure is well adapted to automatic machine computation, since it requires no initial estimates of the eigenvalues $\lambda_{m,n}(c)$ to be determined. Also, the procedure is reliable and accurate, and based on readily available computer library routines. The new procedure is simply based on realizing that the recurrence relation in Eq. 2.21 can be used to reformulate the computational task as an *algebraic eigenvalue problem*. The solution of the corresponding algebraic eigenvalue problem yields not only *the eigenvalues*, but also *the required eigenvectors*. Truncation at N terms gives the following eigenvalue

problem if $n - m$ is even (cf. Eq. 2.25)

$$\begin{bmatrix} (\beta_0^{(m)}-\lambda_m) & \alpha_0^{(m)} & 0 & 0 & \cdots & 0 & 0 & 0 \\ \gamma_2^{(m)} & (\beta_2^{(m)}-\lambda_m) & \alpha_2^{(m)} & 0 & & 0 & 0 & 0 \\ 0 & \gamma_4^{(m)} & (\beta_4^{(m)}-\lambda_m) & \alpha_4^{(m)} & & 0 & 0 & 0 \\ \vdots & & & & & & & \vdots \\ 0 & 0 & 0 & 0 & \cdots & \gamma_{2N-2}^{(m)} & (\beta_{2N-2}^{(m)}-\lambda_m) & \alpha_{2N-2}^{(m)} \\ 0 & 0 & 0 & 0 & \cdots & 0 & \gamma_{2N}^{(m)} & (\beta_{2N}^{(m)}-\lambda_m) \end{bmatrix} \begin{bmatrix} d_0^m \\ d_2^m \\ d_4^m \\ \vdots \\ d_{2N-2}^m \\ d_{2N}^m \end{bmatrix} = 0. \tag{2.31}$$

which by means of available software packages can be accurately solved provided the value of N is of reasonable size. Thus by solving the tridiagonal matrix eigenvalue problem in Eq. 2.31, we obtain the eigenvalues *as well as* the corresponding eigenvectors (coefficients). The solution can be obtained by applying standard computer library routines, such as the LAPACK library routines [46], for solving algebraic eigenvalue problems. These routines are readily available and can be applied also to complex-valued matrices.

Wang et al. [45] did not use Bouwkamp's method to determine the eigenvalues, but found them by considering the corresponding algebraic eigenvalue problem, i.e. by requiring that the determinant of the matrix in Eq. 2.25 be zero. Then they used these eigenvalues to find the expansion coefficients by the repeated use of the recurrence relations. Hence Wang et al. did not solve the full algebraic eigenvalue problem to obtain the eigenvectors (coefficients) as we do. Rather, as Asano et al. [22], they required the determinant of the matrix in Eq. 2.25 to vanish and assumed the eigenvalues so obtained to be accurate enough. Wang et al. obtained reasonable values for optical properties of realistic spheroids using this method. Since their method for obtaining the eigenvalues is mathematically equivalent to ours, and since the use of recurrence relations to find the eigenvectors is in principle equivalent to solving the eigenvalue problem for the eigenvectors, the results of Wang et al. for optical properties give an indication of the kind of results we can expect to obtain with our method. However, little is known about the

accuracy they obtained for the expansion coefficients and their computational precision.

2.4 Numerical results for the expansion coefficients

It is of interest to compare results obtained by our new method with results obtained by another independent approach for real and complex values of c. However, benchmark results for eigenvalues and angular and radial functions are available only for purely real or purely imaginary values of c [47, 48]. Also, these results are for absolute values of c less than 40. Our first tests therefore were limited to purely real and purely imaginary values of c for which Hanish et al. [47] and van Buren et al. [48] at Naval Research Laboratories (NRL) have published extensive tables of radial and angular functions for values of $|c|$ in the range $0.1 \leq |c| \leq 40.0$ and for $m = 0, 1, 2, 3$. The NRL computer programs employed for generating the benchmark tables of radial and angular functions [49, 50, 51] contain routines that make use of Bouwkamp's method for finding eigenvalues and coefficients. The initial estimates for the eigenvalues are found in the same way as in the code by Asano et al. [22] by requiring the determinant of the matrix in Eq. 2.25 to vanish. Comparisons of eigenvalues obtained by the NRL routines with eigenvalues obtained by our routines revealed agreement up to the computational limit of precision. The NRL tables do not contain coefficients, but we have compared results for the coefficients obtained with our code with corresponding results obtained with the NRL code and found good agreement.

Next we replaced the parts of the original NRL routines for computing eigenvalues and coefficients with our routines described in Section 2.3 and compared the resulting output for the angular functions and the radial functions of the first and second kind with tabulated NRL values as well as with corresponding output from the original, unmodified NRL routines. These comparisons showed excellent agreement up to the limit set by our computer. The calculations were done in double precision on a 64 bit workstation. For the radial functions of the first and second kind and their derivatives one can determine

the accuracy of the calculated values by use of the Wronskian

$$R_{m,n}^{(1)}(c,\xi)\frac{dR_{m,n}^{(2)}}{d\xi} - R_{m,n}^{(2)}\frac{dR_{m,n}^{(1)}}{d\xi} = \frac{1}{c(\xi^2-1)}. \tag{2.32}$$

Checking our calculations in this way we found that we in general obtained the same order of accuracy as reported in Refs. [47] and [48]. This method is not used in the following numerical tests as computations of functions are not considered.

Some discrepancies where observed for the radial functions of the second kind for all values of c and small arguments. These are attributed to the fact that the radial functions of the second kind converge very slowly for small arguments $c\xi$ (if at all), and even very small differences between the eigenvectors will be magnified. Sinha et al. [42] has developed an integral method which completely overcomes this problem.

The original NRL program and the one we modified for use with our method takes about the same computing time, but as mentioned above, the original NRL program can only handle purely real or purely imaginary values of c.

For complex values of c we conducted tests by comparing our results with results obtained with the code of Asano et al. [10, 22]. In this code the same methods as in the NRL code are used for finding the eigenvalues and the eigenvectors, but it can be used also for complex values of c. For absolute values of c larger than about 50, the code implemented by Asano et al. [10, 22] for finding initial estimates for the eigenvalues (by requiring the determinant of the matrix in Eq. 2.25 to vanish) breaks down. For further comparisons between the two codes, the code by Asano et al. [10, 22] must be modified. The results of this comparison are summarized in Figure 2.4 which shows the largest relative difference between eigenvalues obtained with our method and with the code of Asano et al. [22, 10]. For each value of $|c|$ and m the relative eigenvalue difference is plotted for that value of n, $m \leq n \leq m + 100$, which gives the largest relative difference. Excellent agreement between the two methods is found for values of $|c|$ less than about 50. In this plot the value of the complex refractive index $\tilde{n}$ in Eq. 2.20 was set to $1.33 + 0.05i$. We have set the value of the wave number in vacuum equal to

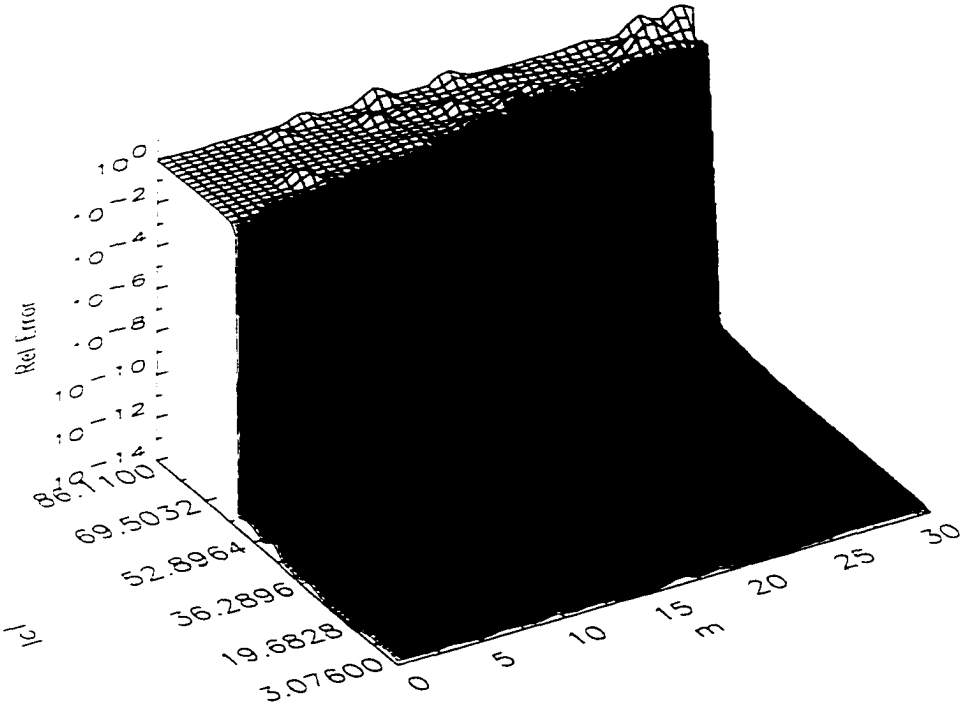

Figure 2.4. Comparison of eigenvalues found by our method and by Bouwkamp's method as implemented by Asano et al. [10, 22]. For each value of $|c|$ and m the relative eigenvalue difference is plotted for that value of n, $m \leq n \leq m + 100$ which gives the largest relative difference. For values of $|c|$ larger than about 50, the original code of Asano et al. [10, 22] breaks down. For values of $|c|$ less than 50, excellent agreement is obtained for all values of m and n.

$k_0 = 2\pi$, which means that distances are measured in units of the wavelength in vacuum. The inter-focal distance d varies from about 0.7 to 20.6 in this figure. For the case of a needle-like prolate or disk-like oblate particle this corresponds to particles with about the same length or diameter, respectively. The size-parameter can only be determined when the surface of the spheroid has been chosen by setting it at a fixed radial distance ξ_0.

In a second test we used our eigenvalue method to obtain starting values for Bouwkamp's iterative procedure, and then we checked for what values of $|c|$ the iterative refinement

of the eigenvalues would be significant. To test if the accuracy of the method has any dependence on the magnitude of the imaginary part of the refractive index. we chose three different complex refractive indices with the same real part, but with a large variation in the imaginary part. For a complex refractive index of $\tilde{n} = 1.33 + 0.05i$ and a 100×100 eigenvalue matrix the eigenvalues found by our method would start to be altered by Bouwkamp's iterative refinement when the absolute value of c got larger than about 160. For larger values of $|c|$ our solution did not converge using this matrix size. But an absolute value for c of 160 drastically increases the allowable range compared with that reached by earlier investigators. With an eigenvalue matrix size of 70×70 and the same refractive index we obtained convergence for absolute values of c up to about 130. and with an eigenvalue matrix size of 50×50 we obtained convergence for absolute values of c up to about 75. Examples of results obtained with different values for the imaginary part of the refractive index are shown in Figures 2.5 - 2.7. From these figures it follows that there is no significant difference between the eigenvalues obtained with our method and those that are obtained through the additional refinement by Bouwkamp's method as long as the matrix is large enough to give convergence when solving the eigenvalue problem. Thus additional refinement of the eigenvalues by the use of Bouwkamp's iterative procedure is unnecessary as long as the matrix is sufficiently large to give convergence. In each of the Figures 2.5 - 2.7 the matrix size is 100×100. but the imaginary part of the refractive index has a value of 0.005 in Figure 2.5. a value of 0.05 in Figure 2.6, and a value of 0.1 in Figure 2.7. As these results indicate by having about the same limit of convergence, we conclude that the method is insensitive to the size of the imaginary part of the refractive index.

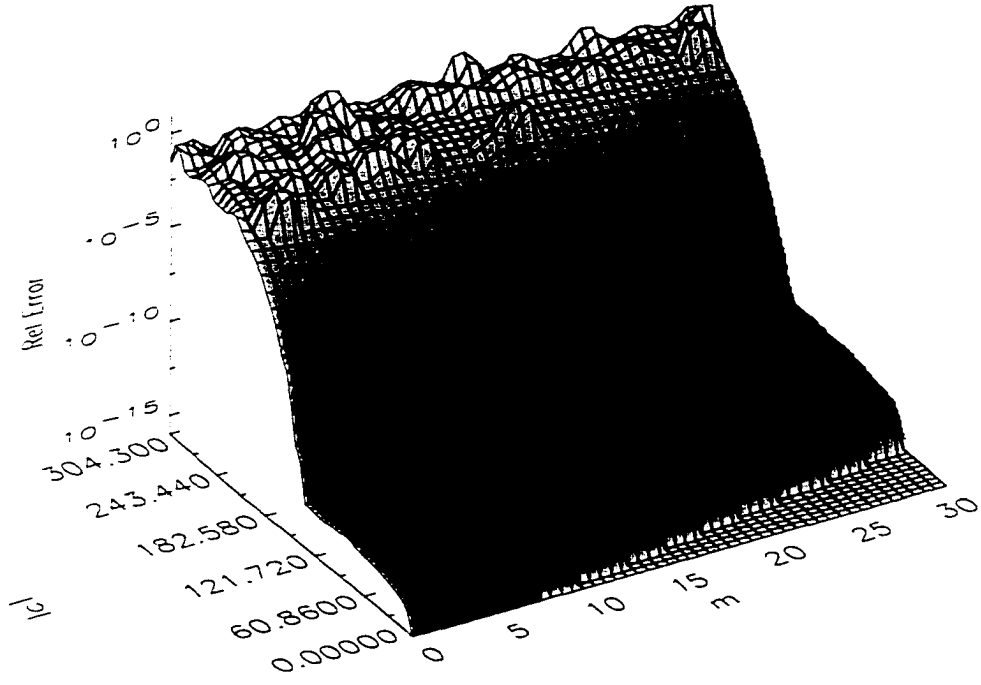

Figure 2.5. Comparison of eigenvalues found by our method and the same eigenvalues after additional refinement by Bouwkamp's method. For each value of $|c|$ and m the relative eigenvalue difference is plotted for that value of n which gives the largest relative difference. In this plot the value of the complex refractive index $\tilde{n}$ in Eq. 2.20 was set to $1.33 + 0.005i$. We used a 100×100 eigenvalue matrix, and for values of $|c|$ larger than about 160 convergence is no longer obtained in either case.

2.5 The boundary value problem

From the solutions of the scalar wave equation the following solutions to even or odd vector wave equations can be formed [22, 39]

$$\begin{aligned} \mathbf{M}_{p,m.n} &= \nabla \times (\mathbf{r} \cdot \psi_{p,m,n}) , \\ \mathbf{N}_{p,m,n} &= k^{-1} \cdot \nabla \times \mathbf{M}_{p,m,n} , \end{aligned} \tag{2.33}$$

where the vector $\mathbf{r}$ is the position vector, and $p = e, o$ denotes even or odd functions.

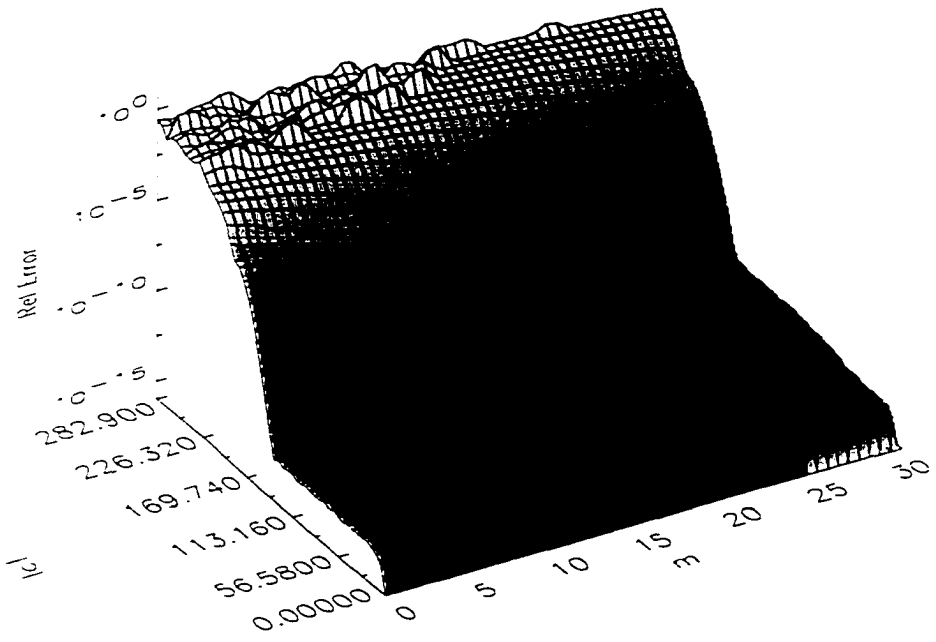

Figure 2.6. Comparison of eigenvalues found by our method and the same eigenvalues after additional refinement by Bouwkamp's method. For each value of $|c|$ and m the relative eigenvalue difference is plotted for that value of n which gives the largest relative difference. In this plot the value of the complex refractive index $\tilde{n}$ in Eq. 2.20 is here $1.33 + 0.05i$, and a 100×100 eigenvalue matrix was used.

respectively. The vectors $\mathbf{M}_{p,m,n}$ and $\mathbf{N}_{p,m,n}$ are solenoidal, and the electromagnetic field vectors $\mathbf{E}$ and $\mathbf{H}$ can be expressed in infinite series of them. A spheroidal particle in a coordinate system with the z-axis coinciding with the particle's symmetry axis, and a polarized plane wave incident in the x-z plane at an angle ζ with the z-axis. The electric field vector is either in the incident plane (TM mode) or perpendicular to it (TE mode). The electric field of the incident plane wave in the TE mode is given by

$$\mathbf{E}^i = \sum_{m=0}^{\infty} \sum_{n=m}^{\infty} i^n [f_{n,m}^{(2)}(\zeta)\, \mathbf{M}_{e,n,m}^{(1)}(k_2\mathbf{r}) + i f_{n,m}^{(1)}(\zeta)\, \mathbf{N}_{o,n,m}^{(1)}(k_2\mathbf{r})], \qquad (2.34)$$

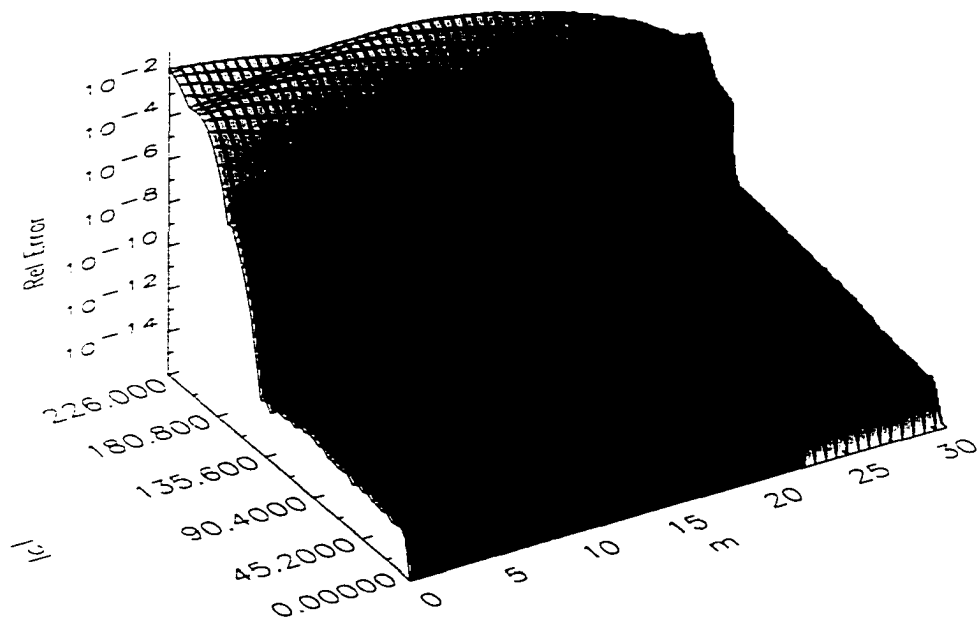

Figure 2.7. Comparison of eigenvalues found by our method and the same eigenvalues after additional refinement by Bouwkamp's method. For each value of $|c|$ and m the relative eigenvalue difference is plotted for that value of n which gives the largest relative difference. In this plot the value of the complex refractive index $\tilde{n}$ in Eq. 2.20 is $1.33+0.1i$. i.e. a very high absorption. Again a 100×100 eigenvalue matrix was used. Convergence is no longer obtained in this case as well for values of $|c|$ around 160.

and the corresponding field in the TM mode is

$$\mathbf{E}^i = \sum_{m=0}^{\infty} \sum_{n=m}^{\infty} i^n [f_{n,m}^{(1)}(\zeta)\, \mathbf{M}_{o,n,m}^{(1)}(k_2\mathbf{r}) - i f_{n,m}^{(2)}(\zeta)\, \mathbf{N}_{e,n,m}^{(1)}(k_2\mathbf{r})]. \tag{2.35}$$

The plane wave expansion coefficients are [22, 52]:

$$f_{n,m}^{(1)}(\zeta) = \frac{4m}{N_{m,n}} \sum_{r=0,1}^{\infty\prime} \frac{d_r^{(m,n)}}{(r+m)(r+m+1)} \frac{P_{m+r}^{(m)}(\cos\zeta)}{\sin\zeta} \tag{2.36}$$

$$f_{n,m}^{(2)}(\zeta) = \frac{2(2-\delta_{0,m})}{N_{m,n}} \sum_{r=0,1}^{\infty\prime} \frac{d_r^{(m,n)}}{(r+m)(r+m+1)} \frac{dP_{m+r}^{(m)}(\cos\zeta)}{d\zeta}. \tag{2.37}$$

The scattered and internal field in the TE mode are given by

$$\mathbf{E}^s = \sum_{m=0}^{\infty}\sum_{n=m}^{\infty} i^n[\pi^{(2)}_{1,n,m}\,\mathbf{M}^{(3)}_{e,n,m}(k_2\mathbf{r}) + i\pi^{(1)}_{1,n,m}\,\mathbf{N}^{(3)}_{o,n,m}(k_2\mathbf{r})]. \qquad \xi > \xi_0. \tag{2.38}$$

$$\mathbf{E}^{int} = \sum_{m=0}^{\infty}\sum_{n=m}^{\infty} i^n[\chi^{(2)}_{1,n,m}\,\mathbf{M}^{(1)}_{e,n,m}(k_1\mathbf{r}) + i\chi^{(1)}_{1,n,m}\,\mathbf{N}^{(1)}_{o,n,m}(k_1\mathbf{r})]. \qquad \xi < \xi_0. \tag{2.39}$$

and in the TM mode by

$$\mathbf{E}^s = \sum_{m=0}^{\infty}\sum_{n=m}^{\infty} i^n[\pi^{(1)}_{2,n,m}\,\mathbf{M}^{(3)}_{o,n,m}(k_2\mathbf{r}) - i\pi^{(2)}_{2,n,m}\,\mathbf{N}^{(3)}_{e,n,m}(k_2\mathbf{r})]. \qquad \xi > \xi_0. \tag{2.40}$$

$$\mathbf{E}^{int} = \sum_{m=0}^{\infty}\sum_{n=m}^{\infty} i^n[\chi^{(1)}_{2,n,m}\,\mathbf{M}^{(1)}_{o,n,m}(k_1\mathbf{r}) - i\chi^{(2)}_{2,n,m}\,\mathbf{N}^{(1)}_{e,n,m}(k_1\mathbf{r})]. \qquad \xi < \xi_0. \tag{2.41}$$

where $k_j = k_0\tilde{n}_j$ $(j = 1, 2)$ with k_0 being the wave number in vacuum and n_1 and n_2 being the complex refractive indices inside and outside the particle, respectively. $\xi = \xi_0$ is the coordinate hypersurface coinciding with the surface of the spheroidal particle. Similar relations can be written for the magnetic field [22].

The problem is to compute the unknown constants of integration in the expansions (2.38) - (2.41) by using the boundary conditions for the electric field

$$E^i_\eta + E^s_\eta = E^{int}_\eta \qquad \text{at } \xi = \xi_0, \tag{2.42}$$

$$E^i_\phi + E^s_\phi = E^{int}_\phi \qquad \text{at } \xi = \xi_0, \tag{2.43}$$

and analogous conditions for the magnetic field [22]. The boundary conditions have to be expressed explicitly in terms of the spheroidal wave functions. This yields a system of linear equations for each value of the index m of the form

$$\mathbf{A}_k(m)\cdot\mathbf{x}_k(m) = \mathbf{b}_k(m), \qquad k = 1, 2 \tag{2.44}$$

and

$$\begin{aligned}\mathbf{x}_k(m) &= [\pi^{(1)}_{k,m,m}, \pi^{(1)}_{k,m+1,m}, \ldots, \pi^{(2)}_{k,m,m}, \pi^{(2)}_{k,m+1,m}, \ldots, \\ &\quad \chi^{(1)}_{k,m,m}, \chi^{(1)}_{k,m+1,m}, \ldots, \chi^{(2)}_{k,m,m}, \chi^{(2)}_{k,m+1,m}, \ldots]^T \end{aligned} \tag{2.45}$$

is the vector of the unknown coefficients for the TE ($k = 1$) and the TM mode ($k = 2$), and where both the coefficient matrix $\mathbf{A}_k(m)$ and the inhomogeneity $\mathbf{b}_k(m)$ depend on the coefficients $d_r^{(m,n)}(c)$ and the radial spheroidal wave functions of the first and third kind at $\xi = \xi_0$, $R^{(j)}_{n,m}(c;\xi_0)$, and their derivative $dR^{(j)}_{n,m}(c;\xi)/d\xi|_{\xi=\xi_0}$. The solution of the electromagnetic scattering problem is obtained by solving Eq. 2.44 for each value of m and for both modes. Equation Eq. 2.44 can be found in explicit form in the paper by Asano and Yamamoto [22], which also includes a discussion of the numerical implementation of this system of linear equations and ways to avoid numerical ill-conditioning.

2.6 The Extended Boundary Condition Method

When using the EBCM to solve the problem of scattering by a single particle, one expands the incident, scattered, and internal fields in vector spherical wave functions (VSWF)

$$\mathbf{E}^{inc}(\mathbf{R}) = \sum_{n=1}^{\infty} \sum_{m=-n}^{n} [a^{(1)}_{n,m}\, \mathbf{M}^{(1)}_{n,m}(k_2\mathbf{R}) + a^{(2)}_{n,m}\, \mathbf{N}^{(1)}_{n,m}(k_2\mathbf{R})]\,. \tag{2.46}$$

$$\mathbf{E}^{sca}(\mathbf{R}) = \sum_{n=1}^{\infty} \sum_{m=-n}^{n} [p^{(1)}_{n,m}\, \mathbf{M}^{(3)}_{n,m}(k_2\mathbf{R}) + p^{(2)}_{n,m}\, \mathbf{N}^{(3)}_{n,m}(k_2\mathbf{R})] \quad : \quad |R| > R_>\,. \tag{2.47}$$

$$\mathbf{E}^{int}(\mathbf{R}) = \sum_{n=1}^{\infty} \sum_{m=-n}^{n} [b^{(1)}_{n,m}\, \mathbf{M}^{(1)}_{n,m}(k_1\mathbf{R}) + b^{(2)}_{n,m}\, \mathbf{N}^{(1)}_{n,m}(k_1\mathbf{R})]\,, \tag{2.48}$$

where k is the wave number as before, and $R_>$ is the radius shown in Figure 2.8 of the smallest circumscribing sphere of the scattering particle centered at the origin of the coordinate system. These VSWF are defined in a similar way as the vector spheroidal

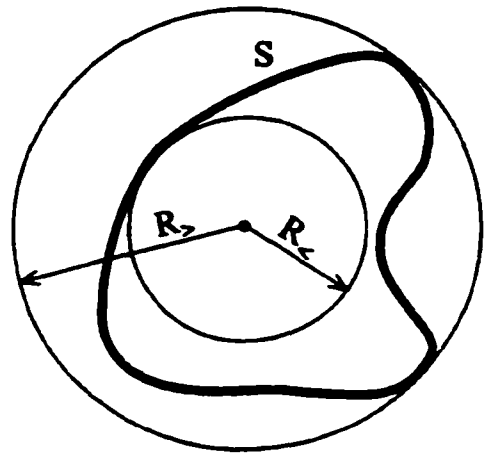

Figure 2.8. Illustration of the concept of the EBCM.

wave functions, i.e. to obtain the vector spherical functions, one has to replace the scalar spheroidal wave functions by the scalar spherical wave functions $\psi_{n,m}$ given by

$$\psi^{(j)}_{n,m} = P^{(m)}_n(\cos\theta) z^{(j)}_n(kr) \mathrm{e}^{im\phi}, \qquad j = 1,\ldots,4 \tag{2.49}$$

where the $z^{(1)}_n$ and $z^{(2)}_n$ denote spherical Bessel and Neumann functions, respectively, while $z^{(3)}_n$ and $z^{(4)}_n$ denote n^{th} order spherical Hankel functions of the first and second kind, respectively. The EBCM takes advantage of the fact that Maxwell's equations and the boundary conditions are linear. There must therefore be a linear relation between the expansion coefficients in Eqs. 2.46, 2.47, and 2.48. For the case of $\mathbf{E}^{sca}$ and $\mathbf{E}^{inc}$ this can be written as

$$p^{(k)}_{n,m} = \sum_{n'=1}^{\infty} \sum_{m'=-n'}^{n'} \sum_{k'=1}^{2} T^{(k,k')}_{n,m,n',m'} a^{(k')}_{n',m'}, \tag{2.50}$$

with similar expressions for the relation between the coefficients of the other fields. If written in compact matrix-vector notation 2.50 becomes

$$\mathbf{p} = \mathbf{T} \cdot \mathbf{a} \tag{2.51}$$

where $\mathbf{T}$ is called the T-matrix.

The next step of the EBCM involves using an integral-equation approach for deriving the matrices relating the fields [53, 54, 55, 56, 57]. The resulting expressions are then integrated over the particle's surface with the cross products of the vector spherical functions. These surface integrals are usually evaluated numerically. The EBCM has been applied to nonspherical particles of different shapes, such as spheroids [11, 18, 58], finite circular cylinders [12, 59], and Chebyshev particles [18]. A matrix inversion needed to obtain the T-matrix tends to become ill-conditioned for nonspherical particles much larger than a wavelength or with large real or imaginary parts of the refractive index [38], as well as for non-absorbing or weekly absorbing particles [60], and for highly aspherical particles. Recent progress in numerical procedures, however, has made it possible to extend the applicability of the EBCM to size parameters larger than 150 for both non-absorbing and weakly absorbing particles [60], and for small particles with highly aspherical shape [61].

2.7 The $\mathcal{T}$-matrix in spheroidal coordinates

The $\mathcal{T}$-matrix in spheroidal coordinates is obtained in a way analogous to the method for obtaining the T-matrix in spherical coordinates. Again, this is possible because Maxwell's equations and the boundary conditions are linear, and there must therefore be a linear relation between the expansions of the fields also for the spheroidal coordinate system. From Eq. 2.50 we see that we can write

$$\pi_{nm}^{k} = \sum_{n'=0}^{\infty} \sum_{m'=-n'}^{n'} \sum_{k'=1}^{2} \mathcal{T}_{nmn'm'}^{kk'} \alpha_{n'm'}^{k'}. \tag{2.52}$$

The major difference is that instead of choosing plane waves as incident waves, we now use waves expanded with the coefficients

$$(\alpha_{nm}^{k})_i = \delta_{nn_i} \delta_{mm_i} \delta_{kk_i}, \tag{2.53}$$

for the i^{th} incident wave. These waves might not have any obvious physical meaning, but

the analogy to the impulse-response method is interesting. Now we obtain from Eq. 2.52

$$\mathcal{T}^{kk_j}_{nmn_jm_j} = (\pi^k_{nm})_j. \tag{2.54}$$

What we have done is to employ the SVM for a different set of incident waves, i.e. the incident wave is not a plane wave, and have thus obtained the $\mathcal{T}$-matrix in spheroidal coordinates as using the SVM solution.

For more detail on this subject we refer to Ref. [16].

2.8 Transformation of the $\mathcal{T}$-matrix into the T-matrix

As described above, the advantage of the T-matrix is that it greatly facilitates orientational averaging of the particles. The next step is therefore to obtain the T-matrix by transforming the $\mathcal{T}$-matrix in spheroidal coordinates into spherical coordinates. The transformation can be derived using the expansion of angular spheroidal functions in terms of associated Legendre functions [16]. The result is of the form

$$\begin{aligned} T^{kk'}_{n_1mn_2m} &= i^{n_1-n_2}\sqrt{\frac{n_1(n_1+1)}{n_2(n_2+1)}} \\ &\times \sum_{n,n'} \sqrt{\frac{N_{mn}}{N_{mn'}}}\, i^{n'-n}\, f^{mn}_{n_1-|m|}(c)\, f^{mn'*}_{n_2-|m|}(c)\, \mathcal{T}^{kk'}_{nmn'm}. \end{aligned} \tag{2.55}$$

where N_{mn} denotes the normalization constant of the angular spheroidal functions, and the factors f^{mn}_r are related to their expansion coefficients. The explicit form of the factors f^{mn}_r are given in Ref. [39]. In compact vector matrix notation Eq. 2.56 can be written

$$\mathbf{T} = \mathbf{G}\cdot\mathcal{T}\cdot\mathbf{H}. \tag{2.56}$$

Having performed this transformation we can directly compare the T-matrix calculated with our modified SVM to the one obtained with the EBCM. Such tests have been carried out in Ref. [16]. We are now ready to use our T-matrix to analytically calculate optical properties of randomly oriented particles in connection with the well-established procedure for analytic averaging over orientation.

2.9 Summary

We have shown that an alternative to Bouwkamp's method exists for computing expansion coefficients for spheroidal functions. The new method is based on using the recurrence relation between the expansion coefficients for spheroidal functions to reformulate the problem of finding eigenvalues and eigenvectors (expansion coefficients) as an algebraic eigenvalue problem. The eigenvalue problem is solved by the use of readily available computer library routines.

When combined with the recent work of Schultz et al. [16] in which a method based on the SVM for spheroidal particles was developed for efficient computation of ensemble-averaged optical properties, we believe that this new method for computing spheroidal functions can be of great value in future work concerned with modeling of electromagnetic scattering by size-shape distributions of nonspherical particles.

Above we presented results obtained with a 100×100 eigenvalue matrix. Using single precision complex variables and double precision real variables on a standard workstation and a 400×400 eigenvalue matrix, we have recently obtained accurate results for the expansion coefficients of spheroidal functions for absolute values of c up to about 280. The method has been shown to be insensitive to the magnitude of imaginary part of the refractive index.

In principle one can find the eigenvalues $\lambda_{m,n}$ and the corresponding eigenvectors (expansion coefficients) for any desired c provided one has access to resources that allow one to solve an eigenvalue problem large enough to ensure convergence of the method. The remaining challenge is to develop more accurate schemes for calculating the radial spheroidal functions of the second kind when ξ is small.

Chapter 3

Phase functions for ensembles of randomly oriented spheroids

In Chapter 2 we developed a new method for computing the optical properties of ensembles of randomly oriented spheroidal particles. Thus, we are now in a position to study the effect of particle shape on radiative processes. Here we compare the phase functions obtained with traditional Mie theory and those obtained with the new method for various types of distributions. The Separation of Variables Method (SVM) can handle particles with shapes that deviates significantly from the sphere. Results for ensembles containing such particles are presented here. The results show that the phase functions of ensembles containing needle-like or disk-like particles closely resembles the phase functions of natural aerosols [17], and also that the most extreme of these shapes have unique scattering properties similar to those previously reported only in Ref. [61]. In Ref. [61] the phase functions of needle-like and disk-like particles are reported as being close to the phase functions of surface equivalent spheres. Our results show larger differences for the same phase functions, but like in Ref. [61], we find that needle-like and disk-like particles have asymmetry parameters close to those of surface equivalent spheres. and that the other optical parameters resembles those of particles small compared to the wavelength, i.e. particles scattering in the Rayleigh regime. This result may have important implications

for remote sensing and optical particle sizing. We vary the width of the particle distributions in order to study the effect of particle diversity on the optical properties. As the particle diversity increases, features often seen in the phase function of more uniform distributions tend to get washed out. Variation in particle shape has a greater impact on the phase functions than variation in particle size in this respect.

3.1 Introduction

Until recently very little was known about the shape-dependence of the radiance and polarization in a medium containing size-shape distributions of moderately and highly aspherical particles. Results indicate that spheroids with extreme aspect ratios may have scattering properties dramatically different from those of moderately aspherical particles [19, 62]. It has been shown that the averaged phase function of a size-shape distribution of randomly oriented *mildly* aspherical spheroids has a smooth featureless variation with the scattering angle [17]. These phase functions show none of the characteristics typical for spheres and it qualitatively resembles the phase function of natural aerosols. One of the few methods efficient enough to model size-shape distributions of randomly oriented particles is the Extended Boundary Condition Method (EBCM). The EBCM has traditionally been limited to modeling particles that do not depart too much from spherical shape. Recently however, improvements of the T-matrix method has extended its range of validity considerably [15, 63]. The new SVM approach that has been developed [1, 16] is capable of producing accurate results for spheroidal particles of extreme shapes, including flat oblate disks and elongated prolate needles. This method can also provide efficient and accurate averaging over orientational angles through the use of an analytical method developed by Mishchenko [18] and originally used only in connection with the EBCM. A recent application of the new SVM approach has shown that the single scattering optical properties of size-shape distributions of randomly oriented moderately and highly aspherical small prolate spheroids are generally quite sensitive to variations in the effective aspect ratio of the shape-distribution [19].

Phase functions obtained with the new SVM have been published [16, 19] for size parameters up to $x = 10$, and aspect ratios up to $\epsilon = 12$. Here we present previously unpublished results for particle size parameters up to $x = 30$ and aspect ratios up to $\epsilon = 20$. The size parameter x is defined as $x = 2\pi r_A/\lambda$, where r_A is the radius of an area or volume equivalent sphere, and λ is the wavelength of the incident light. The choice of whether to characterize the size of the non-spherical particles in terms of equal volume or equal area spheres should depend on the amount of absorption in the particles. If the particles have little or no absorption, then the scattered field will largely be due to the discontinuity of the refractive index across the particle surface. On the other hand, if the particle absorption is substantial, then the volume of the particles might be of greater importance and one should chose the volume equivalent representation. Not all investigators seem to adhere to this principle. The aspect ratio of a spheroid is defined as $\epsilon = a/b$ where a is the major and b is the minor axis of the spheroid. Improvements in the algorithms for computing the expansion coefficients for the prolate and oblate spheroidal eigenfunctions [1] have enabled us to extend the validity of the new SVM to larger size parameters as well as to more extreme shapes.

An important feature with the phase functions obtained for ensembles of randomly oriented spheroidal particles is that they are very similar to those that are often observed in nature. The assumption is that averaging over orientations, size and/or shape will smear out the characteristic features of the individual shapes. The new SVM should hence provide a useful tool for applications in which one wants to include the effect of non-sphericity without paying attention to special features in the phase function of individual particles.

In this Chapter examples of phase functions and the linear polarization for various distributions of randomly oriented spheroids with various aspect ratios are presented. We consider monodispersions, size distributions, shape distributions, and size-shape distributions. Results of Mie calculations for distributions of comparable spherical particles are presented alongside the results for the distributions of spheroids where applicable.

In the next Chapter we use the SVM to study the effect of distributions of spheroidal particles on the backscatter, and, in conjunction with a vector radiative transfer code, we model the expected LIDAR returns from a stratospheric cirrus cloud consisting of an ensemble of such particles.

3.2 Theory

The electric field vector of monochromatic plane electromagnetic wave incident upon a particle in the direction of $\mathbf{n}^{inc}$ can be written as

$$\begin{aligned} \mathbf{E}^{inc}(\mathbf{R}) &= \mathbf{E}_0^{inc} \exp(ik\,R\,\mathbf{n}^{inc}) \\ &= E_\theta^{inc}\theta^{inc} + E_\phi^{inc}\phi^{inc}. \end{aligned} \tag{3.1}$$

where $k = 2\pi/\lambda$ is the wavenumber of the incident wave in the surrounding medium, and $\mathbf{R}$ is the radius vector with the origin at the laboratory reference frame. The quantities $E_\theta\theta$ and $E_\phi\phi$ are the transverse electric field components in, and perpendicular to, a plane through the laboratory z-axis and the direction of the beam, respectively. The time-factor $\exp(-i\omega t)$ has been suppressed. Because of the linearity of the Maxwell's equations and the boundary conditions, it is always possible to express the scattered electromagnetic field,

$$\mathbf{E}^{sca}(\mathbf{R}) = E_\theta^{sca}(R, \mathbf{n}^{sca})\theta^{sca} + E_\phi^{sca}(R, \mathbf{n}^{sca})\phi^{sca} \quad : \quad \mathbf{n}^{sca} = \frac{\mathbf{R}}{R}. \tag{3.2}$$

by a linear transformation of the incident field. In the far-field region, where the scattered wave becomes spherical, this transformation can be written

$$\begin{bmatrix} E_\theta^{sca} \\ E_\phi^{sca} \end{bmatrix} = \frac{\exp(ikR)}{R}\,\mathbf{S}(\mathbf{n}^{sca} : \mathbf{n}^{inc} : \alpha, \beta, \gamma) \begin{bmatrix} E_{\theta_0}^{inc} \\ E_{\phi_0}^{inc} \end{bmatrix}. \tag{3.3}$$

where $\mathbf{S}$ is the 2×2 amplitude (scattering) matrix. This amplitude matrix linearly transforms the electric field components of the incident wave to the electric field vectors

of the scattered wave. The amplitude matrix depends on the directions of incidence and the direction of scattering. It also depends on the size, shape, and composition of the scattering particle, and on its orientation with respect to the laboratory frame as specified by the Euler angels of rotation α, β, and γ.

It is now convenient to introduce the so-called Stokes parameters. A monochromatic transverse electromagnetic wave can be described by four quantities $[I, U, Q, V]$ that are such that

$$\begin{aligned} I &= E_\theta E_\theta^* + E_\phi E_\phi^*, \\ Q &= E_\theta E_\theta^* - E_\phi E_\phi^*, \\ U &= -E_\theta E_\phi^* - E_\phi E_\theta^*, \\ V &= i(E_\theta E_\phi^* - E_\phi E_\theta^*), \end{aligned} \tag{3.4}$$

where the asterix denotes the complex conjugate. The Stokes parameters have units of energy per unit area per unit time per unit wavelength. The parameter I is equal to the energy flux of the wave, Q and U describe the state of linear polarization of the wave, and V describe the state of circular polarization of the wave. Having defined the Stokes parameters we can describe an electromagnetic wave by its Stokes vector

$$\mathbf{I} = \begin{bmatrix} I \\ Q \\ U \\ V \end{bmatrix}. \tag{3.5}$$

If the wave is a coherent, plane monochromatic wave then we also have $I^2 \equiv Q^2 + U^2 + V^2$, but in general $I^2 \geq Q^2 + U^2 + V^2$ [3]. The degree of polarization is defined as $P = [Q^2 + U^2 + V^2]^{1/2}/I \leq 1$, the degree of linear polarization as $P_L = [Q^2 + U^2]^{1/2}/I \leq 1$, and the degree of circular polarization as $P_C = V/I \leq 1$. It follows from this that for unpolarized (natural) light we have $Q = U = V = 0$. These quantities should not be confused with the linear backscatter *depolarization ratio*, δ_L, and the circular backscatter *depolarization ratio*, δ_C, discussed in more detail in the next chapter.

From the above definitions we can now reformulate the expression for a spherical wave scattered from a single particle as

$$\begin{aligned} \mathbf{I}^{sca} &= \frac{1}{R^2}\mathbf{Z}(\mathbf{n}^{sca}:\mathbf{n}^{inc}:\alpha,\beta,\gamma)\,\mathbf{I}^{inc} \\ &= \frac{1}{R^2}\mathbf{Z}(\theta^{sca},\phi^{sca},\theta^{inc},\phi^{inc};\alpha,\beta,\gamma)\,\mathbf{I}^{inc}. \end{aligned} \tag{3.6}$$

where $\mathbf{Z}$ is the 4×4 phase matrix. Explicit expressions for its elements $Z_{1,1}\cdots Z_{4,4}$ can be found in for example Ref. [3]. The phase matrix is normalized such that integrating $Z_{1,1}$ over all directions yields 1. The orientationally averaged phase matrix $<\mathbf{Z}(\mathbf{n}^{sca}:\mathbf{n}^{inc})>$ is independent of the Euler angles, and can be constructed from any combination of particles, e.g. particles with varying size, shape, and composition, as long as the single scattering phase matrix for each particle is known.

By definition, the *phase* matrix relates the Stokes parameters of the incident and scattered beams defined relative to their respective meridional planes, e.g. defined in respect to the propagation vector of the incoming and scattered beam and the laboratory z-axis, respectively. The *scattering* matrix $\mathbf{F}$ relates the Stokes parameters of the incident and scattered beams defined with respect to the scattering plane, e.g. the plane through $\mathbf{n}^{inc}$ and $\mathbf{n}^{sca}$. An easy way to convert from the scattering matrix to the phase matrix is to direct the laboratory z-axis along the direction of propagation for the incident beam ($\theta = 0$) and let the plane with $\phi^{inc} = \phi^{sca} = 0$ be in the scattering plane. Because of symmetry, the scattering matrix $\mathbf{F}$ for macroscopically isotropic and symmetric media is invariant with respect to the choice of the scattering plane and depends only on the angle between the incident and scattered beams. Let the scattering angle in this system be Θ, then

$$\mathbf{F}(\Theta) = \frac{4\pi}{C_{sca}} < \mathbf{Z}(\Theta,0;0,0) >. \tag{3.7}$$

where the C_{sca} is the scattering cross section per particle, i.e.

$$C_{sca} = 2\pi \int_0^{\pi} d\Theta \,\sin\Theta \, < Z_{1,1}(\Theta,0;0,0) > . \tag{3.8}$$

The factor $4\pi/C_{sca}$ follows from the normalization of the phase function. For macroscopically isotropic and symmetric media the scattering cross section is independent of the direction and polarization of the incident beam. Likewise. the extinction cross section is also independent of the direction and polarization of the incident beam. and thereby so is also the absorption cross section $C_{abs} = C_{ext} - C_{sca}$. Another useful quantity is the single scattering albedo

$$\omega = \frac{C_{sca}}{C_{ext}}. \tag{3.9}$$

which is the probability that a photon incident on a small volume element of the scattering media will survive the scattering incident instead of being absorbed.

In a macroscopically isotropic and symmetric media the scattering matrix has the well known form [3]

$$\mathbf{F}(\Theta) = \begin{bmatrix} F_{1,1}(\Theta) & F_{1,2}(\Theta) & 0 & 0 \\ F_{1,2}(\Theta) & F_{2,2}(\Theta) & 0 & 0 \\ 0 & 0 & F_{3,3}(\Theta) & F_{3,4}(\Theta) \\ 0 & 0 & -F_{3,4}(\Theta) & F_{4,4}(\Theta) \end{bmatrix}. \tag{3.10}$$

so that in this case only eight of the elements of the scattering matrix are non-zero. The phase matrix in Eq. 3.10 is the phase matrix applicable to ensembles of randomly oriented spheroids. Further more, for the special cases of the scattering angles 0 and π we have

$$\begin{aligned} F_{2,2}(0) = F_{3,3}(0) \quad ; \quad F_{2,2}(\pi) = -F_{3,3}(\pi)\,. \\ F_{1,2}(0) = F_{3,4}(0) = F_{1,2}(\pi) = F_{3,4}(\pi) = 0\,. \\ F_{4,4}(\pi) = F1,1(\pi) - 2F_{2,2}(\pi)\,. \end{aligned} \tag{3.11}$$

In addition, rotationally symmetric particles have [64]

$$F_{4,4}(0) = 2F_{2,2}(0) - F_{1,1}(0). \tag{3.12}$$

The element $F_{1,1}(\Theta)$ of the scattering matrix is called the phase *function.* It satisfies the normalization condition

$$\frac{1}{4\pi}\int_{4\pi} d\mathbf{n}^{sca}\, F_{1,1}(\Theta) \;=\; \frac{1}{2}\int_{0}^{\pi} d\Theta\, sin\Theta\, F_{1,1}(\Theta) \;=\; 1. \tag{3.13}$$

The phase function relates the scattered field intensity to the incident field intensity. The element $F_{2,2}$ relates the corresponding Stokes vector Q-components to one another, and the element $F_{3,4}$ constitutes the linear relation between the U and V components of the incident and scattered field.

Lastly, the quantity

$$g \;=<\cos\Theta>\;=\; \frac{1}{2}\int_{-1}^{1} d\cos\Theta\, F_{1,1}\, \cos\Theta\,, \tag{3.14}$$

is called the asymmetry factor of the phase function. It is positive for particles that scatter predominantly in the forward direction, negative for predominantly backscattering particles, and zero for particles with a symmetric (isotropic) phase function.

3.3 Modeling phase matrices

The next four sub-sections contains four figures each with examples of results obtained for the phase functions of different kinds of distributions. To give an overview of the figures we have listed them in Table 3.1.

The spheroids considered here will have low absorption, i.e. the values of the imaginary part of the refractive index is small. We shall therefore characterize their size by the radius of an area-equivalent sphere. For the form of the size distribution, a power-law distribution is assumed:

$$n_{size}(r) \;=\; \begin{cases} C & : \; r \le r_1 \\ C\,(r_1/r)^3 & : \; r_1 \le r \le r_2 \\ 0 & : \; r > r_2 \end{cases} \tag{3.15}$$

Table 3.1. Overview of figures in Chapter 3.

Fig. no.	Distrib. type	Aspect rat. ε_{eff}	Shape var. var. $\mu_{eff}(\%)$	Size parameter parameter r_{eff}	Size ν_{eff}	Refractive index
3.1	mono	2	0	1.1, 2.0, 10, 20	0	$1.31 + i6.1 \times 10^{-9}$
3.2	mono	2	0	1.1, 2.0, 10, 20	0	$1.31 + i6.1 \times 10^{-9}$
3.3	mono	30	0	0.91, 0.67, 0.5, 0.25	0	$1.33 + i0.005$
3.4	mono	30	0	0.91, 0.67, 0.5, 0.25	0	$1.33 + i0.005$
3.5	size	2	0	1.1, 2.0, 10, 20	0.1	$1.31 + i6.1 \times 10^{-9}$
3.6	size	2	0	1.1, 2.0, 10, 20.	0.1	$1.31 + i6.1 \times 10^{-9}$
3.7	size	8	0	0.91, 0.5, 0.33, 0.25	0.1, 0.05, 0.01	$1.31 + i6.1 \times 10^{-9}$
3.8	size	8	0	0.91, 0.5, 0.33, 0.25	0.1, 0.05, 0.01	$1.31 + i6.1 \times 10^{-9}$
3.9	shape	2	5, 10	1.1, 2.0, 10, 20	0	$1.31 + i6.1 \times 10^{-9}$
3.10	shape	2	5, 10	1.1, 2.0, 10, 20	0	$1.31 + i6.1 \times 10^{-9}$
3.11	shape	10	5, 10	0.91, 0.5, 0.125, 0.1	0	$1.31 + i6.1 \times 10^{-9}$
3.12	shape	10	5, 10	0.91, 0.5, 0.125, 0.1	0	$1.31 + i6.1 \times 10^{-9}$
3.13	size-shape	2	5	1.1, 2.0, 6.0, 12.0	0.1	$1.31 + i6.1 \times 10^{-9}$
3.14	size-shape	2	5	1.1, 2.0, 6.0, 12.0	0.1	$1.31 + i6.1 \times 10^{-9}$
3.15	size-shape	10	5	0.91, 0.5, 0.125, 0.1	0.1	$1.31 + i6.1 \times 10^{-9}$
3.16	size-shape	10	5	0.91, 0.5, 0.125, 0.1	0.1	$1.31 + i6.1 \times 10^{-9}$

where r is the area-equivalent sphere radius. The constant C is chosen such that

$$\int_0^\infty dr\, n_{size}(r) \;=\; 1. \tag{3.16}$$

A size distribution can be characterized [65] by its effective radius

$$r_{eff} \;=\; \frac{1}{G}\int_0^\infty dr\, r\pi r^2 n_{size}(r)\,, \tag{3.17}$$

and its effective variance

$$\nu_{eff} \;=\; \frac{1}{r_{eff}^2 G}\int_0^\infty dr\,(r - r_{eff})^2\,\pi r^2 n_{size}(r)\,. \tag{3.18}$$

where the averaged cross sectional area is

$$G \;=\; \int_0^\infty dr\,\pi r^2 n_{size}(r). \tag{3.19}$$

The parameters r_1 and r_2 in (3.15) can be expressed in terms of r_{eff} and ν_{eff}.

A spheroid can be characterized by its major and minor axes a and b. Alternatively, the aspect ratio $\epsilon = a/b$ determines the shape of the spheroid. Little information is available about the quantitative distribution of shapes in natural cirrus clouds or aerosol layers. The description of such natural shape-distributions is complicated by the multitudes of irregular shapes. It is impossible to exactly describe a natural shape-distribution as one would have to account for every individual shape. Here we use shape-distributions of spheroidal particles that will be described by only one parameter, namely the aspect ratio $\epsilon = a/b$. Such shape distributions is ideal for modeling purposes, and it is a natural extension of the in many cases over-simplified spherical particle model. The form of the shape distributions are adapted from Mishchenko's work [66], hence we assume an equiprobable distribution of the aspect ratio

$$n_{shape}(\epsilon) = \begin{cases} C & : \ \epsilon_1 \leq \epsilon \leq \epsilon_2 \\ 0 & : \ \text{otherwise} \end{cases} \tag{3.20}$$

where $C = 1/(\epsilon_2 - \epsilon_1)$. The effective aspect ratio ϵ_{eff} and effective variance μ_{eff} of the equiprobable shape distribution are defined as

$$\epsilon_{eff} = \frac{\epsilon_1 + \epsilon_2}{2}. \tag{3.21}$$

$$\mu_{eff} = \frac{\epsilon_1 - \epsilon_2}{2}. \tag{3.22}$$

In this investigation we first vary the size distribution while keeping the shape-distribution constant. Next we vary the shape distribution while keeping the size distribution constant. Lastly we vary both parameters at the same time to model the effect on the optical single-scattering properties of size-shape distributions.

3.3.1 Monodispersions

The two first figures, Figures 3.1 and 3.2, show the phase function, $-F_{1,2}/F_{1,1}$, and $F_{2,2}/F_{1,1}$ for ensembles of randomly oriented monodisperse prolate spheroids with equal

area sphere size parameter $x = 2$. The refractive index is $1.31 + i6.1 \times 10^{-9}$, i.e. that of pure ice at 603 nm wavelength. The dotted line in Figure 3.1 corresponds to the phase function for a monodispersion of spherical particles with the same radius and refractive index. One thing to notice is that the phase function for the spheroids changes from that of a sphere to a more featureless, or flat, phase function very quickly as the aspect ratio is increased. The result is a decrease in the asymmetry parameter g with increasing aspect ratio. In Figure 3.2 the solid lines corresponds to the linear polarization, or $-F_{1,2}/F_{1,1}$. In the upper left panel the dotted lines is the linear polarization for spherical particles. (For spheres $F_{2,2} = F_{1,1}$, so $F_{2,2}/F_{1,1}$ is always 1 and is not included.) The linear polarization curves are very close to those obtained for particles in the Rayleigh region, i.e. at 90° scattering angle an unpolarized incident beam is almost completely polarized. This effect is seen to increase with increasing aspect ratio except for the very highest aspect ratios. On the other hand, for the very highest aspect ratios the value of $F_{2,2}/F_{1,1}$ (dashed line) has become significant around 90°. This indicates that polarized light will get depolarized in this direction. The value of the backscatter depolarization, δ_L, is indicated in each panel. Because these particles are small compared to the wavelength of the incident light they do not have any significant backscatter depolarization.

In the following two figures, Figures 3.3 and 3.4, we have increased the size parameter to 30. The ensembles now consists of monodispersions of randomly oriented oblate spheroids with a refractive index of $1.33 + i0.005$, typical for slightly "dirty" atmospheric ice particles at $0.55\mu m$. The phase functions for various aspect ratios are shown in Figure 3.3. Again the phase function changes from one similar to that of a sphere to a more featureless, or flat, phase function very quickly as the aspect ratio is increased. Already at an aspect ratio of $\epsilon \sim 2$ the typical features of the spherical counterpart are absent. The corresponding Mie calculations are shown for comparison as the dotted lines. An interesting feature is the "lump", similar to a rainbow effect, that is apparent for the moderate aspect ratios. The feature is no longer present for particles with aspect ratio greater than 0.25. Features like this are only observed for monodispersions of

spheroids. This is an argument for using polydispersions when using scattering code in atmospheric applications. In Figure 3.4 we again show plots of $F_{2,2}/F_{1,1}$ and $F_{1,2}/F_{1,1}$ as a function of scattering angle. Note the extreme oscillating behavior of $F_{1,2}/F_{1,1}$ for the Mie calculations (dotted line in upper left panel). Since the particles in these figures are rather big we now have a significant backscatter depolarization as indicated by the δ_L values in the figure. The more extreme shapes are able to significantly depolarize in a wide range around the backscatter direction whereas the linear polarization is modest.

3.3.2 Size distributions

Figure 3.5 shows the phase function for a size distribution of randomly oriented oblate spheroids for various aspect ratios. We have used the power law distribution with an effective size parameter of 2, and an effective variance of 0.1. The dotted line corresponds to a similar distribution of spheres. The refractive index of the particles is $1.31 + i6.1 \times 10^{-9}$. As would be expected, the introduction of a size distribution leads to a featureless, flat phase function. Increasing aspect ratio leads to lower asymmetry parameters. The corresponding angular behavior of $F_{1,2}/F_{1,1}$ and $F_{2,2}/F_{1,1}$ is shown in Figure 3.6. Note again how the more extreme aspect ratios leads to features approaching those of Rayleigh scattering particles.

In Figures 3.7 and 3.8 we have size distributions of randomly oriented oblate spheroids. We have included lines for three different values of the effective size variance ν_{eff}. The solid lines corresponds to $\nu_{eff} = 0.1$, the dashed lines to $\nu_{eff} = 0.05$, and the dash-dotted lines to $\nu_{eff} = 0.01$. The phase function is not very sensitive to the width of the size distributions. There are more differences between the distributions in Figure 3.8, especially for $F_{1,2}/F_{1,1}$ for near spherical particles, and $F_{2,2}/F_{1,1}$ for the more extreme particles.

3.3.3 Shape distributions

As evident from the preceding figures, the elements of the scattering matrix are highly sensitive to the particle aspect ratio. One expects that when using shape distributions, the phase functions will tend to be smooth and feature less. In Figure 3.9 we have used two different widths of the shape distributions: one with $\mu_{eff} = 5\%$ (solid lines) and one with $\mu_{eff} = 10\%$ (dashed lines). Curiously enough, there is hardly any difference between the two distributions for this specific choice of size parameter ($x = 2$) and μ_{eff}. This could be due to that the two distributions are both centered at the same ε_{eff} and so have some of the same type of particles in their distributions. Also, the phase functions resembles the monodispersion case of Figure 3.1 more than the size-distribution case of Figure 3.5. The reason for this is probably that even though we see a strong shape dependence between the $\varepsilon = 1.1$ case and the $\varepsilon = 2.0$ case, the effective variances of 5% and 10% in each of these are small compared to their difference. For the $\mu_{eff} = 10\%$ case, the maximum ε value considered for $\varepsilon_{eff} = 1.1$ is $\varepsilon = 1.21$, and the minimum ε value considered for $\varepsilon_{eff} = 2.0$ is $\varepsilon = 1.8$. The conclusion must be that even if the shape dependence on the scattering characteristics of these ensembles is strongly present, a shape distribution needs to have μ_{eff} larger than 10% in order to deviate significantly from that of the corresponding monodispersion. In Figure 3.10 the solid lines again corresponds to the $\mu_{eff} = 5\%$ case. In the upper left panel the dotted lines is the linear polarization for spherical particles. The linear polarization curves are very close to those obtained for particles in the Rayleigh region, i.e. at 90° scattering angle an unpolarized incident beam would is almost completely polarized. This effect is again seen to increase with increasing aspect ratio.

Figures 3.11 and 3.12 are as for the two preceding figures, but now for randomly oriented oblate spheroids with $\varepsilon_{eff} = 10$. The difference between the two distributions are now discernible, most likely to the increased size of the particles.

3.3.4 Size-shape distributions

Figures 3.13 through 3.16 contain the results for the size-shape distributions. The phase function is in general less like that of the spherical equivalent size distribution than for any of the preceding cases. The asymmetry parameter decreases monotonously with increasing aspect ratio. These distributions have in general stronger backscatter depolarization values.

3.4 Summary

We have developed a method for accurate computation of the optical properties of spheroidal particles for a wide range of shapes, sizes, and complex refractive indices. The method has been proven to function almost as well for spheroidal particles as the Mie theory for spherical particles. In this chapter we have shown only a few examples of phase functions for ensembles of randomly oriented distributions of spheroidal particles. We have considered monodispersions, size-, shape-, and size-shape distributions. The phase functions of distributions of randomly oriented spheroidal particles are smooth and feature-less and as such closely resemble the phase functions observed in nature for cases in which the particle habits and orientations are not too uniform.

Spheroids with high aspect ratios and moderate equivalent spheres size parameters have interesting unique scattering properties. Their phase functions are similar to those of equivalent size distributions of spheres and spheroids with moderate aspect ratios, but the other elements of the scattering matrix seem to approach those typical of smaller particles closer to the Rayleigh scattering regime. In particular, the linear polarization of these particles approaches a maximum near 1 for scattering angles around 90°, and the backscatter depolarization tends to be small. The important lesson from this is that the value of the backscatter depolarization can not be used as a direct indicator of the degree of particle asphericity. This result is important for applications involving remote sensing of particle size and shape.

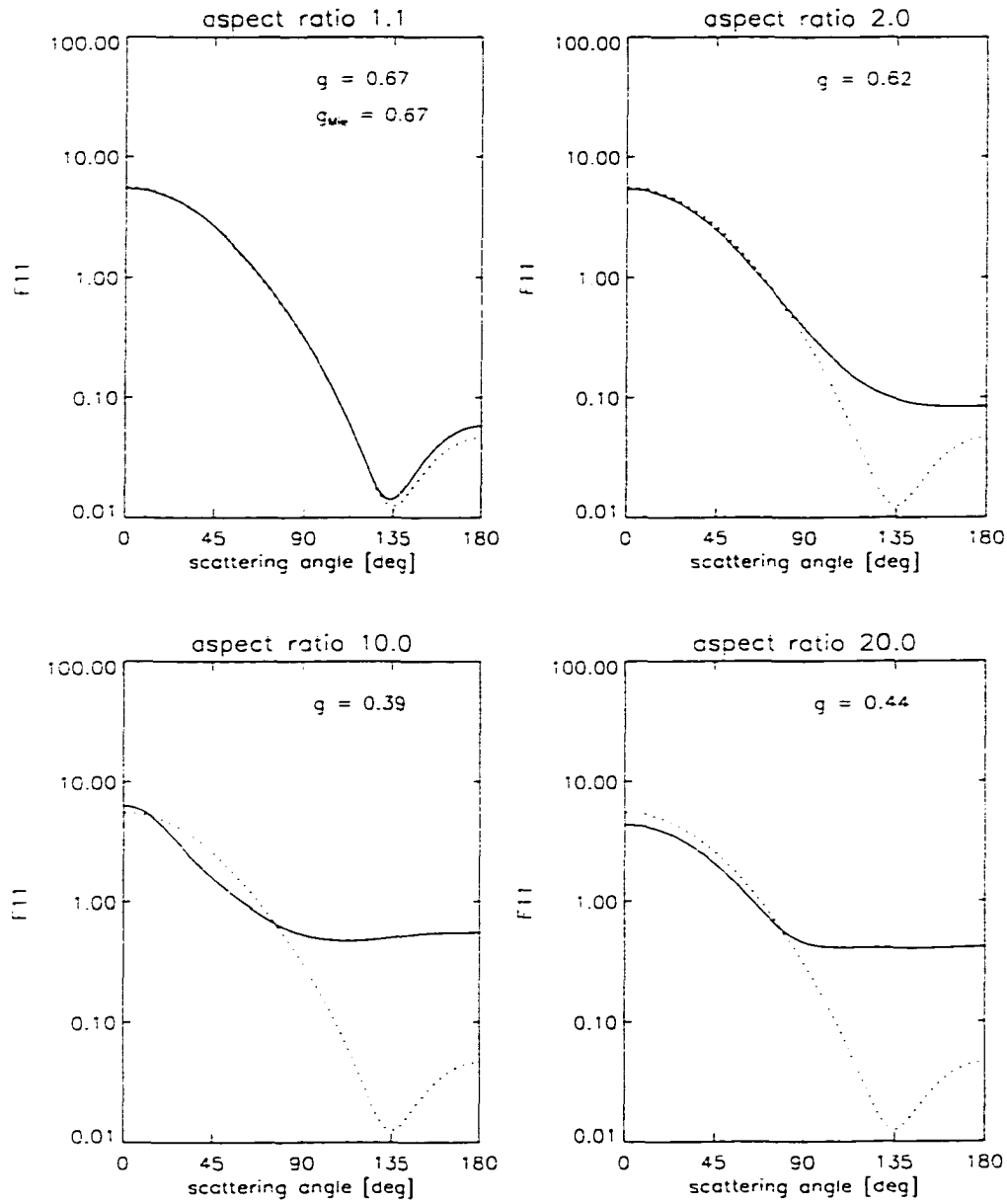

Figure 3.1. Phase function for randomly oriented monodisperse prolate spheroids with equal area sphere size parameter $x = 2$ for various aspect ratios (solid lines). The refractive index is $1.31 + i6.1 \times 10^{-9}$. The dotted line shows corresponding results for the equivalent spheres. The asymmetry parameter of the phase functions are included in each panel.

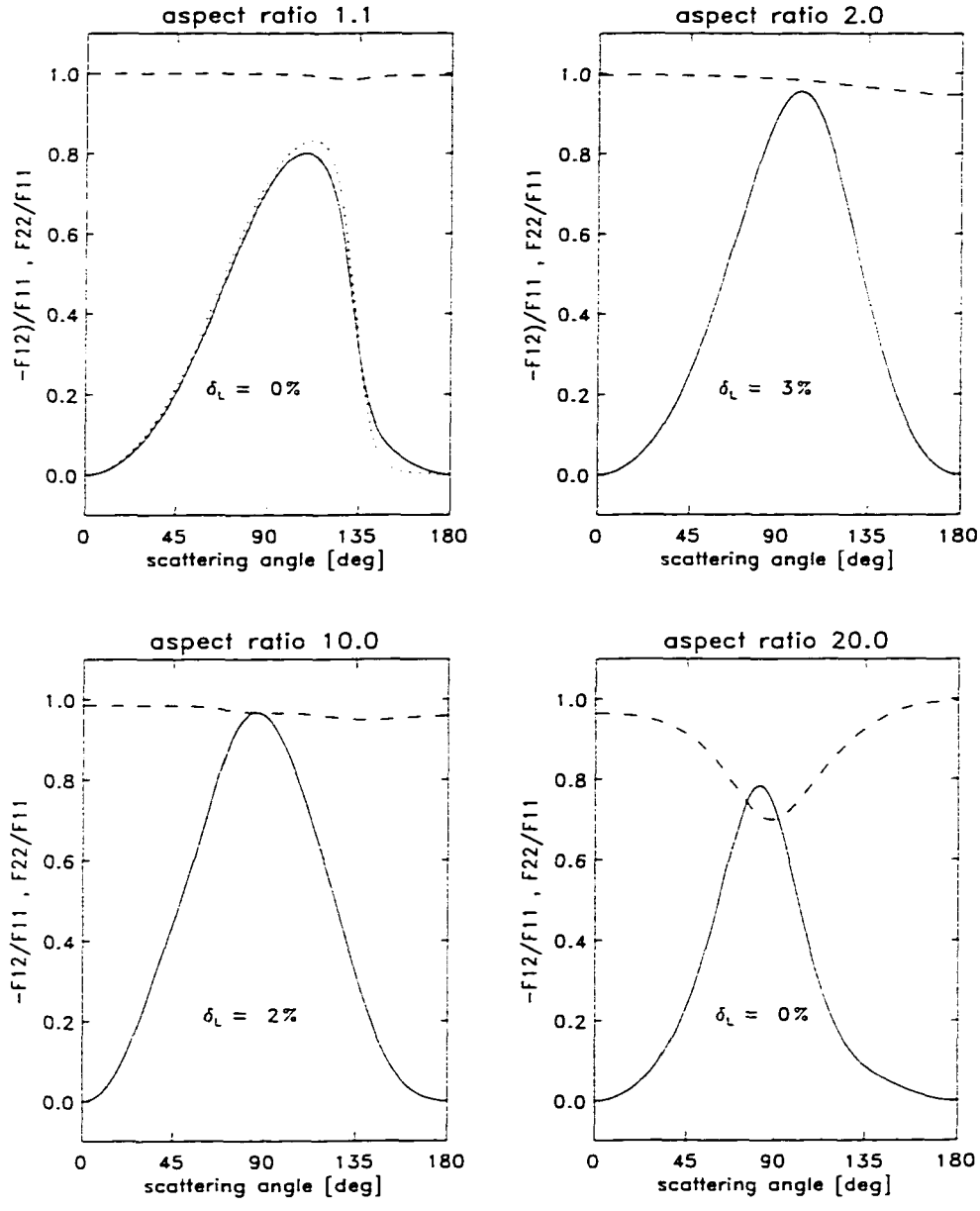

Figure 3.2. Plot of $F_{2,2}/F_{1,1}$ (dashed lines) and the linear polarization $F_{1,2}/F_{1,1}$ (solid lines) for randomly oriented monodisperse prolate spheroids with size parameter $x = 2$ for various aspect ratios. The refractive index is $1.31 + i6.1 \times 10^{-9}$. The value of the linear depolarization, δ_L, at the backscatter angle is indicated in each panel. The dotted line in the upper left panel is the result for the equivalent spheres.

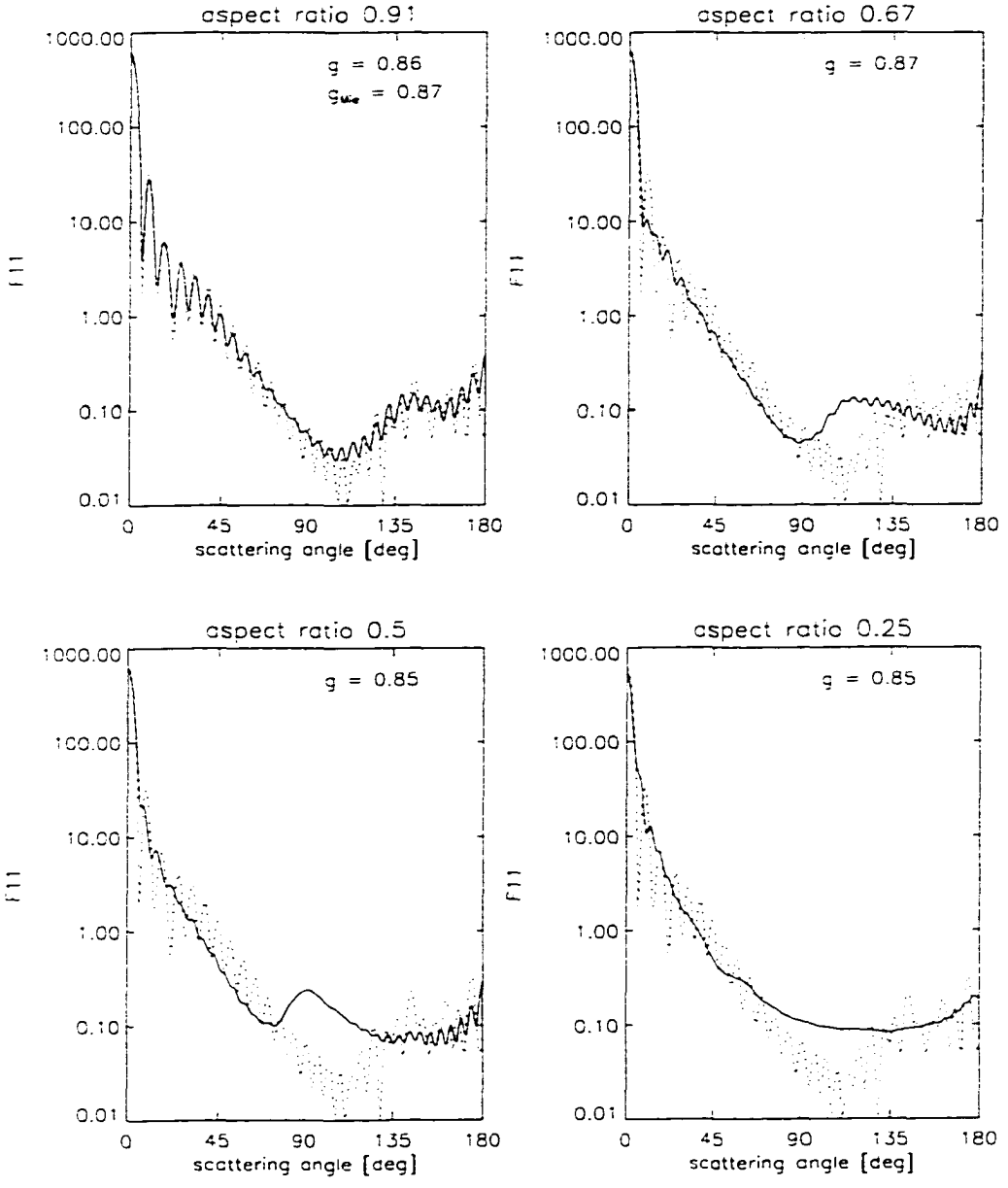

Figure 3.3. Phase function for randomly oriented monodisperse oblate spheroids with size parameter $x = 30$ for various aspect ratios (solid lines). The refractive index is $1.33 + i0.005$. The dotted line shows corresponding Mie results for the equivalent spheres. The value of the asymmetry parameter is included in each panel.

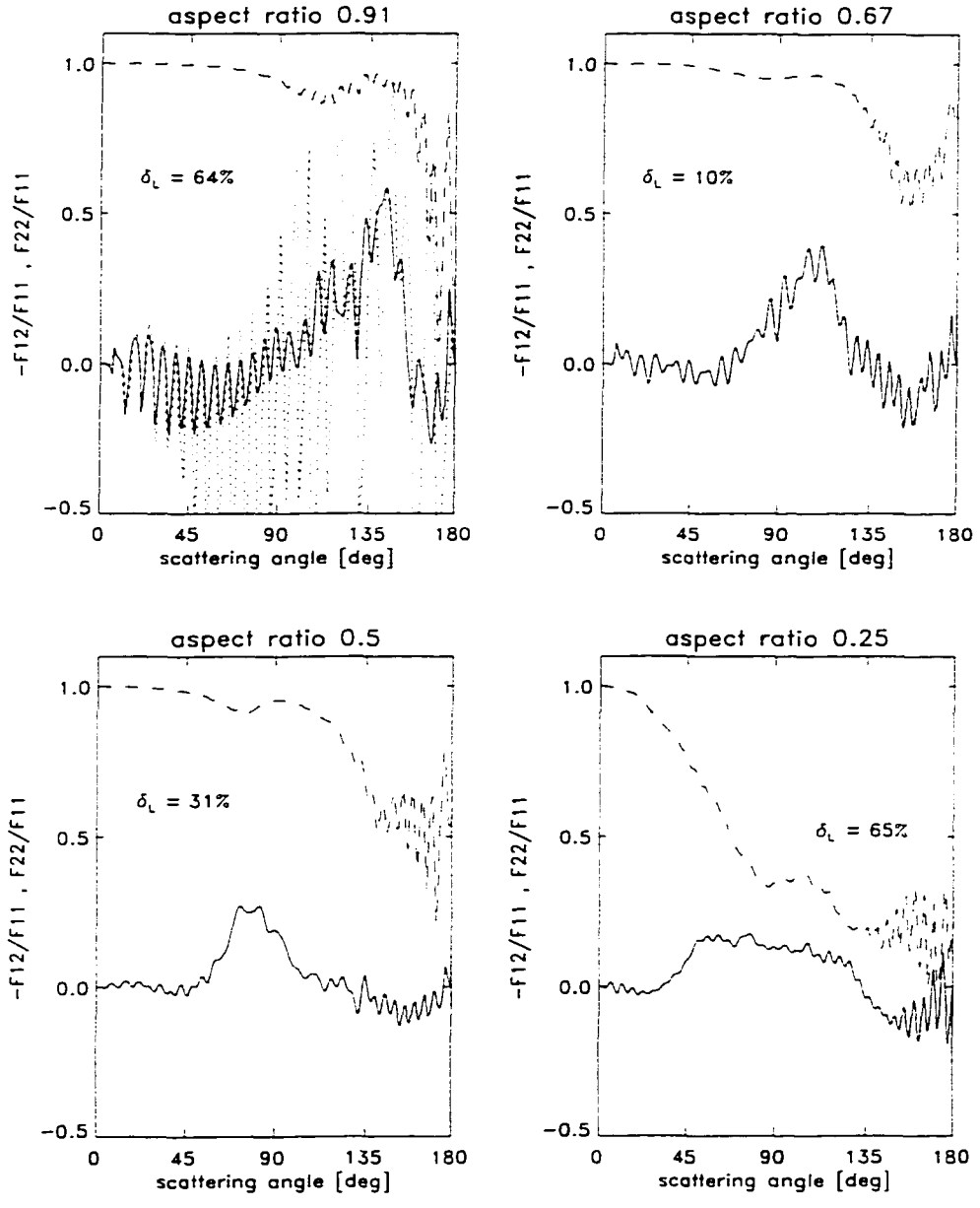

Figure 3.4. Plot of $F_{2,2}/F_{1,1}$ (dashed lines) and the linear polarization $F_{1,2}/F_{1,1}$ (solid lines) for randomly oriented monodisperse oblate spheroids with size parameter $x = 30$ for various aspect ratios. The refractive index is $1.33 + i0.005$. The value of the linear backscatter depolarization, δ_L, is indicated in each panel.

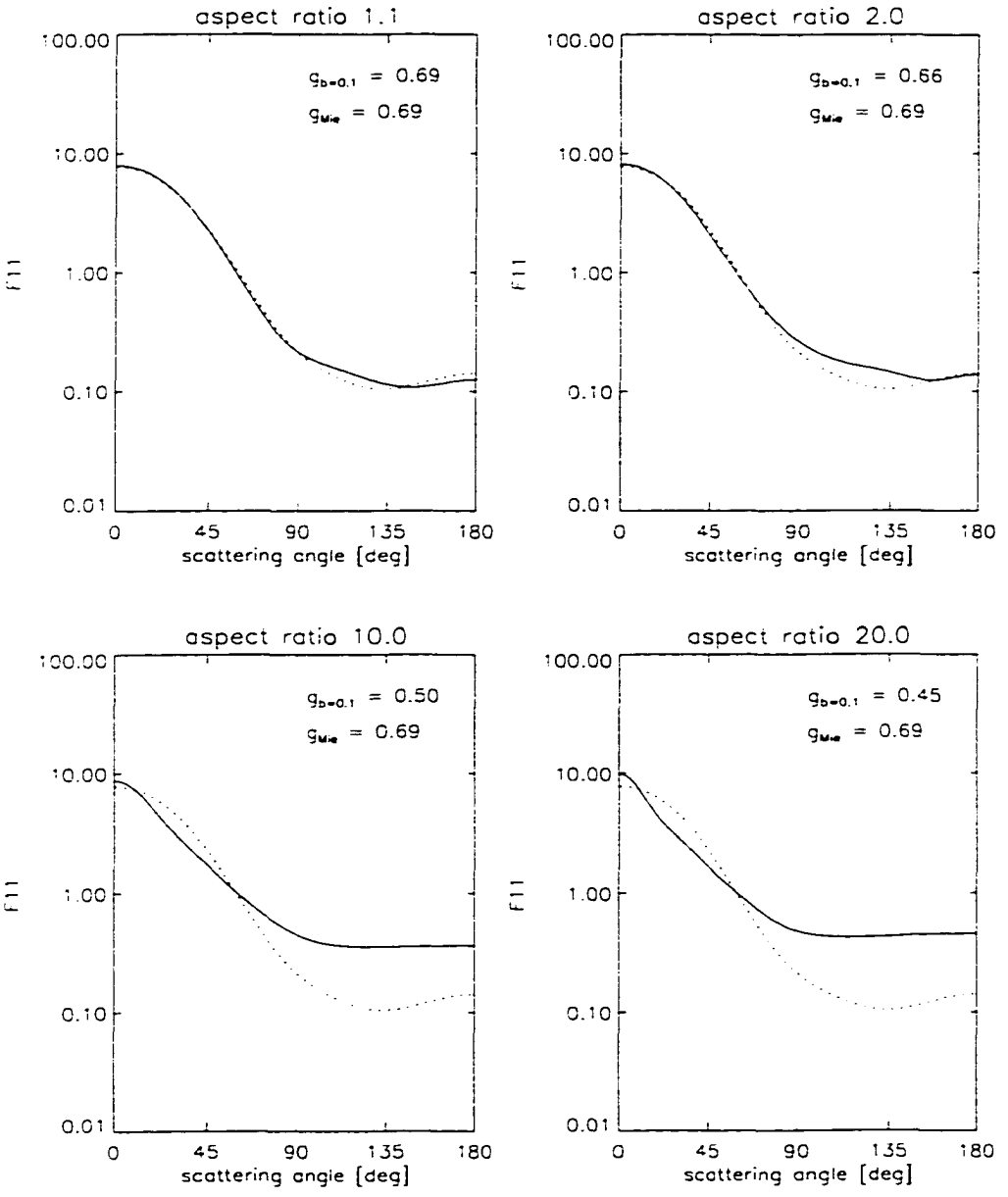

Figure 3.5. Phase function for a size distribution of randomly oriented prolate spheroids with effective size parameter $x = 2$ and variance $\nu_{eff} = 0.1$ for various aspect ratios (solid lines). The refractive index is $1.31 + i6.1 \times 10^{-9}$. The dotted line corresponds to the equivalent spheres.

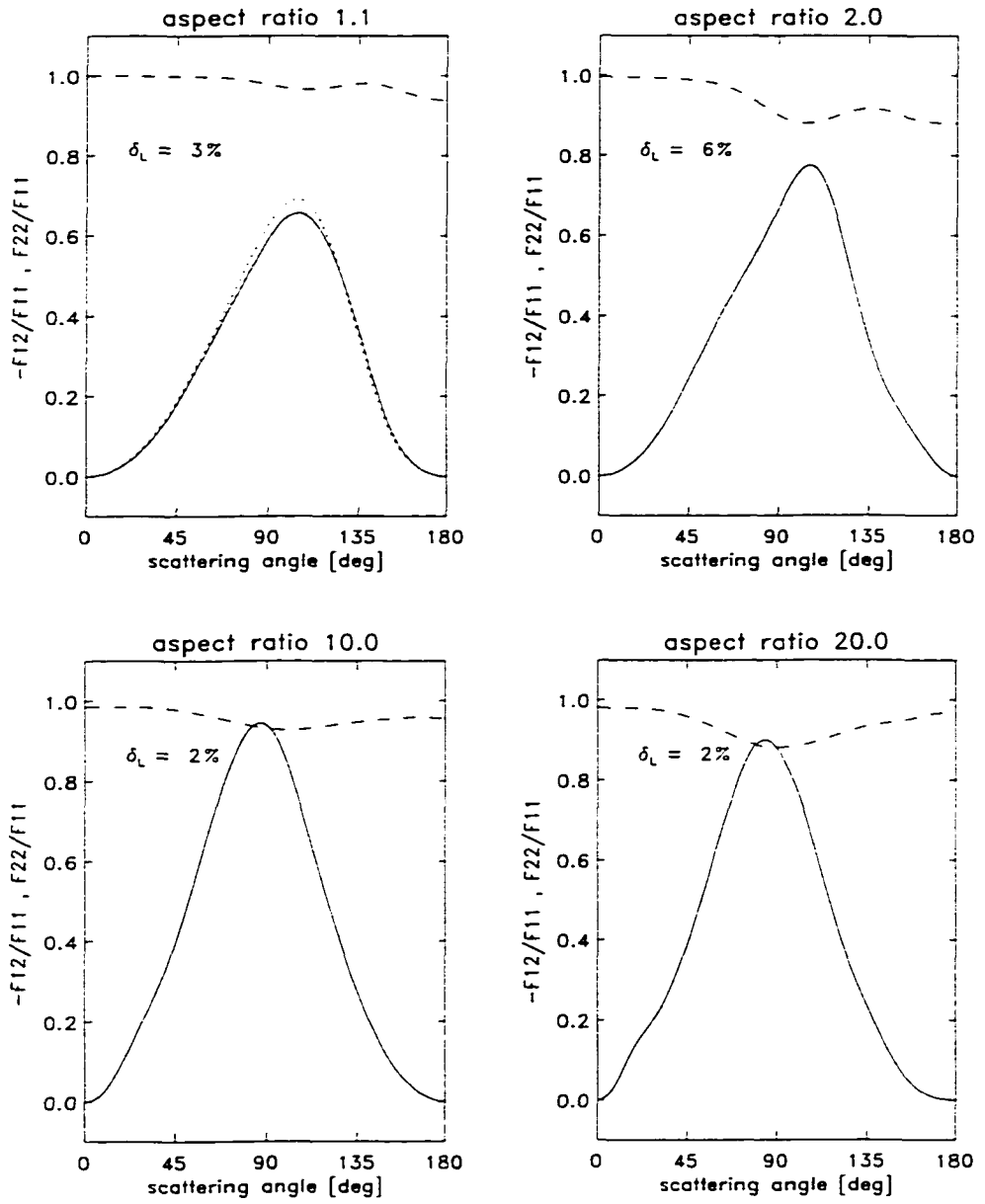

Figure 3.6. Figure showing $F_{1,2}/F_{1,1}$ (solid lines) and $F_{2,2}/F_{1,1}$ (dashed lines) for a size distribution randomly oriented prolate spheroids with size parameter $x = 2$ for various aspect ratios. The refractive index is $1.31+i6.1\times10^{-9}$. The value of the linear backscatter depolarization, δ_L. is indicated in each panel. The dotted line in the upper left panel is for the equivalent spheres.

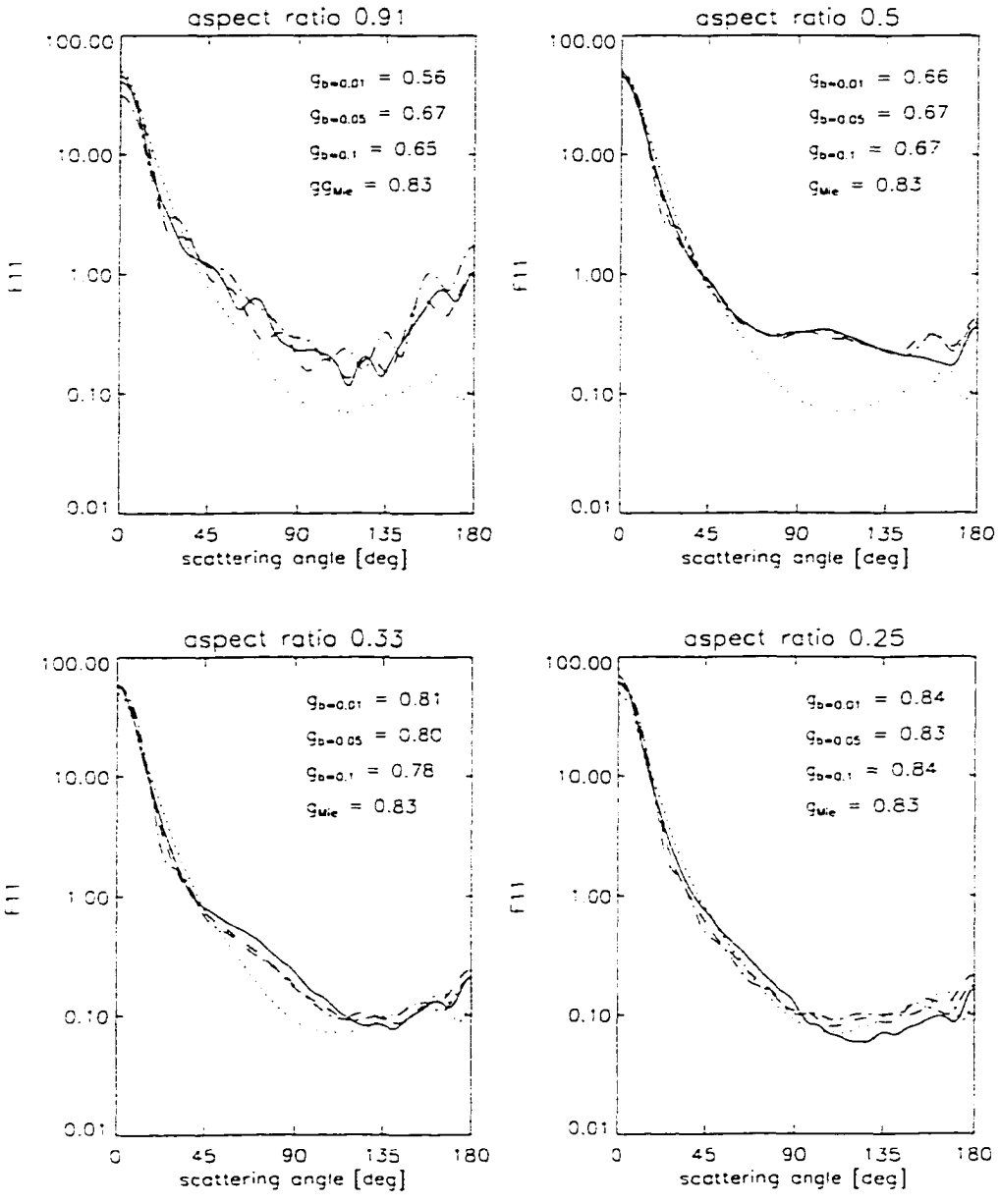

Figure 3.7. Figure showing the phase functions for size distributions of randomly oriented oblate spheroids with effective size parameter $x = 8$ and effective size variance $\nu_{eff} = 0.1$ (solid lines), $\nu_{eff} = 0.05$ (dashed lines), $\nu_{eff} = 0.01$ (dash-dotted lines) for various aspect ratios. The refractive index is $1.31 + i6.1 \times 10^{-9}$. The dotted line corresponds to the equivalent spheres.

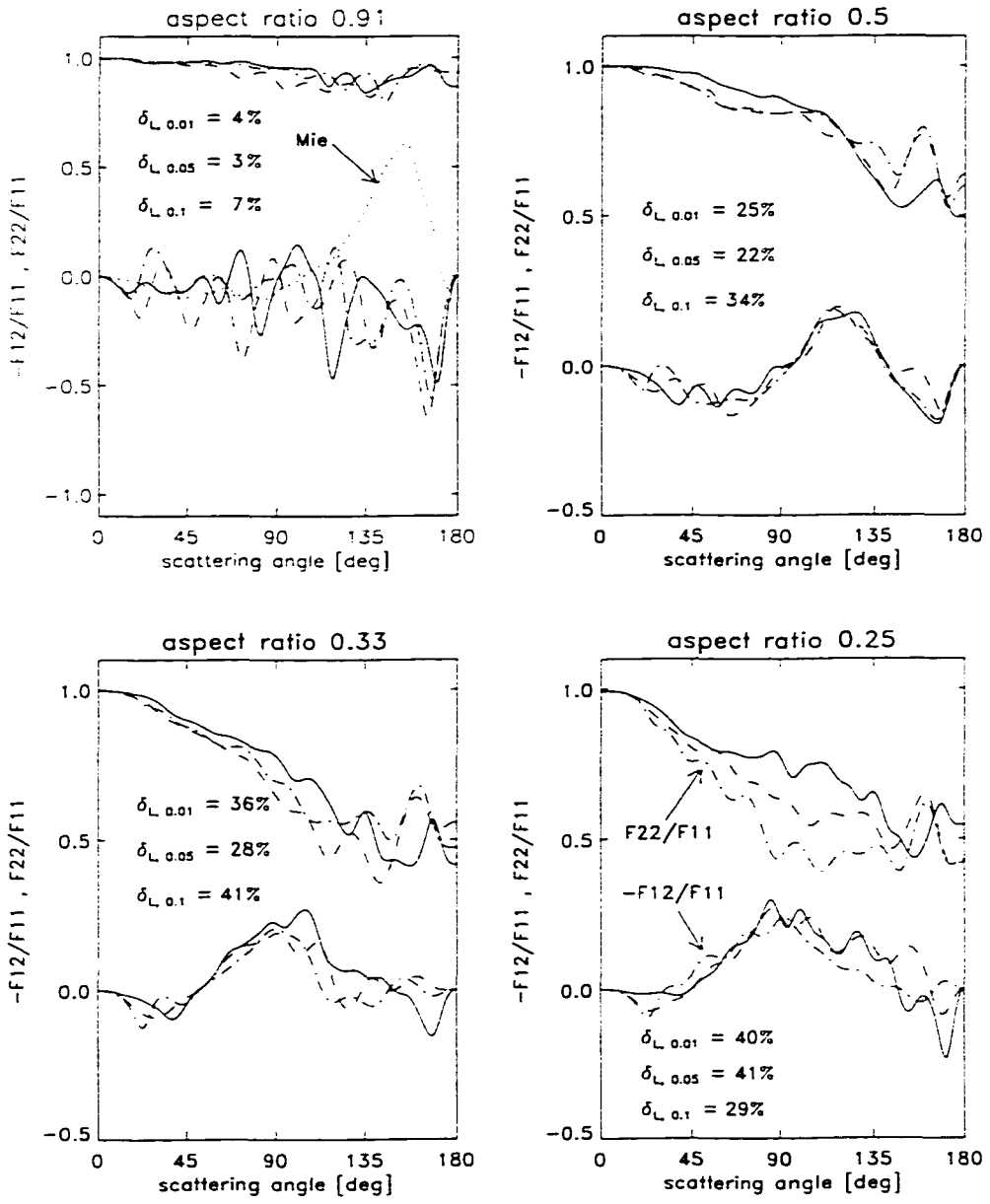

Figure 3.8. Figure showing $F_{1,2}/F_{1,1}$ and $F_{2,2}/F_{1,1}$ for size distributions of randomly oriented oblate spheroids with size parameter $x = 8$ for various aspect ratios. The effective size variance is $\nu_{eff} = 0.1$ (solid lines), $\nu_{eff} = 0.05$ (dashed lines), $\nu_{eff} = 0.01$ (dash-dotted lines). The refractive index is $1.31 + i6.1 \times 10^{-9}$. The value of the linear backscatter depolarization, δ_L, is indicated in each panel. The dotted line in the upper left panel is for the equivalent spheres.

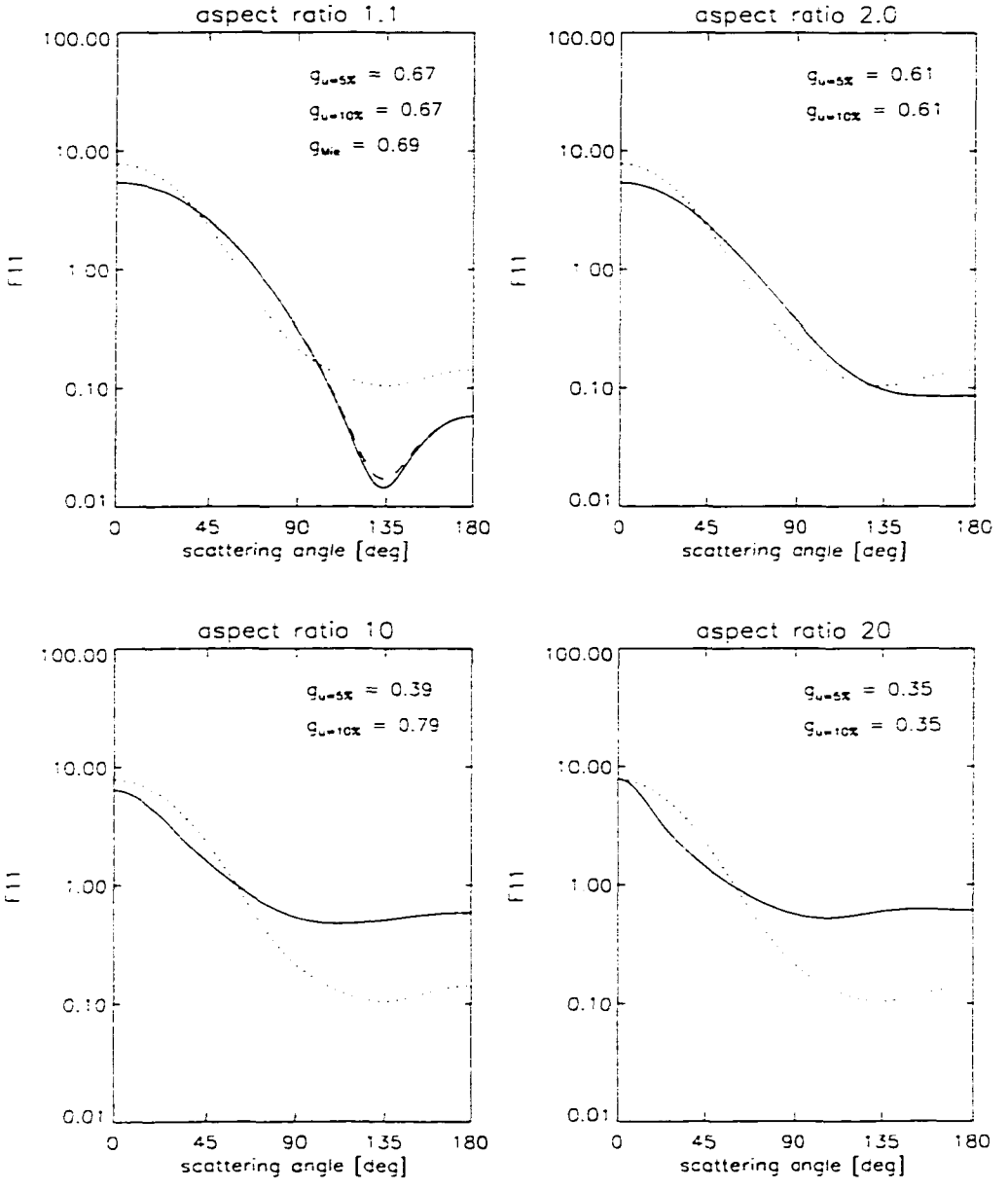

Figure 3.9. Figure showing the phase function for shape distributions of randomly oriented prolate spheroids with effective size parameter $x = 2$ and various aspect ratios. The refractive index is $1.31 + i6.1 \times 10^{-9}$. Two lines, one for shape variance $\mu_{eff} = 0.1$ (solid lines), and one for shape variance $\mu_{eff} = 0.2$ (dashed lines), are hardly distinguishable. The dotted line corresponds to the equivalent spheres.

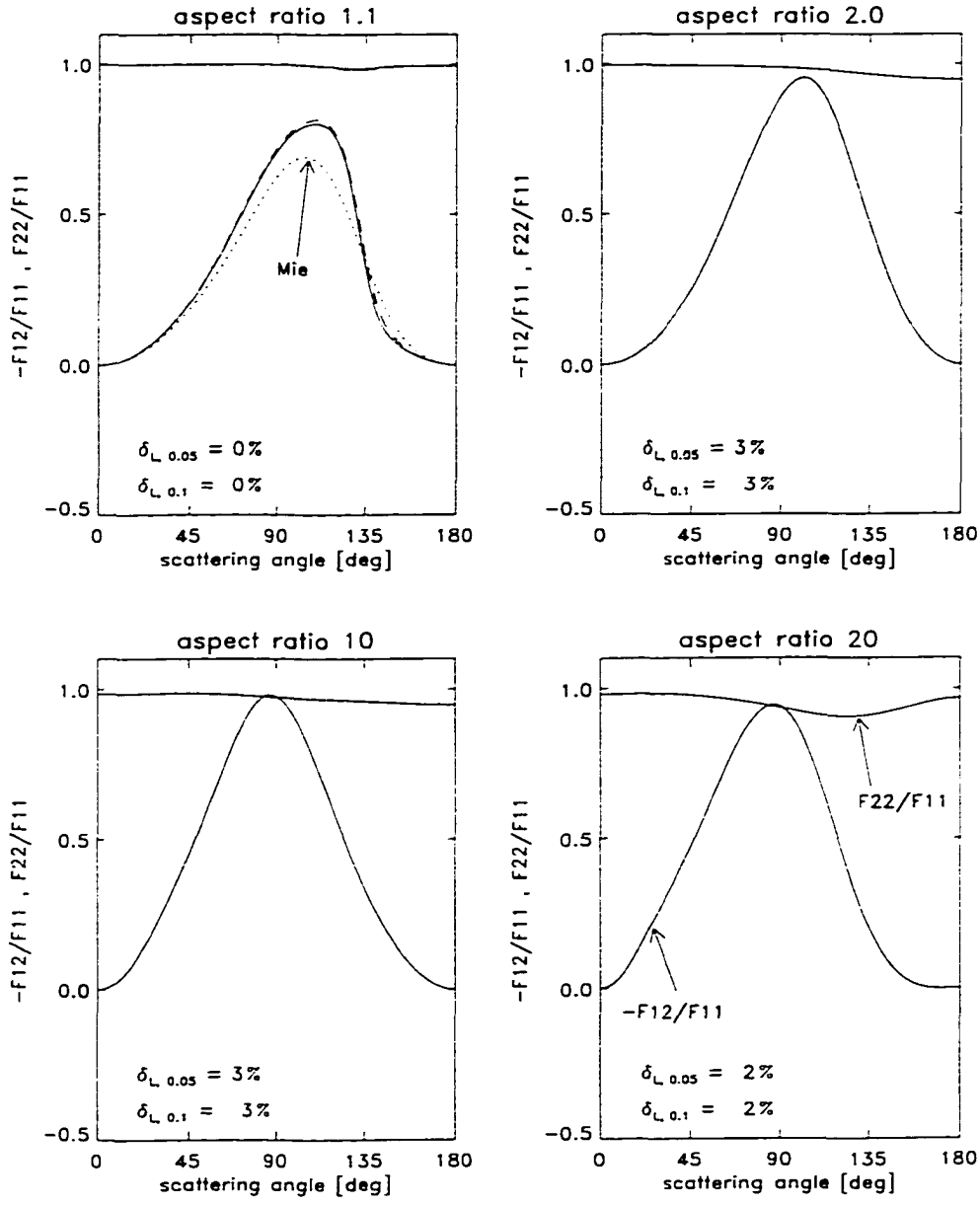

Figure 3.10. Figure showing $F_{1,2}/F_{1,1}$ and $F_{2,2}/F_{1,1}$ for shape distributions of randomly oriented prolate spheroids with size parameter $x = 2$ for various aspect ratios. Two lines, one for shape variance $\mu_{eff} = 0.1$ (solid lines), and one for shape variance $\mu_{eff} = 0.2$ (dashed lines), are hardly distinguishable. The refractive index is $1.31 + i6.1 \times 10^{-9}$. The value of the linear backscatter depolarization, δ_L, is indicated in each panel. The dotted line in the upper left panel is for the equivalent spheres.

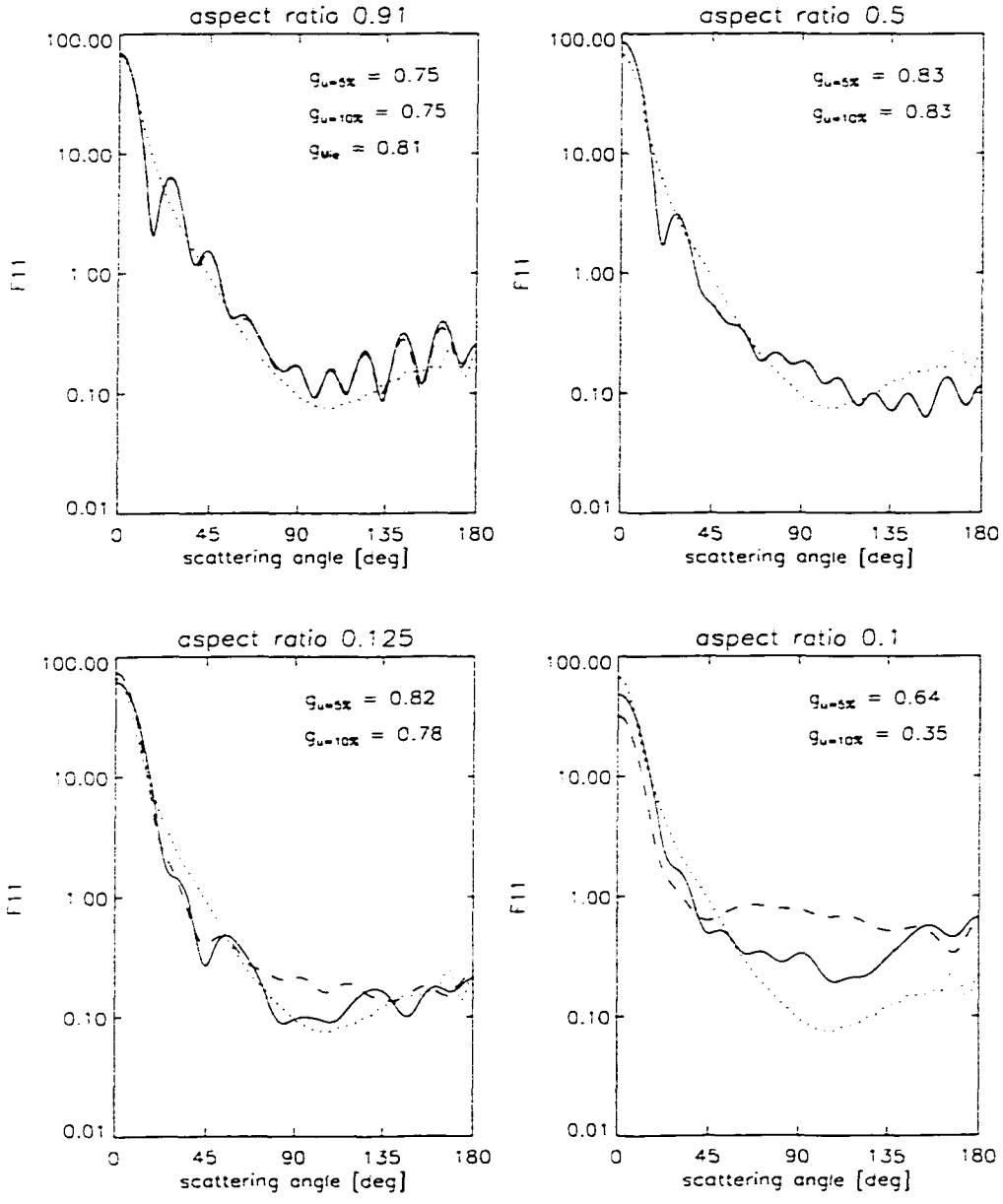

Figure 3.11. Figure showing the phase function for shape distributions of randomly oriented oblate spheroids with effective size parameter $x = 10$ and various aspect ratios. The refractive index is $1.31 + i6.1 \times 10^{-9}$. Two lines, one for shape variance $\mu_{eff} = 0.5$ (solid lines), and one for shape variance $\mu_{eff} = 1.0$ (dashed lines), are hardly distinguishable in the upper panels. The dotted line corresponds to the equivalent spheres.

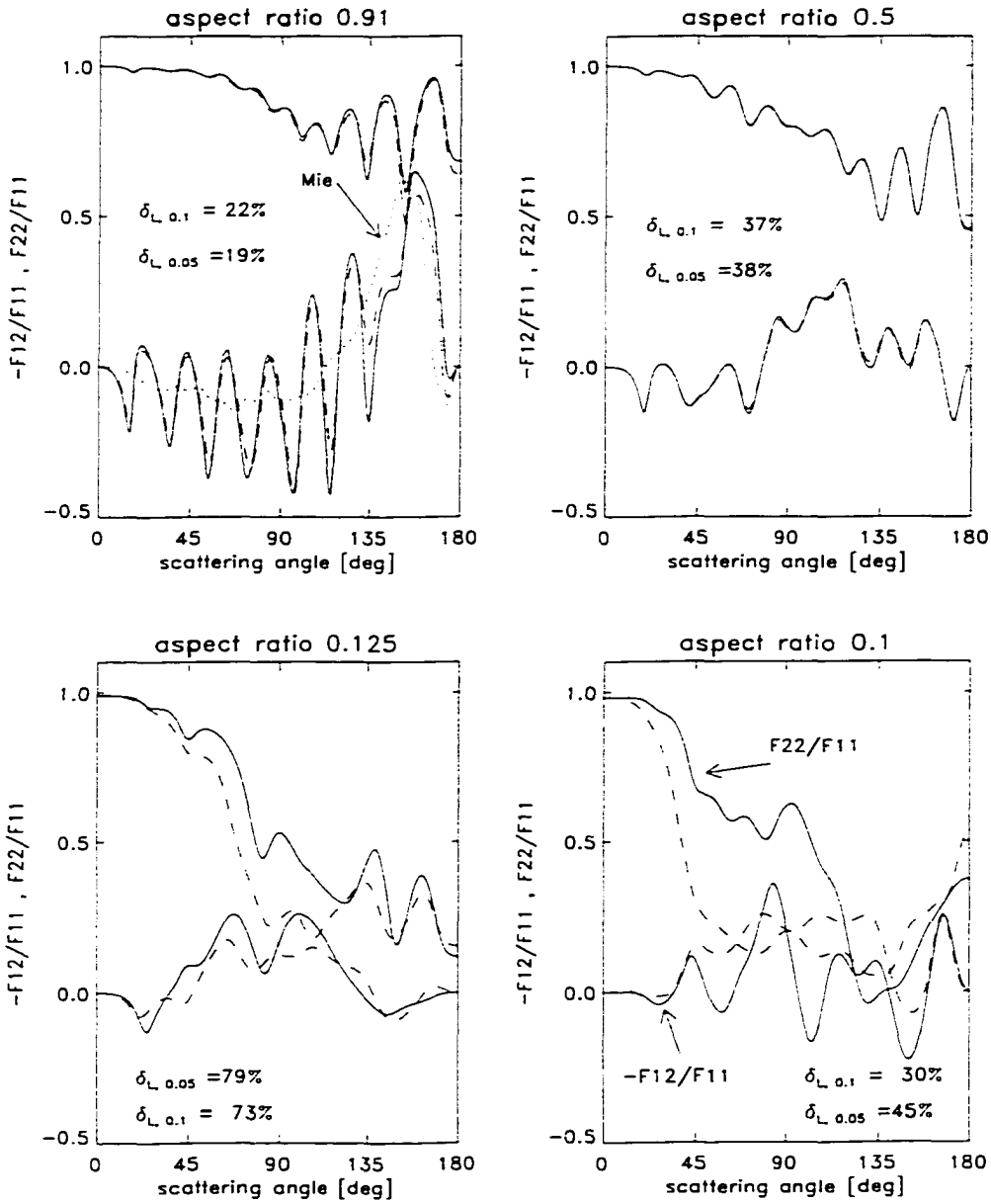

Figure 3.12. Figure showing $F_{1,2}/F_{1,1}$ and $F_{2,2}/F_{1,1}$ for shape distributions of randomly oriented oblate spheroids with size parameter $x = 10$ for various aspect ratios. There are two lines, one for shape variance $\mu_{eff} = 0.5$ (solid lines), and one for shape variance $\mu_{eff} = 1.0$ (dashed lines). The refractive index is $1.31 + i6.1 \times 10^{-9}$. The value of the linear backscatter depolarization, δ_L, is indicated in each panel. The dotted line in the upper left panel is for the equivalent spheres.

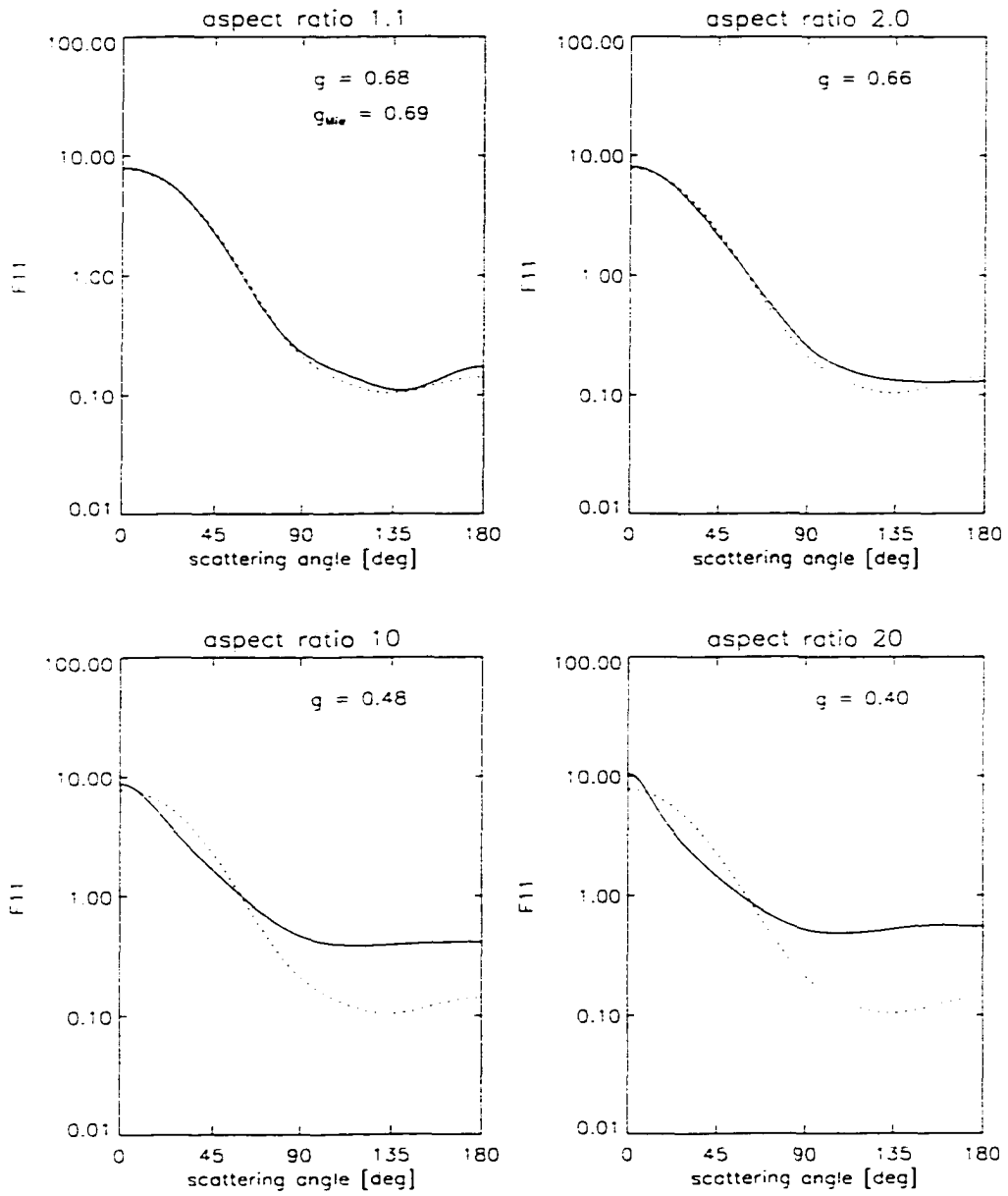

Figure 3.13. Figure showing the phase function for a size-shape distribution of randomly oriented prolate spheroids with effective size parameter $x = 2$ for various aspect ratios. The size variance is $\nu_{eff} = 0.1$, and the shape variance is $\mu_{eff} = 0.1$. The refractive index is $1.31 + i6.1 \times 10^{-9}$. The dotted line corresponds to the equivalent spheres.

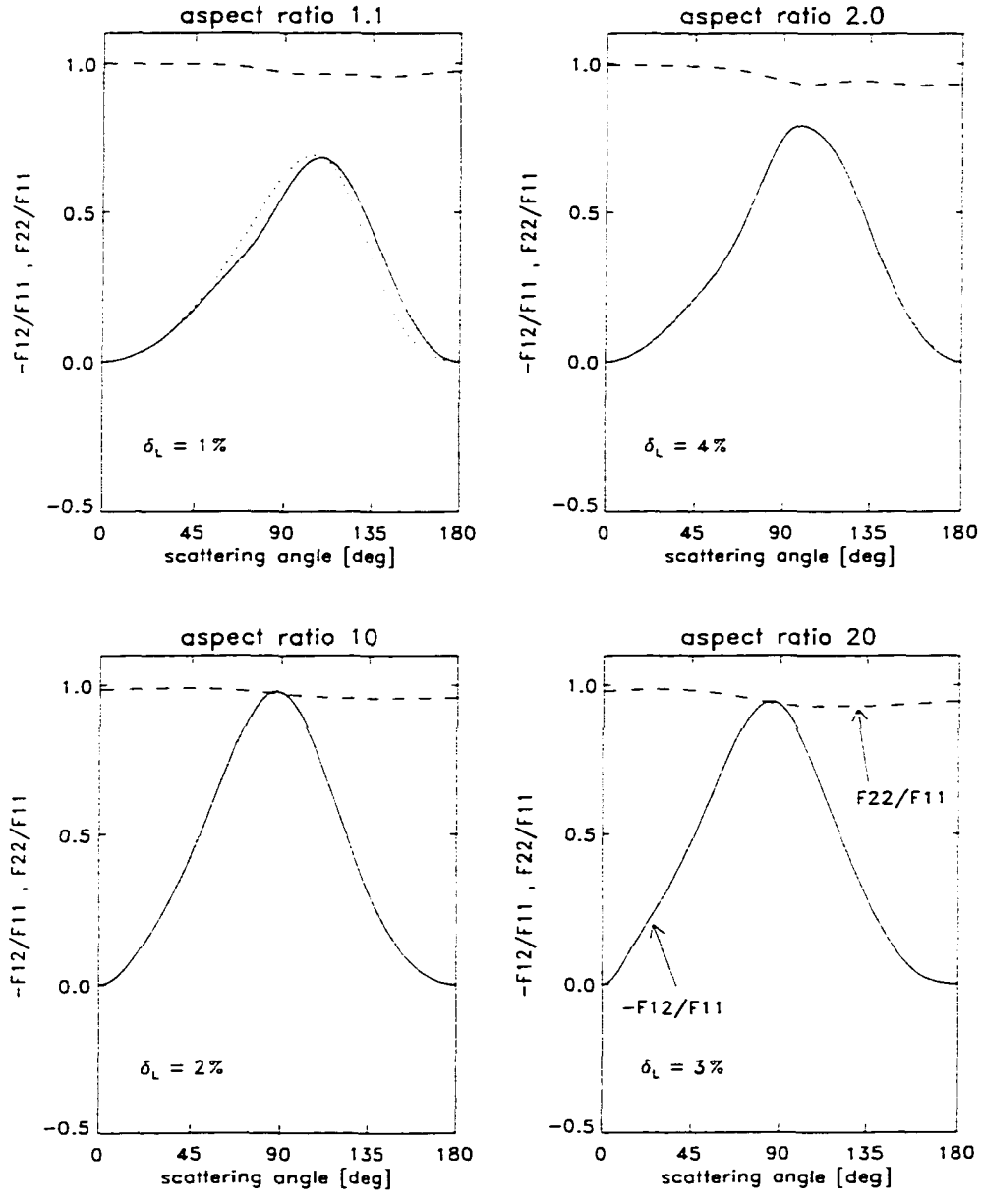

Figure 3.14. Figure showing $F_{1,2}/F_{1,1}$ and $F_{2,2}/F_{1,1}$ for size-shape distributions of randomly oriented prolate spheroids with size parameter $x = 2$ for various aspect ratios. The size variance is $\nu_{eff} = 0.1$, and the shape variance is $\mu_{eff} = 0.1$. The value of the linear backscatter depolarization, δ_L, is indicated in each panel. The dotted line in the upper left panel is for the equivalent spheres.

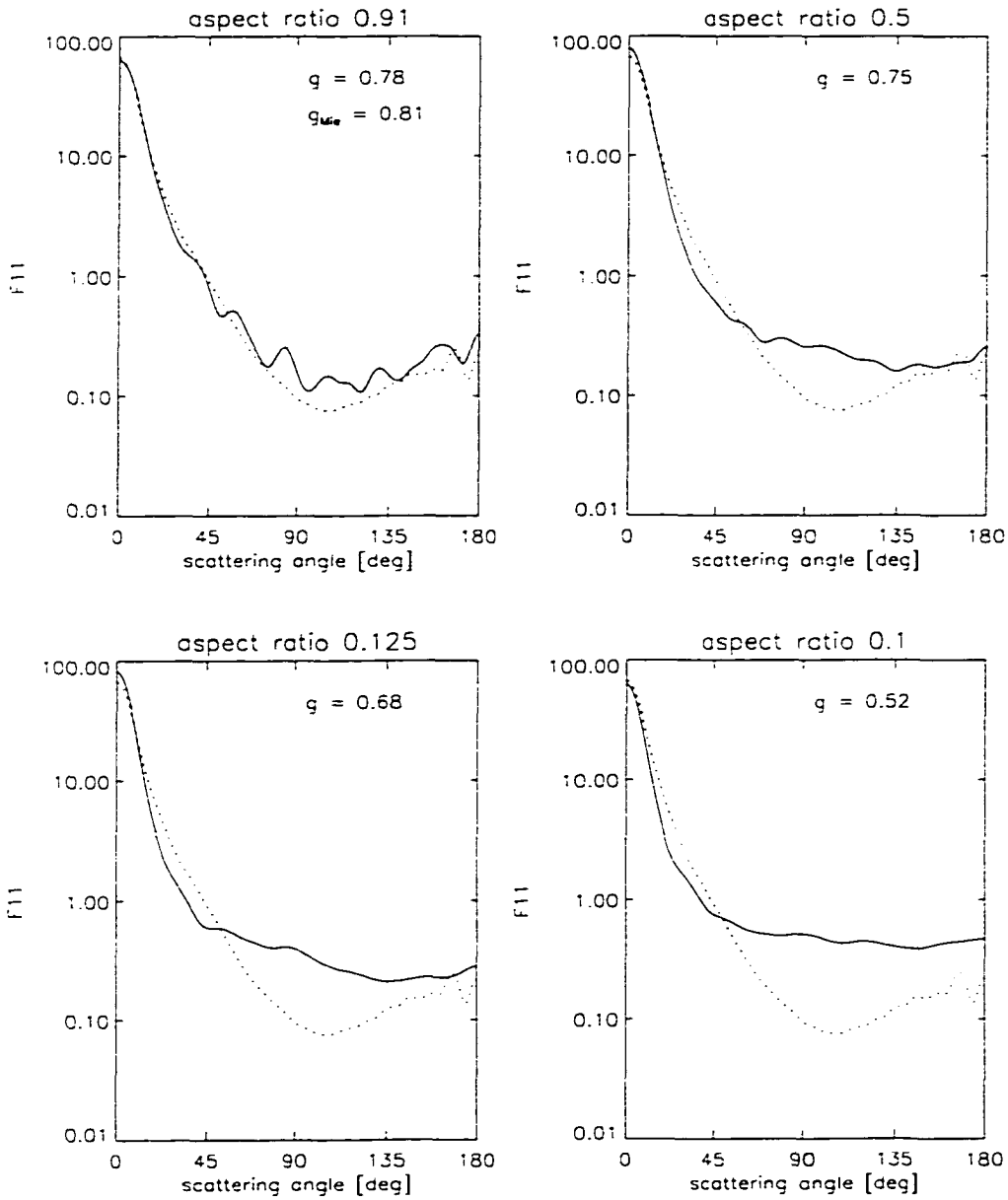

Figure 3.15. Phase function for a size-shape distribution of randomly oriented oblate spheroids with effective size parameter $x = 10$ for various aspect ratios. The size variance is $\nu_{eff} = 0.1$, and the shape variance is $\mu_{eff} = 0.5$. The refractive index is $1.31 + i6.1 \times 10^{-9}$. The dotted line corresponds to the equivalent spheres.

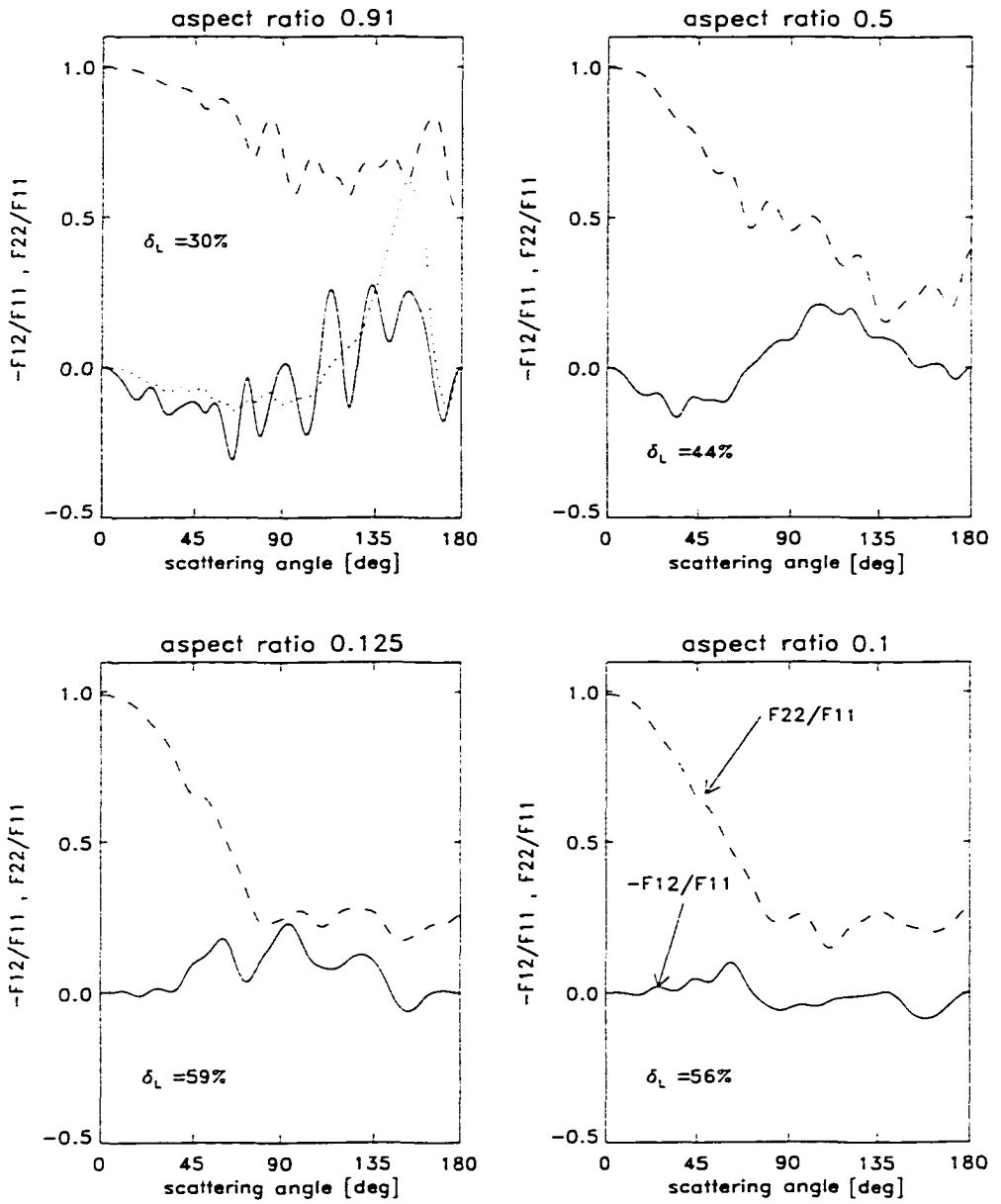

Figure 3.16. Figure showing $F_{1,2}/F_{1,1}$ and $F_{2,2}/F_{1,1}$ for size-shape distributions of randomly oriented oblate spheroids with size parameter $x = 10$ for various aspect ratios. The size variance is $\nu_{eff} = 0.1$, and the shape variance is $\mu_{eff} = 0.5$. The value of the linear backscatter depolarization, δ_L, is indicated in each panel. The dotted line in the upper left panel is for the equivalent spheres.

Chapter 4

Modeling lidar backscatter

Theoretical studies on lidar observations of polar stratospheric clouds (PSCs), and on lidar observations of clouds consisting of nonspherical particles in general, are sparse. This is due to the complex nature of the scattering problem and the wide range of size, shape, and compositions of the (nonspherical) particles found in nature, as well as the lack of a general, fast, accurate, and easy-to-use model for doing the scattering computations.

It is a well known fact that nonspherical particles will depolarize a linearly polarized lidar beam, but too few theoretical studies have been done to establish whether or not further information about the scattering particles can be deduced from polarization lidar observations. Even when some a priori knowledge of the scattering particles exists, it remains to be shown if observations of linearly depolarized lidar returns from one wavelength alone can be utilized for particle sizing or for obtaining other information about the scattering medium.

The particles in an actual ice-cloud, and the aerosols in the atmosphere in general, are not spheroids, but modeling ensembles of such nonspherical particles with ensembles of spheroids have been shown to yield very useful results [11, 18, 58]. Compared to a spherical particle, the spheroidal particle can be characterized by only one additional parameter, namely the shape (or eccentricity). As discussed in previous chapters, several

models for calculating the single scattering properties of spheroids exist [3. 15].

The present study is aimed at improving the theoretical basis for polarization lidar studies by expanding the range of applicability of the spheroidal particle model and combining it with vector radiative transfer computations. More specifically, the new model for calculating the scattering properties of ensembles of randomly oriented spheroids will be used together with a vector radiative transfer code to interpret lidar data. The intention is to validate the new method by comparing results with benchmark studies, and use it to provide new insights to aid the interpretation of lidar data.

One advantage of computing **T**-matrix is that it greatly simplifies the averaging over particle orientations and thus facilitates the computation of the scattering characteristics for various types of particle distributions. In nature, an actual PSC is likely to consist of particles with varying sizes and shapes. Results for the backscattering by polydispersions are presented here. It is well known that the backscattering of a monodispersion of spheres will oscillate greatly with particle size parameter (ratio between particle size and wavelength), at least when the size of the spheres are comparable to the wavelength, and that this effect is smeared out if a polydispersion is introduced. Similarly, a monodispersion of nonspherical particles will have distinct backscattering features (but less pronounced than for spheres). However, here we find that even narrow distributions in size and/or shape will tend to smear out these features. It seems, then, that we need to look for features in the backscattering from polydispersions if we are to make reliable inferences about the particles in nature studied by lidar, or at least we need to know the effect of polydispersions on the backscattering.

By modeling the optical properties of ensembles of nonspherical particles we can compute the lidar return from various types of clouds. We can determine if one wavelength of a polarization lidar is enough to retrieve information about the size or shape of the particles in actual clouds. The theoretical computations can also be used to develop retrieval algorithms for use with polarization lidars. Here we will study the case of PSCs as this is a problem for which both theoretical and actual data are readily available.

4.1 Introduction

Having obtained the Fourier expansion coefficients of the Stokes scattering matrix for size-shape distributions of spheroidal particles, we can use them in a vector radiative transfer model to compute the impact of nonspherical particle shape on the radiation field, or, if we are studying lidar problems, we can model the backscatter returns from a variety of size-shape distributions. Schulz et al. [67, 68, 69] studied the effect of nonspherical particles on radiative transfer using this approach. Here we use the same methods to model the polarization lidar backscatter signal from PSCs.

As discussed in the previous chapters, we have developed a new method for calculating the coefficients in the eigenfunction expansions required to solve the problem of scattering by spheroidal particles using the Separation of Variables Method (SVM) [1]. Also, a new method for finding the **T**-matrix based on the single scattering calculations obtained with the SVM is available [16].

To validate and check the results obtained with our scattering code we have compared them with results obtained by other investigators using different methods. These comparisons indicate that our results are in close agreement with those obtained by Mishchenko and co-workers using the Extended Boundary Condition Method (EBCM) [70, 18, 71]. Our method allows us to study particles with relatively large sizes and aspect ratios. Two studies by Toon et al. [2, 20] discussed lidar returns by PSCs. In these works Toon et al. established a classification scheme for PSC particles in terms of the computed lidar returns based on assumptions about their shape, size, and composition.

PSC particles are commonly classified in two major types, type 1 and 2. PSCs of type 2 consist of particles larger than 10 μm. They are identified as water ice clouds and are seldom observed in the polar stratosphere except when they originate from mountain induced gravity waves [72]. PSCs of type 1 consist of typically smaller particles of varying phase and composition. The exact composition of these particles is still a matter of discussion. For type 1 PSCs one distinguishes further between types 1a, 1b, and recently 1c [73]. Type 1a is thought to be nonspherical (solid phase) particles about 1 μm or

larger, that consist of either Nitric Acid Trihydrate (NAT) or Nitric Acid Dihydrate (NAD). Type 1b particles are smaller, spherical particles with a typical radius of about 0.5 μm. These are thought to consist of a ternary solution of sulfuric and nitric acid ($HNO_3/H_2SO_4/H_2O$) [2]. Other types of PSCs have been suggested. Of these the solid phase HNO_3/H_2O type 1c particles [73] are interesting in view of the current investigation as we will show how they can be detected with a dual wavelength lidar system.

Due to their differing sizes and shapes, the various PSC particle types will scatter light differently and can therefore be distinguished with a polarization lidar system. Light scattering models for nonspherical particles provide a tool for determining the predominant size and shape of the particles present in a PSC. Toon et al. [2, 20] computed the scattering properties of PSC type particles. Using a scattering code developed by Barber and Yeh [56], and more recently the code developed by Mishchenko et al. [11], they related the scattering signature of the various types of PSCs to particles of a certain general shape and size range. The computations were based on the assumption that the nonspherical PSC particles have a cylindrical shape that can be approximated with ensembles of randomly oriented prolate and oblate spheroids. To support this assumption they cited observations and laboratory experiments [74, 75] which suggest that the typical nonspherical PSC particle is a prolate cylinder with a rather modest aspect ratio. In these calculations the spheroids were specified in terms of their aspect ratio and their equal volume sphere radii. They also determined the real part of the refractive index of NAT to be about 1.5 with a very small absorption for the two wavelengths (0.603 μm and 1.064 μm) of the Browell [76] lidar system. Also Carslaw et al. [72] inferred from similar scattering calculations that PSC particles should have aspect ratios between 0.85 (oblate) and 1.2 (prolate).

4.2 Lidar backscatter theory

The intensity of the lidar backscatter return is determined by the backscatter efficiency of the scattering medium. If the scattering matrix $\mathbf{F}(\theta, \phi)$ of a particle at a given wavelength

is known, then the Stokes vector $\mathbf{I}_{sca}$ of the light scattered by the particle in direction (θ, ϕ) can be found by

$$\mathbf{I}_{sca} = \mathbf{F}(\theta, \phi)\, \mathbf{I}_{inc}\,. \tag{4.1}$$

and the intensity anywhere in the far field by

$$I_{sca} = \frac{1}{k^2 R^2}\, \mathbf{F}(\theta, \phi)\, I_{inc}\,. \tag{4.2}$$

Here $\mathbf{I}_{inc} = (I_i, Q_i, U_i, V_i)$ is the Stokes vector of the incoming light, $k = 2\pi/\lambda$ is the corresponding wavenumber, and R is the distance from the particle to the observation point. $\mathbf{F}$ is thus a dimensionless function of direction. Dividing $\mathbf{F}$ by $k^2 C_{sca}$ another dimensionless function called the phase phase matrix, $\mathbf{Z}$, is obtained. Integrating the $(1,1)$ element of the phase matrix, called the phase function, over all directions yields 1. and it can therefore also be viewed as a probability function describing the probability that light will be scattered in a certain direction. The scattering cross section, C_{sca}, of the particle is defined such that the total energy leaving (scattered by) the particle in all directions is equal to the energy of the incident wave falling upon the area C_{sca}, or

$$\begin{aligned} C_{sca} &= \frac{1}{I_{inc}} \int_{4\pi} d\mathbf{n}_{sca} \mathbf{I}_{sca}(\mathbf{n}_{sca}) \\ &= \frac{1}{k^2} \int_{4\pi} d\omega\, F(\theta, \phi)\,. \end{aligned} \tag{4.3}$$

where $\mathbf{n}^{sca}$ is the unit vector in the direction of the far-field diverging scattered spherical wave, and $d\omega = \sin\theta\, d\theta d\phi$. The scattering matrix, $\mathbf{F}(\Theta)$, for a macroscopically isotropic and symmetric medium (e.g. an ensemble of particles with a plane of symmetry) is invariant with respect to the choice of the scattering plane, that is, it depends only on the angle Θ between the incident and scattered beams. It is defined as [3, 15]

$$\mathbf{F}(\Theta) = \frac{4\pi k^2}{C_{sca}} < \mathbf{Z}(\boldsymbol{\Theta}) >\,. \tag{4.4}$$

where $< \mathbf{Z} >$ is the orientationally averaged phase matrix. Equation 4.3 can in this case also be written as

$$C_{sca} = 2\pi \int_0^{\pi} d\Theta \sin\Theta \; < Z_{1,1}(\Theta) > . \tag{4.5}$$

and Eq. 4.1 can be written as

$$I_{sca}(\Theta) = \frac{4\pi}{C_{sca}\, k^4\, R^2} \; < Z_{1,1}(\Theta) > \; I_{inc} . \tag{4.6}$$

The energy leaving the particle in any direction Θ relative to the incoming beam through a hypothetical circumscribing sphere is thus

$$I_{sca}(\Theta) = \frac{1}{k^2 R^2} F_{1,1}(\Theta) I_{inc} . \tag{4.7}$$

The direction dependent scattering coefficient is defined as the ratio of the out-going energy in any given direction to that of the incoming energy, or

$$\sigma(\Theta) = \frac{I(\Theta)}{I_{inc}} = \frac{1}{k^2} F_{1,1}(\Theta) . \tag{4.8}$$

More specifically, the backscattering coefficient is given by

$$\sigma_{\pi} = \sigma(\pi) = \frac{1}{k^2} F_{1,1}(\pi) . \tag{4.9}$$

The backscattering efficiency, Q_b, is just the backscattering coefficient divided by the cross sectional area of the (individual) particle, or

$$Q_b = \frac{\sigma_{\pi}}{\pi a^2} = \frac{1}{k^2\, \pi\, a^2} F_{1,1}(\pi) = \frac{1}{\pi x^2} F_{1,1}(\pi) . \tag{4.10}$$

where $x = ak$ is the size parameter of the particle(s) in question, and a is its equal volume sphere (or equal area sphere) radius. Q_b is a dimension less quantity.

4.2.1 Aerosol backscattering and depolarization

The aerosol backscattering ratio is defined as the ratio of the backscattering coefficient due to aerosols and air molecules over that due to the air molecules alone, or

$$S = (\sigma_\pi^P + \sigma_\pi^R)/\sigma_\pi^R \,. \tag{4.11}$$

with σ_π^P and σ_π^R being the backscattering coefficients of the aerosols and the surrounding air, respectively. It is often convenient to use the ratio of the aerosol backscattering coefficient to the molecular backscattering coefficient, denoted $S-1$, or

$$S - 1 = \sigma_\pi^P/\sigma_\pi^R \,. \tag{4.12}$$

If the mixing ratio of aerosols in the surrounding air is known then the aerosol backscattering ratio at a given wavelength and height z is given by

$$S_\lambda(z) = \frac{\sigma_{\lambda,\pi}^P\, n_P(z)}{\sigma_{\lambda,\pi}^R\, n_A(z)} + 1 \,, \tag{4.13}$$

where $\sigma_{\lambda,\pi}^P$ and $\sigma_{\lambda,\pi}^R$ are the backscattering coefficients for the particles and the air at a given wavelength, respectively, and $n_P(z)$ and $n_A(z)$ are the number densities of particles and air molecules, respectively. With a known particle mixing ratio of 10 ppbm we have

$$\frac{n_P(z)\, m_P}{n_A(z)\, m_A} = 1 \times 10^{-8} \,, \tag{4.14}$$

where m_P and m_A are the masses of the particles and air molecules, respectively. Using this relation we can write Eq. 4.13 as

$$S_\lambda(z) = \frac{\sigma_{\lambda,\pi}^P}{\sigma_{\lambda,\pi}^R}\left(\frac{m_A}{m_P} \times 10^{-8}\right) + 1 \,. \tag{4.15}$$

For the case of Rayleigh backscattering due to the clear air we have [77]

$$\sigma_{\lambda,\pi}^R = 5.45\left(\frac{\lambda}{5.5 \times 10^{-7}}\right)^{-4} \times 10^{-24}\ \mathrm{m^2 sr^{-1}}. \tag{4.16}$$

In addition masses m_P and m_A are given by

$$m_P = \frac{4}{3}\pi a_P^3 \rho_P \quad ; \quad m_A = \frac{M_A}{N_A} . \tag{4.17}$$

where a_P is the particle equivalent radius, $\rho_P = 1 \times 10^3$ kg/m^3 is the density of the particles which is close to that of water for the case of PSCs, and $N_A = 6.02 \times 10^{23}$ mol^{-1} is Avogado's number, and $M_A = 0.02897$ kg/mol is the molar mass of air. The aerosol backscattering ratio can now be written as

$$S_\lambda(z) - 1 = \frac{C_{sca} F_{1,1}(\pi)}{21.8\pi k^2} \left(\frac{\lambda}{5.5 \times 10^{-7}}\right)^4 \times 10^{24} \left(\frac{3}{4}\frac{M_A}{\pi a_P^3 \rho_P N_A} \times 10^{-8}\right) . \tag{4.18}$$

or equivalently

$$S_\lambda(z) - 1 = \frac{3}{4}\frac{C_{sca} F_{1,1}(\pi) M_A}{21.8\pi^2 k^2 a_P^3 \rho_P N_A} \left(\frac{\lambda}{5.5 \times 10^{-7}}\right)^4 \times 10^{16} . \tag{4.19}$$

which can be further simplified by inserting the actual numbers.

The backscatter ratio is easily measured by a lidar system. So is the total depolarization ratio which is just the ratio of the perpendicular backscatter return, R_s, to the parallel backscatter return, R_p, or $D_T = R_s/R_p$, where the wavelength subscript has been omitted. The linear depolarization, D, due to aerosols alone can be obtained from the aerosol backscattering ratio [76]

$$D = D_T \left(\frac{S_p[S_s - 1]}{S_s[S_p - 1]}\right) = \frac{R_s^P}{R_p^P} . \tag{4.20}$$

hence it is the ratio of the perpendicular backscatter return from aerosols to the parallel backscatter return from aerosols.

With a dual wavelength lidar system we can measure the above quantities at two wavelengths. From this we can study their wavelength dependence and get additional information about particle size or shape. The color ratio is defined as

$$\text{color ratio} = \sigma^{\mathrm{P}}_{\lambda_1,\pi}/\sigma^{\mathrm{P}}_{\lambda_2,\pi} , \tag{4.21}$$

where $\sigma^{P}_{\lambda_n,\pi}$ is the aerosol backscattering coefficient for a given wavelength. λ_1 and λ_2 ($\lambda_1 < \lambda_2$) are the wavelengths of the dual wavelength lidar system. Here we use a parameter α similar to the color ratio is defined by

$$(S_{\lambda_1} - 1)/(S_{\lambda_2} - 1) = (\lambda_1/\lambda_2)^{\alpha-4} . \tag{4.22}$$

where we have assumed that the aerosol backscattering ratio $(S_\lambda - 1)$ is proportional to $\lambda^{4-\alpha}$, and hence we assume that the aerosol backscatter by itself is proportional to $\lambda^{-\alpha}$. The factor 4 in the exponent is due to inverse fourth power wavelength dependence of the molecular scattering. Thus, α will describe the wavelength dependence of the aerosol backscattering cross section alone. Solving for α in the above equation yields

$$\alpha = 4 + \frac{\ln([S_{\lambda_2} - 1]/[S_{\lambda_1} - 1])}{\ln(\lambda_1/\lambda_2)} . \tag{4.23}$$

We also introduce here the co-color ratio, defined as the ratio of the linear depolarization due to aerosols that is observed with the shorter wavelength over that observed with the longer wavelength, or

$$\text{co-color ratio} = D_{\lambda_1}/D_{\lambda_2} . \tag{4.24}$$

It is often more convenient to define a similar parameter β to describe the wavelength dependence of the linear depolarization through the relation

$$D_{\lambda_1}/D_{\lambda_2} = (\lambda_1/\lambda_2)^{-\beta} . \tag{4.25}$$

Thus,

$$\beta = \frac{\ln(D_{\lambda_2}/D_{\lambda_1})}{\ln(\lambda_1/\lambda_2)} . \tag{4.26}$$

If we have an α of zero the aerosol backscatter is assumed to be wavelength independent for wavelengths between λ_1 and λ_2. A positive α means that the backscatter will increase with decreasing wavelength. When the aerosols are in the Rayleigh region for both wavelengths, the value of α is 4, describing the normal λ^{-4} dependence for this case. Similarly, a zero β value will indicate that there is no wavelength dependence of the

depolarization, whereas a positive β will indicate that the depolarization is increasing with decreasing wavelength.

4.3 Backscatter calculations

In this section results from extensive calculations of backscattering characteristics for ensembles of randomly oriented spheroidal particles are presented and discussed. The assumptions about the particles are made to mimic the conditions in PSCs, and as such follows the reasoning of Toon et al. [2, 20]. We assume that the particles have a very low absorption and a real refractive index slightly higher than that of water-ice at the wavelengths considered, 603 nm and 1064 nm, the wavelengths of the Browell [76] et al. dual lidar system.

4.3.1 Monodispersions

Figure 4.1 shows the backscatter ratio and the total depolarization for monodispersions consisting of randomly oriented spheroids of varying aspect ratio as a function of equal volume sphere particle size. The upper panel shows the backscatter ratio, $S_\lambda - 1$, at 603 nm wavelength as a function of the spherical **volume** equivalent radius. The various lines correspond to the particle aspect ratio indicated in the figure. The lower panel shows the corresponding depolarization ratio D_λ. The calculations were performed for a particle mixing ratio of 10 ppbm, a particle density of 1 gm cm^{-3}, and particle refractive index of $1.5 + i0.0$, i.e. the particles have no absorption. The refractive index for water ice at this wavelength is $1.31 + i6.06 \times 10^{-9}$ [78]. The refractive index of NAT and NAD type PSC particles has been calculated to be near 1.5 with a similarly small absorption. The backscatter ratio for spheres are included for comparison (labeled Mie). It is seen that the ensembles having mildly aspherical shape tend to display the same resonances in the backscatter ratio as do spheres, but that this effect is completely gone once the aspect ratio exceeds about 2. The ensembles with highly aspherical particles do not display the resonance features because they lack the symmetry of the spherical particles.

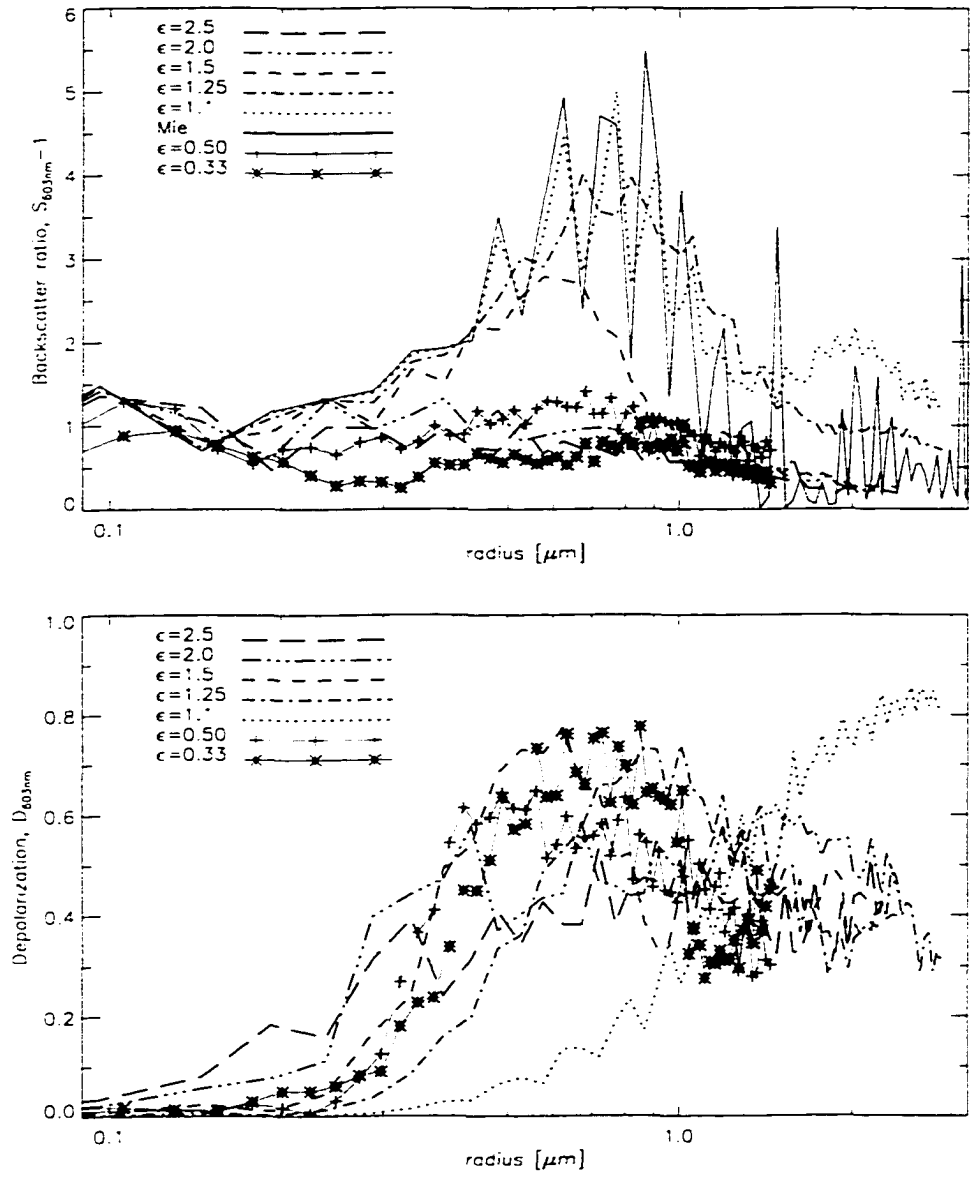

Figure 4.1. Plot of the backscatter ratio $S - 1$ and depolarization ratio D for monodispersions of randomly oriented spheroids as a function of equal volume sphere particle radius. The lidar wavelength is 603 nm, and the refractive index of the particles is $1.5 + i0.0$. The different lines correspond to different particle aspect ratios ($\varepsilon > 1$ are prolate spheroids) and are labeled in the figure.

In an ensemble of spherical particles all the particles can be said to be lined up or oriented the same way, i.e. it does not make any sense to talk about randomly oriented spheres. If the spheres in a monodispersion have a scattering resonance, or lobe, in some direction for a certain wavelength, particle size, and direction of propagation of the incoming light, then the scattered light from all the spheres in the ensemble will add up in this direction and give a peak in the phase function of the ensemble. With non-spherical particles this is not so because in an ensemble with randomly oriented non-spheres, peaks in the phase function will not add up in the same direction. This is why ice-clouds scatter more to the side than water clouds. The influence of the shape on the backscatter depolarization (the lower panel) is also interesting. The more aspherical particles show significant depolarization for smaller particles, but even nearly spherical particles can have very high depolarization. In fact, the highest depolarization values are seen for the particles with $\varepsilon = 1.1$. Note also that the "saturation" depolarization value, i.e. the value around which the depolarization seems to fluctuate once it has reached a significant zero value, is about 0.5 for all the shapes except the nearly spherical ones.

Figure 4.2 shows plots of the same quantities as in Figure 4.1 but now for the lidar wavelength 1064 nm. We again consider a monodispersion with a real refractive index of 1.5. Aside from the backscatter ratio being higher and the oscillations more pronounced because of the decrease in the contribution from the background air molecules at this wavelength, the plot is similar to the previous one but shifted to the right. Again we see that particles with aspect ratio greater than about 2 do not yield high backscatter ratios compared to the ones closer to spherical shape.

In Figure 4.3 the results from Figure 4.1 and Figure 4.2 are used to calculate the parameters α and β, i.e. the wavelength dependence of the backscatter ratio and depolarization, respectively. The wavelength dependence of the backscatter ratio is positive, or increasing with increasing wavelength for the smaller particles, but tends towards zero or negative for the larger ones. This corresponds to the location of the "hump" in the two previous figures. As expected, the α values for the least aspherical particles are

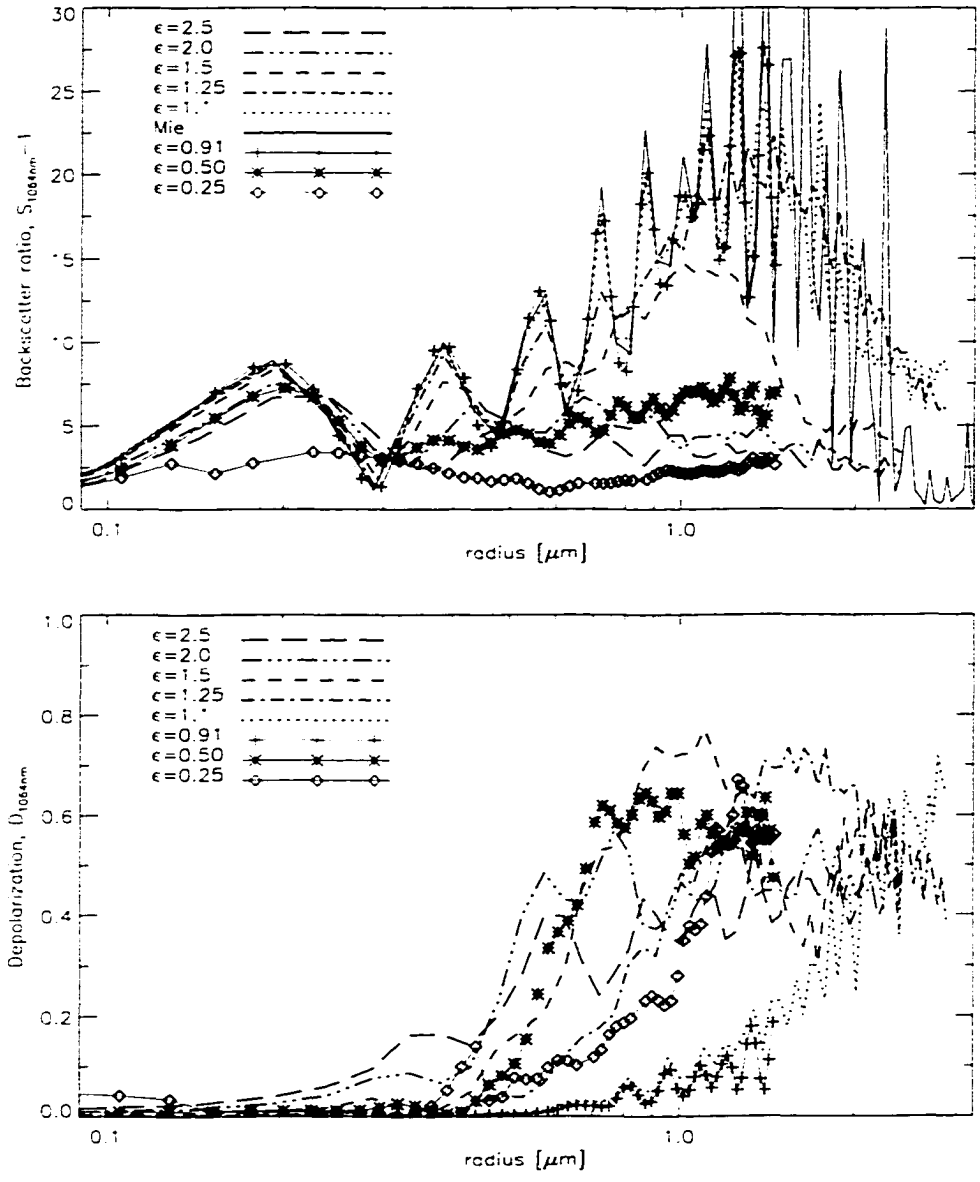

Figure 4.2. Plot of the backscatter ratio $S - 1$ and depolarization ratio D for monodispersions of randomly oriented spheroids as a function of equal volume sphere particle radius. The lidar wavelength is 1046 nm. and the particles have a real refractive index of 1.5. The different lines correspond to different particle aspect ratios ($\varepsilon > 1$ are prolate spheroids) and are labeled in the figure.

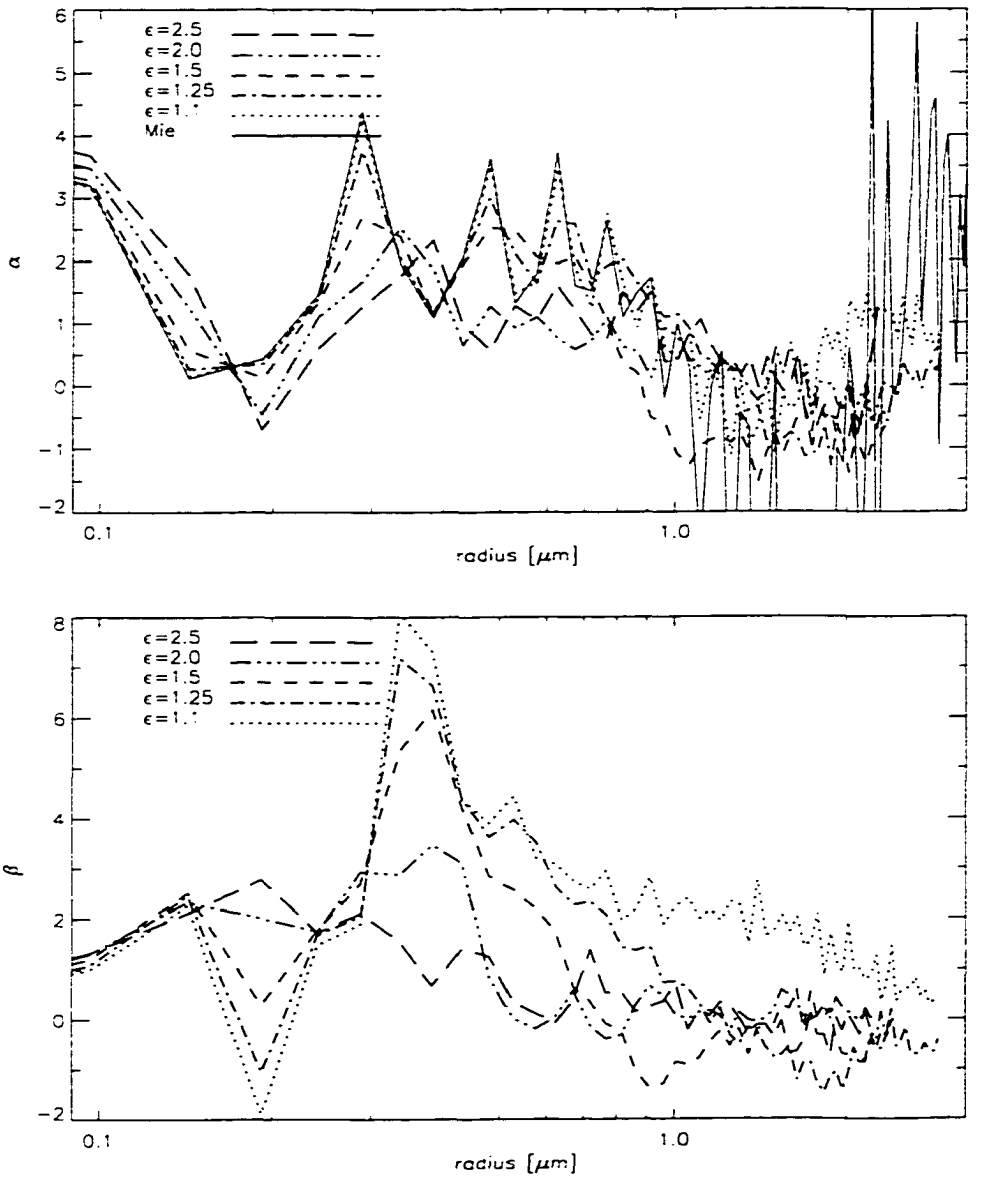

Figure 4.3. Plot of the parameter α (upper panel) and β (lower panel) as a function of equal volume sphere particle size for monodispersions of randomly oriented spheroids. The different lines corresponds to different particle aspect ratios as indicated in the figure. The two lidar wavelengths used to calculate the plot are 603 nm and 1064 nm. The particles have a real refractive index of 1.5.

oscillating more than what is the case for the most aspherical particles. Unfortunately it is impossible to determine the shape or size of particles from the α values alone: some additional information is necessary. The value of β has a pronounced peak for mildly aspherical particles with an equivalent radius of about $0.4\mu m$. Looking at the previous two figures we conclude that this behavior is due to the significant depolarization at 603 nm wavelength. whereas the same particles have very little depolarization at 1064 nm.

There are some differences between our results and those of Toon et al. [20]. These differences are largely due to the finer spacing of the data-points in our figures. The results obtained here as well as those reported in Ref. [20] differ significantly from the ones in Ref. [2]. This discrepancy is due to the scattering code used in [2], which was an early implementation of the EBCM that was run in single precision mode in an effort to find general trends rather than high precision numbers.

4.3.2 Polydispersions

It is highly unlikely that a PSC would consist solely of identical particles. It is therefore desirable to base theoretical modeling on a cloud consisting of particles with a more realistic size distribution. or size-shape distribution. Although it is difficult to determine the size-shape distribution accurately, theoretical studies [15] have shown that even a small variability in the particle size and/or shape of a scattering particle ensemble tend to smear out conspicuous features in the phase function that are often present in results based on monodispersions. In the case of lidar backscattering, these features show up as an oscillating behavior of the calculated backscattering coefficient which reveals itself also in the backscatter ratio and the color ratio. Since the absorption by PSC particles is generally believed to be small, the predominant source of the scattered field will be due to the discontinuity of the real part of the refractive index across the particle surfaces. The absorption should nonetheless be included, but the size of the spheroids should be specified in terms of their equal **area** sphere radius rather than their equal **volume** sphere radius as the surface area will be a main factor in determining the scattering

properties. Since the particles are in any case small, the effect of specifying the particle size one way or the other will not be great.

Figure 4.4 shows the results of calculations of the same quantities as in Figure 4.1 but now for a size-shape distribution of randomly oriented spheroids (solid lines) as a function of equal **area** sphere radius. The particles now have a small imaginary part (absorption) in the refractive index of 6.1×10^{-9}. The size-shape distribution is a combination of a power-law size distribution with an effective variance of 0.1, and a equiprobability shape distribution with a 5% variation in the aspect ratio ε in 5 bins centered around the mean aspect ratio given in the figure. The two distributions are combined in such a way that the smaller particles are the least non-spherical, a feature often observed in nature. We note that introducing ensembles of size-shape distributions of slightly absorbing randomly oriented prolate spheroids (specified in terms of equal area sphere radius) changes the backscattering characteristics significantly compared to a monodispersion. Our tests show that the difference is almost completely due to the introduction of a size-shape distribution and not due to the added absorption. The linear depolarization becomes significant for smaller effective particle radius as expected because the distributions contain particles that are larger than the effective radius. Other than that, the effect of particle size-shape distributions on the linear depolarization seems to be to blend and smear out features obtained for the monodispersions. The oscillating behavior of the backscatter ratio $S - 1$ due to resonances revealed in the case of monodispersions has been smeared out and is less evident in the case of polydispersions. The "saturation" depolarization is again about 0.5 as expected. It seems that a measured depolarization other than 0.5 is what will give us a reasonable chance of using the depolarization for retrieving information about particle size and/or shape.

Figure 4.5 is similar to Figure 4.4 except that we have used the lidar wavelength of 1064 nm in this case. Mishchenko et al. [70, 71] also noted that even slight deviations from spherical shape can lead to significant depolarization and values far greater than 0.5. This suggests that type 1b PSC particles, which lead to insignificant depolarization,

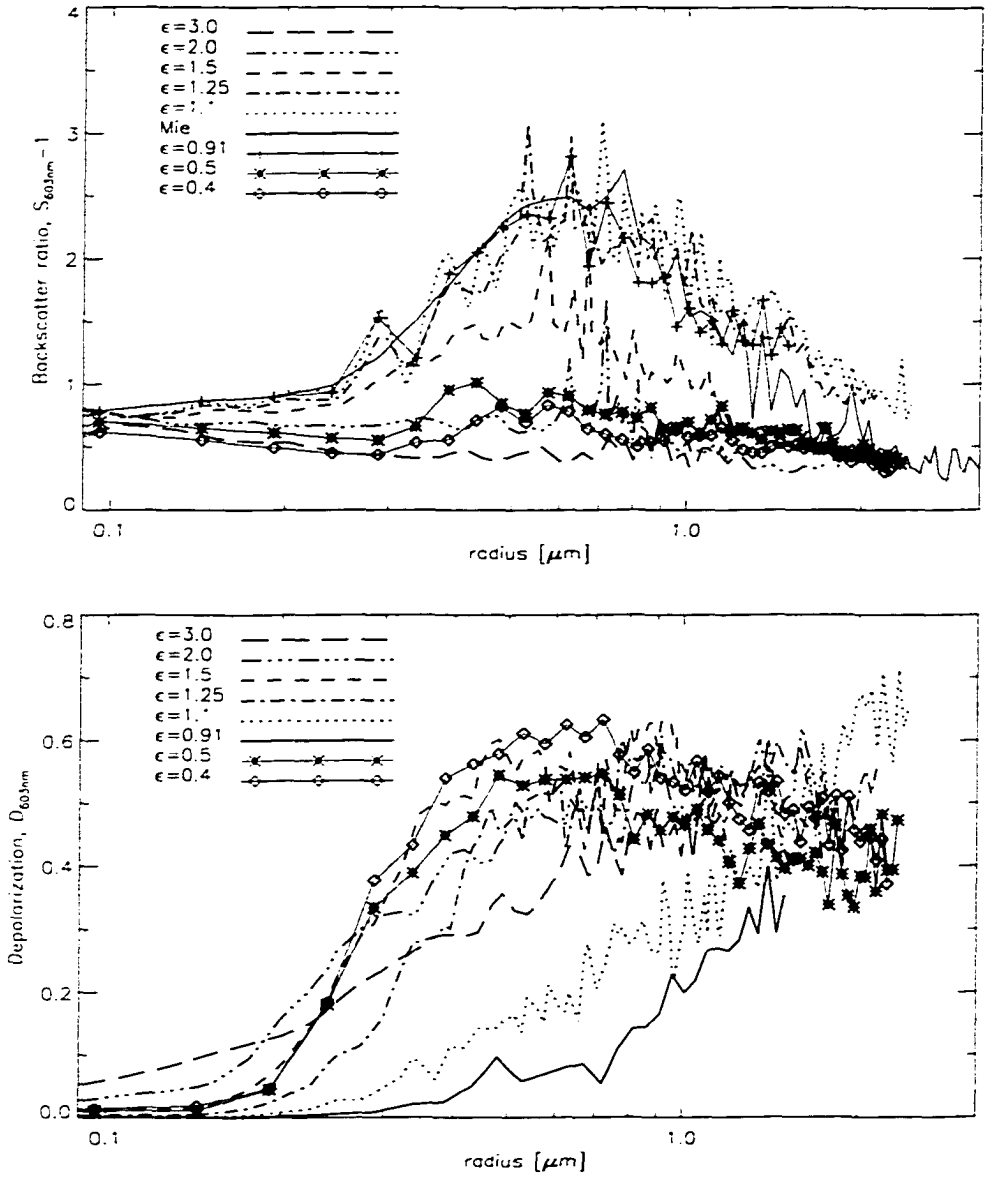

Figure 4.4. Plot of the backscatter ratio $S - 1$ and depolarization ratio D for polydispersions of randomly oriented spheroids as a function of equal area sphere particle radius. The lidar wavelength is 603 nm, and the refractive index of the particles is $1.5 + i6.1 \times 10^{-9}$. The different lines correspond to different particle aspect ratios ($\varepsilon > 1$ are prolate spheroids) and are labeled in the figure.

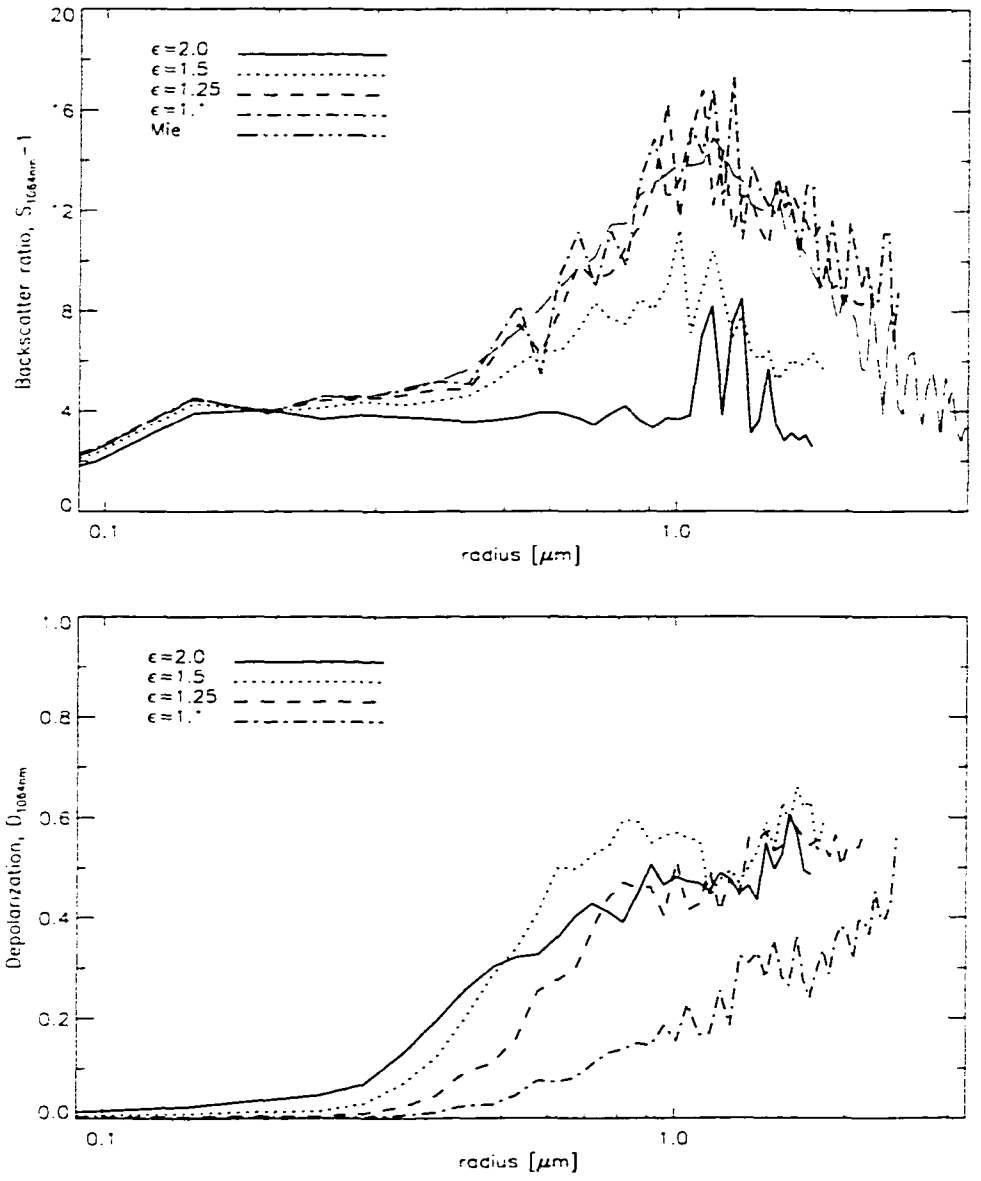

Figure 4.5. Plot of the backscatter ratio $S-1$ and depolarization ratio D for polydispersions of randomly oriented prolate spheroids as a function of equal area sphere particle radius. The lidar wavelength is 1064 nm, and the refractive index of the particles is $1.5+i6.1\times10^{-9}$. The different lines correspond to different particle aspect ratios ($\varepsilon > 1$ are prolate spheroids) and are labeled in the figure.

most likely are almost completely spherical in shape, or, they are smaller than about 0.3μm. They must certainly have an aspect ratio less than $\varepsilon = 1.1$. A third possibility is that these particles consist of (spherical) droplets with crystalline inhomogeneities inside them. Our model can not as yet be used for studies of such particles.

In Figure 4.6 we have plotted the α and β parameter using the results of Figures 4.4 and 4.5. The parameter β, and so also the co-color ratio, is particularly sensitive to particle size. Note how the maximum β values are obtained for effective equal area sphere particle radius between 0.2μm and 0.5μm for the lidar wavelengths considered here. For the shorter of the two wavelengths, the scattering particles are in the resonance region and will therefore give strong backscatter depolarization even for mildly aspherical particles, whereas the scattering mechanism for the longer wavelength is still dominated by Rayleigh type scattering. One could say that the shorter wavelength can be used to reveal the shape of the particles whereas the longer one can not. Also it appears that the height of the peak in the plot for β depends on the mean particle asphericity. The co-color ratio, and β, is therefore a useful indicator of both PSC particle size and shape. For example, type 1b PSCs will have have high α values, but β values close to 0 (or undefined). Similarly, a small α value (less than about 0.5 in our modeled case) and a β value less than about 1 will indicate particle distributions with typical size parameters larger than 10 (or about 1.0 μm in this case). To discern type 1b PSCs from type 1c PSCs, and to establish the size of type 1c PSCs, the parameter β should be especially useful since the value of β varies significantly with size in the region of interest.

In Ref. [20] Toon et al. divided the possible lidar returns from PSCs into four categories as summarized in the Table 4.1. We see that, with the exception of the last category, this schemes follows in a straightforward manner from the plots of $D_{\lambda_{632}}$ and $D_{\lambda_{1064}}$. The argument for the last assertion is as follows: In a mixed cloud with a majority of small spherical particles and a few large non-spherical particles, the backscatter ratio $S_{603} - 1$ will be reasonably high for smaller particles, but very small for the larger ones (Fig. 4.4, upper panel), whereas $S_{1064} - 1$ will be comparable for both (Fig. 4.5, upper

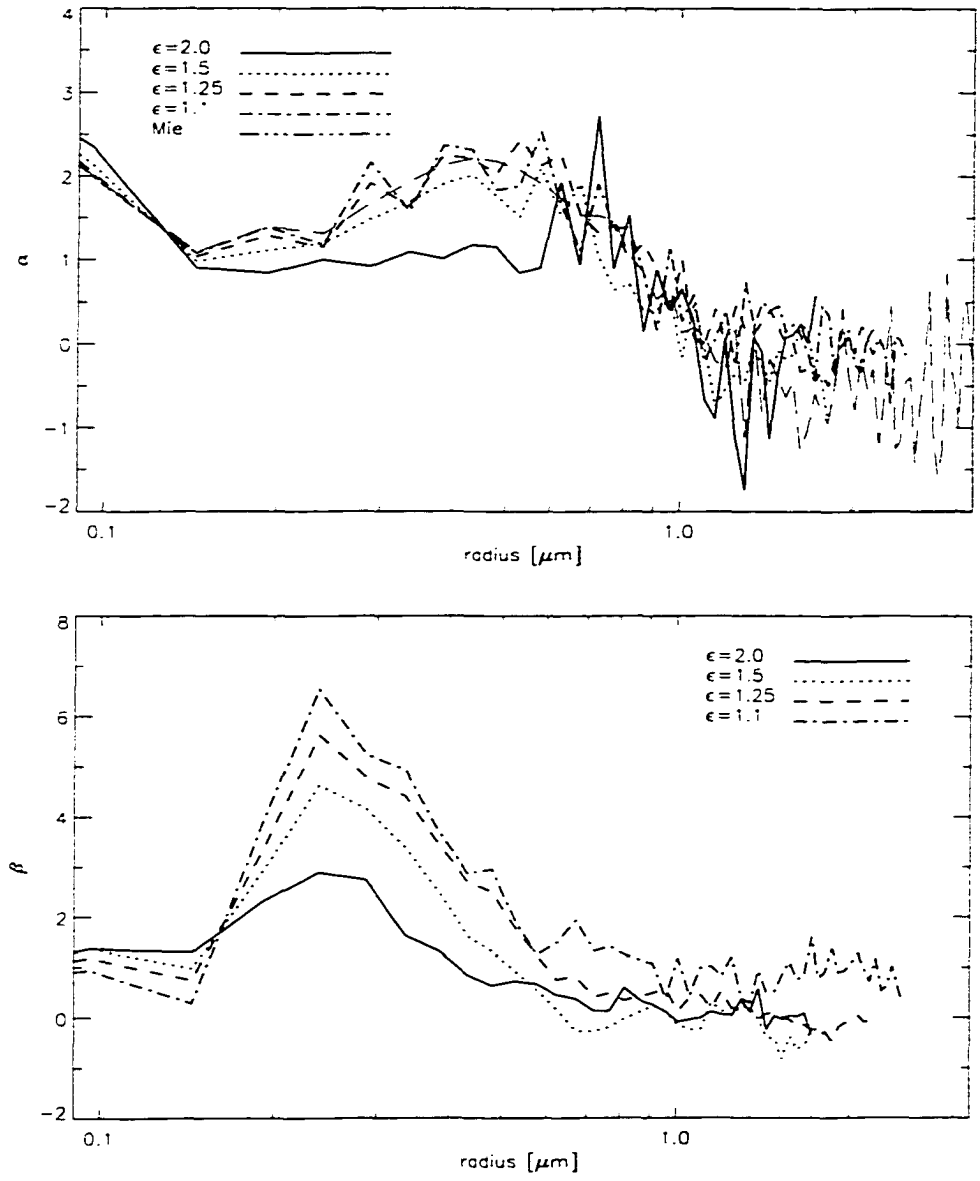

Figure 4.6. Plot of the parameter α (upper panel) and β (lower panel) as a function of equal area sphere particle size for polydispersions of randomly oriented spheroids. The different lines corresponds to different particle aspect ratios as indicated in the figure. The two lidar wavelengths used to calculate the plot are 603 nm and 1064 nm. The particles have a real refractive index of $1.5 + i6.1 \times 10^{-9}$.

Table 4.1. PSC lidar return classification scheme.

$D_{\lambda=603}$	$D_{\lambda=1064}$	Particle Type
$\leq 2\%$	$\leq 2\%$	spheres
$> 2\%$	$> 2\%$	large non-spheres
$> 2\%$	$\leq 2\%$	small non-spheres
$\leq 2\%$	$> 2\%$	spheres mixed with large non-spheres

panel). Hence, the larger particles will account for only a small part of the backscatter at the visible wavelength, but a significant part at the infrared wavelength. The amount for depolarized light returned at the visible wavelength will therefore be small relative to the total return, whereas the amount of depolarized light returned at the infrared wavelength will be substantial.

If we can assume that PSC particles are either spherical or far from spherical (i.e. $\varepsilon \geq 2$) then, referring to the plots for D_{603} and D_{1064}, since the "saturation" depolarization value of about 0.5 is reached very quickly, we can postulate that any lidar returns with depolarization $10\% < D_\lambda < 40\%$ is likely to be from a mixed type cloud. If this is the case then mixed type PSCs are much more common than previously thought [20]. If, on the other hand, non-spherical PSC particles are typically only mildly aspherical, or if liquid PSC particles with solids inside them are common, then it is hard to distinguish between mixed type clouds and homogeneous clouds, unless we have a case as described above. This is because the mildly aspherical particles are seen to slowly increase their ability to depolarize light with size, and so no marked transition from low or no depolarization to a "saturation" depolarization value is seen.

4.4 Modeling lidar signal propagation in the atmosphere

We study an idealized case in which an otherwise clear sky has a cloud consisting of ice particles in the upper atmosphere. If we assume that the beam divergence of the pulsed laser is such that the beam FWHM spot size is much larger than the area covered by the field of view of the receiver, we can consider that part of the sky which is seen from the receiver to be uniformly illuminated. Since we are interested only in the direct backscatter, we conclude from symmetry considerations that we may use a radiative transfer code for a plane parallel, vertically inhomogeneous atmosphere to model the backscatter from each LIDAR bin. The laser light propagates upwards without changing its initial polarization, but is exponentially attenuated by the accumulative optical depth of the atmosphere. The receiver has a finite temporal sampling resolution which determines the vertical spatial resolution of the LIDAR system. Each vertically resolved segment is called a bin and has a typical length of about 100 m. For each of the bins we can compute the Stokes vector in the backscatter direction using the vector radiative transfer model. For bins with no cloud the resulting Stokes vector for the scattered light is due solely to Rayleigh scattering molecules. One does not expect such a layer to depolarize the incident beam unless one accounts for multiple scattering and/or the slight anisotropy (deviation from perfect dipoles) of the molecules in the air. This is accounted for in our model.

A modeled LIDAR profile is shown in Figure 4.7. There is a cloud between 10 and 11 km in which each 100 meter bin has an optical depth of 10 times that of the same bin without cloud. For the 100 meter bin centered at 1050 m $\tau_{cloud} = 4.46 \times 10^{-3}$ whereas $\tau_{clear} = 4.46 \times 10^{-4}$. The total optical depth of the cloud is about 0.04, i.e. a sub-visible, or barely visible, cirrus cloud. The clear sky optical depths were calculated using the 1976 US Standard Atmosphere. The scattering matrix is calculated as above. In Figure 4.7 we used the Stokes scattering matrix for monodispersions of prolate spheroids with an equal area sphere radius of $0.527\mu m$ and aspect ratio $\varepsilon = 1.1$ (dotted lines) and $\varepsilon = 1.1$ (dashed lines). The refractive index of the particles is again $1.5 + i0.0$, and the

wavelength is 0.603μm. From the modeled values the linear depolarization ratio, D, in the cloud is found to be $D_{\varepsilon=1.1} = 0.04$ for the cloud consisting of particles with aspect ratio 1.1, and $D_{\varepsilon=1.5} = 0.6$ for the cloud consisting of particles with aspect ratio 1.5. Since the Stokes scattering matrix used as input for the calculations was calculated using the code described in the previous sections, the differences in the results must be due to the effect of multiple scattering and propagation in the model atmosphere. Note that we get a small depolarization from the clear sky segments of the order of 0.03% in the lower atmosphere. This is due to the finite lidar bin height and multiple scattering included in the model and is also observed in real lidar measurements.

4.5 Conclusions

We have performed calculations of the backscattering properties of ensembles of randomly oriented spheroids. For monodispersions of particles we found small discrepancies between results obtained by Toon et al. [20] and those presented here and by other investigators. However, we find that the primary conclusions drawn in Ref. [20] are valid in spite of these differences, although our results indicate that the type 1b particles should be considered to be practically completely spherical. Extension of the calculations to particles of larger size reveals no significant new information in the backscatter. Most information seems to be in the the resonance region, specifically at size parameters between 3 and 15. This should be taken into account when designing lidar systems for specific purposes.

To model the backscattering characteristics of PSCs in a more realistic manner, we extended the calculations to include size-shape distributions of randomly oriented spheroids. These results show that features in the backscatter typical for monodisperse particle distributions, tend to be smeared out and replaced by more smooth curves when polydisperse distributions are used. In general the linear depolarization ratio from such particle ensembles tend to be around 0.5. As a consequence, for realistic size-shape distributions likely to occur in nature, retrieval of PSC particle size and shape with a

lidar system becomes difficult, especially if only one wavelength is available. However, if a dual wavelength lidar system, or a variable wavelength lidar system is available, the size and shape of nonspherical particles in a cloud can be inferred from the co-color ratio.

Using the single scattering properties found by the method above in a vector radiative transfer code, we have computed intensity and polarization patterns for ensembles of size-shape distributions of spheroids mimicking those found in cirrus clouds. Only a simple application to lidar measurements has been demonstrated here.

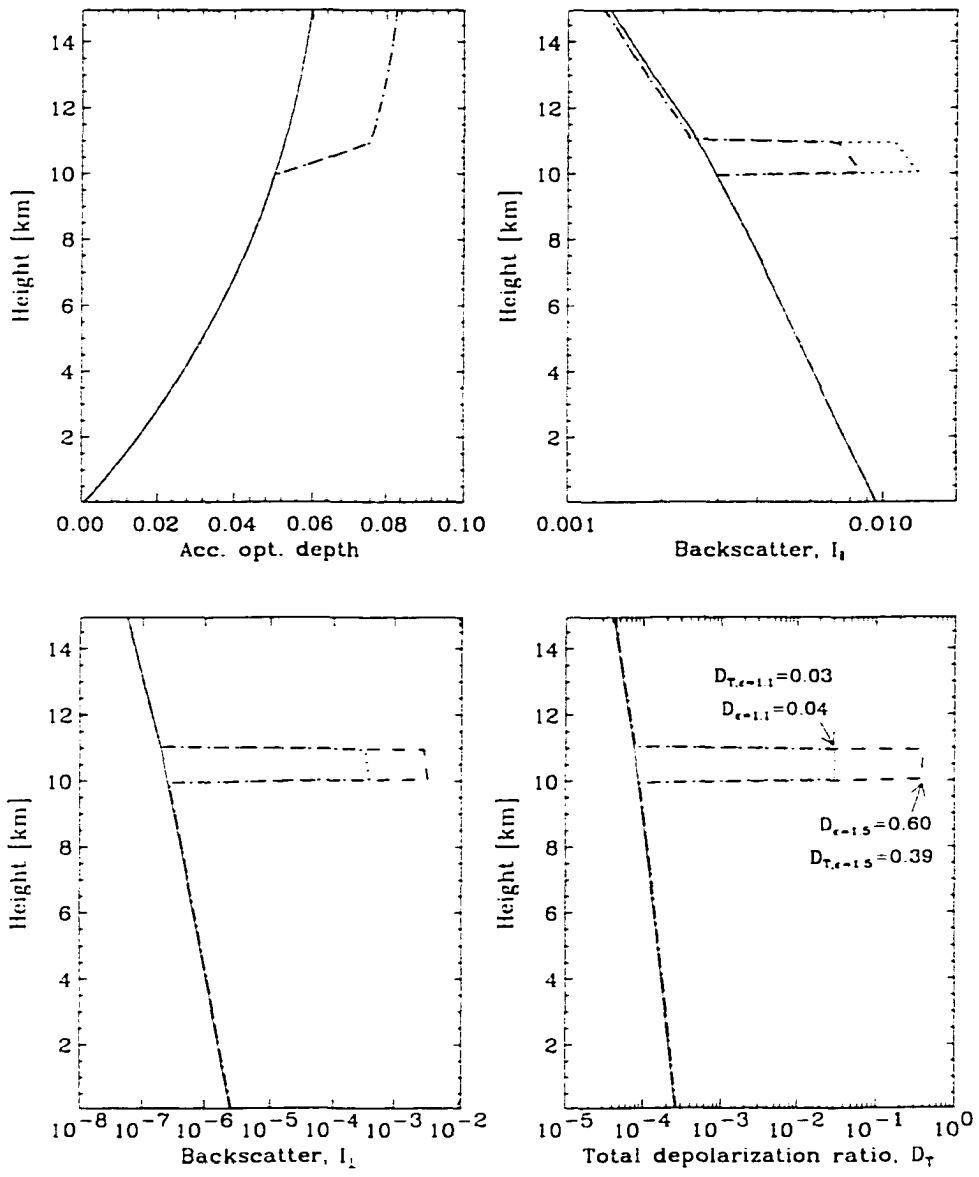

Figure 4.7. The top left panel shows the accumulative optical depth for a model atmosphere with a strato-cirrus cloud between 10 and 11 km. The solid line is for the clear sky case (USSA-76). The dotted and dash-dotted lines are for monodispersions of randomly oriented spheroids with aspect ratio $\epsilon = 1.1$ and $\epsilon = 1.5$, respectively. The parallel and perpendicular relative backscatter signal is shown in the upper right and lower left panels, respectively. The resulting total depolarization profile is shown in the lower right panel with the numbers for D_T and D of the cloud indicated in the figure.

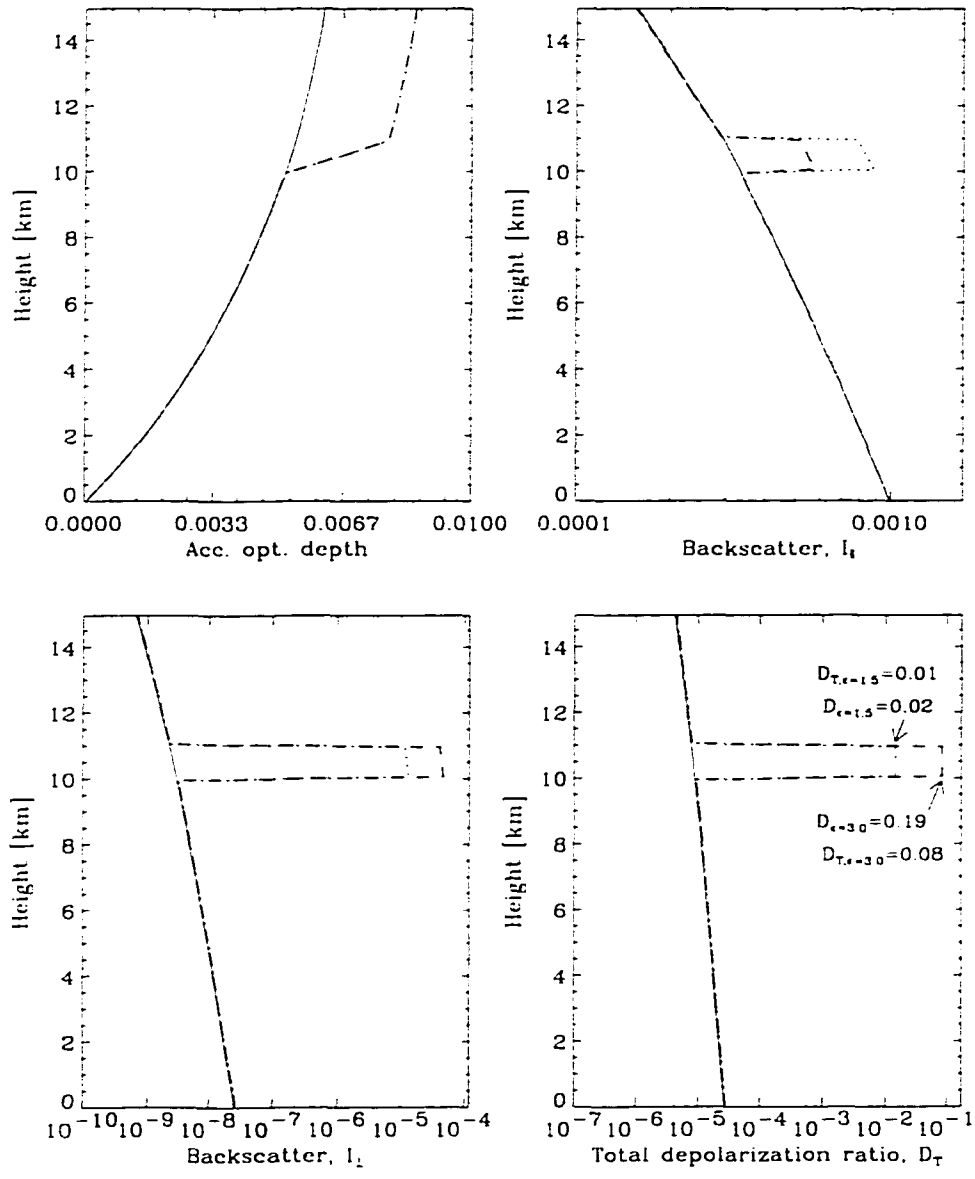

Figure 4.8. The top left panel shows the accumulative optical depth for a model atmosphere with a strato-cirrus cloud between 10 and 11 km. The solid line is for the clear sky case (USSA-76). The dotted and dash-dotted lines are for size-shape distributions of randomly oriented spheroids with aspect ratio $\varepsilon = 1.1$ and $\varepsilon = 2.0$, respectively. The wavelength of the lidar is 1064 nm, the particles have an effective equal area sphere radius of $0.528\mu m$, and their refractive index is $1.5 + i0.0$. The parallel and perpendicular relative backscatter signal is shown in the upper right and lower left panels, respectively. The resulting total depolarization profile is shown in the lower right panel with the numbers for D_T and D of the cloud indicated in the figure.

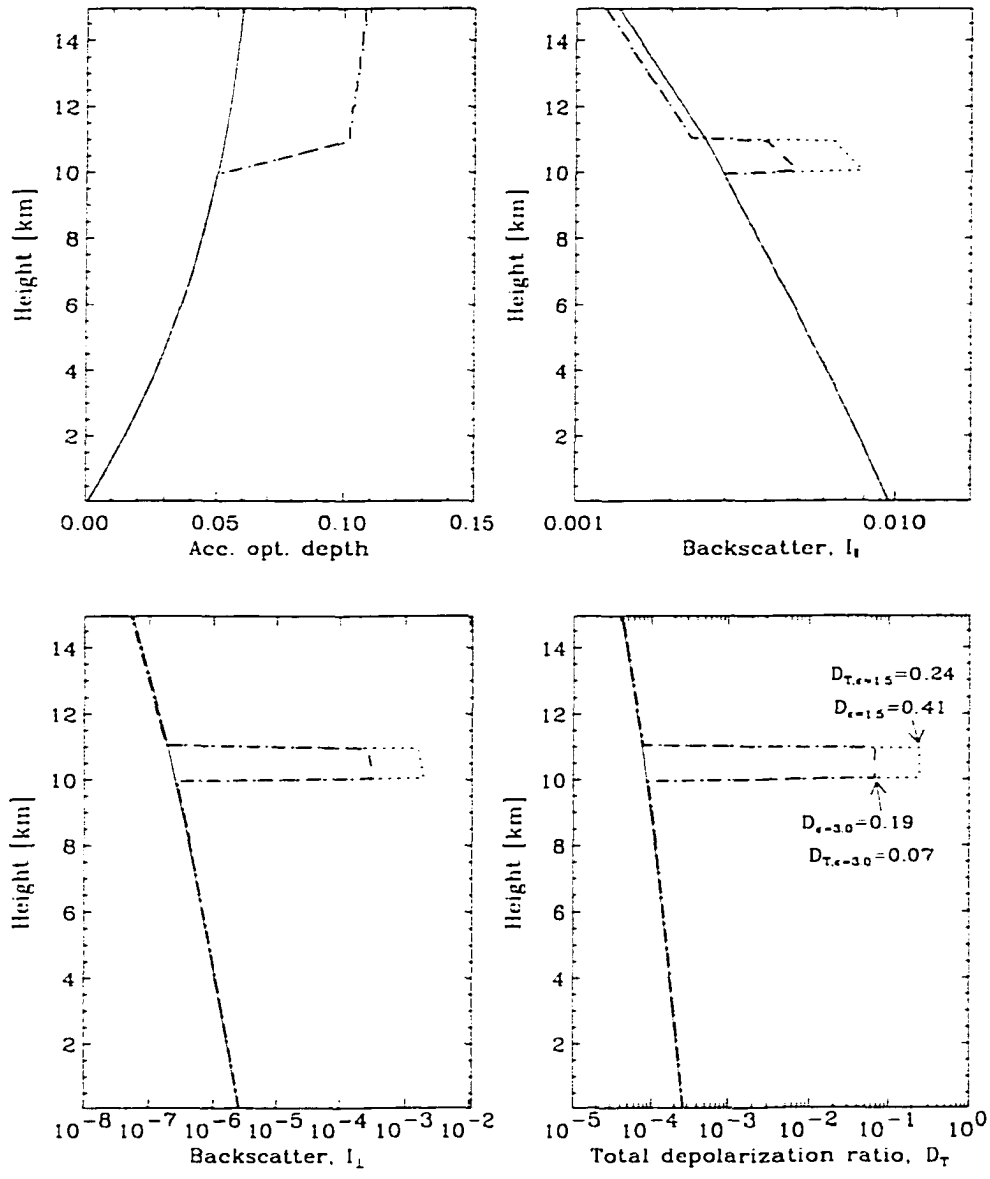

Figure 4.9. The top left panel shows the accumulative optical depth for a model atmosphere with a strato-cirrus cloud between 10 and 11 km. The solid line is for the clear sky case (USSA-76). The dotted and dash-dotted lines are for size-shape distributions of randomly oriented spheroids with aspect ratio $\varepsilon = 1.5$ and $\varepsilon = 3.0$, respectively. The wavelength of the lidar is 603 nm, the particles have an effective equal area sphere radius of $0.49\mu m$, and their refractive index is $1.4 + i1.01 \times 10^{-6}$. The parallel and perpendicular relative backscatter signal is shown in the upper right and lower left panels, respectively. The resulting total depolarization profile is shown in the lower right panel with the numbers for D_T and D of the cloud indicated in the figure.

Chapter 5

Summary

We have developed a new comprehensive model for solving electromagnetic scattering problems involving spheroidal particles. The model starts by rigorously solving the single scattering problem for a single spheroidal particle using the Separation of Variables Method (SVM). The Helmholtz equation is separable in the spheroidal coordinate system. Thus, in the SVM one starts out by separating the wave equation in the three orthogonal components: the radial, the angular, and the azimuthal. Next one proceeds by finding the solution of the Helmholtz equation for each of these orthogonal components. These solutions yield the expansion coefficients needed for expanding the incident and internal fields in terms of the product of the spheroidal basis functions. By matching the fields incident on the particle with the fields in the interior of the particle on the particle surface subject to boundary conditions, one obtains expressions for the coefficients relating the incident field to the scattered field.

The exact solution of the Helmholtz equation is expressed in terms of eigenfunctions series that depends on the size and shape as well as composition of the spheroidal particle. To calculate the eigenfunctions one first needs to find the eigenvectors, or coefficients, of the expansion. Traditionally this involved finding an initial estimate of the eigenvalues, and then using a method based on recurrence relations, infinite continued fractions, and a variational procedure. A major draw-back with this approach is that it does not readily

lend itself to automatic numerical computations. This has limited the use of the SVM for scattering by spheroidal particles in the past. In this study an efficient and reliable method has been developed for computing the expansion coefficients in the eigenfunction series. The new method is based on reformulating the recurrence relation between the coefficients as an algebraic eigenvalue problem. The solution of the algebraic eigenvalue problem can be found with readily available computer algorithms. It yields not only the desired eigenvalues, but also the required expansion coefficients, or eigenvectors. The new procedure is well adapted to automatic machine computation since it requires no initial estimates of the eigenvalues. With this procedure we have greatly extended the range of validity of the SVM for spheroidal particles. In principle one can find the eigenvalues and the corresponding eigenvectors for any desired value of the spheroidal parameter c, provided one has access to resources that allow one to solve an eigenvalue problem large enough to ensure convergence of the method. This method for solving the vector Helmholtz equation is capable of covering a wide range of sizes and shapes of spheroidal particles. There remains a challenge in finding better procedures for calculating the radial spheroidal functions of the second kind for small arguments. The traditional expansions for these functions converges very slowly for small values of the radial coordinate ξ. To solve the boundary value problem we need to evaluate the radial functions of the second kind on the surface of the spheroid. The surface of a spheroid is specified by the radial coordinate ξ_0. The value of ξ_0 approaches its minimum possible value for spheroids with extreme aspect ratios. This means that spheroids with highly elongated shape represent a problem in terms of numerical computations that is not directly associated with the computations of the expansion coefficients.

Another part of the new scattering model involves calculating the $\mathcal{T}$-matrix for spheroidal particles. This $\mathcal{T}$-matrix is then transformed into the spherical coordinate system which yields the traditional T-matrix. Once the T-matrix is found in the spherical coordinate system, our scattering model proceeds by analytically calculating the ensemble-averaged single scattering optical properties for an arbitrary distribution of

randomly oriented spheroidal particles. This circumvents another problem in the conventional use of the SVM where the calculation of ensemble-averaged optical properties of size-shape distributions of randomly oriented spheroids is very inefficient and computer-time intensive. A problem with the Extended Boundary Condition Method (EBCM) has been that it becomes numerically ill-conditioned when used with particles that deviates significantly from spherical shape. The new approach to the single scattering problem therefore circumvents the disadvantages of the traditional SVM and the EBCM, while it retains the advantages of both methods. Thus, this new SVM approach allows for efficient computation of the optical properties of size-shape distributions of randomly oriented small nonspherical particles over a range of shapes unprecedented by previous methods. One can therefore, for the first time, systematically study the effect of particle shape on the single scattering optical properties over an extensive range of particle shape. If so desired, the optical properties thus found can be used as input to a vector radiative transfer model which enables us to solve the full 4-vector problem (including polarization), using the results from the single-scattering computations.

A study of the elements of the phase matrix for various distributions of randomly oriented spheroids revealed that they are strongly sensitive to a variation in the effective aspect ratio of a shape distribution. The same effect was observed for the single scattering albedo and asymmetry parameter. A variance of the effective size has somewhat less impact on the same parameters. As the width of a distribution increases, features often seen in the phase function of more uniform distributions tend to get washed out. Variation in particle shape has a greater impact on the phase functions than variation in particle size in this respect. Disk-like and needle-like, spheroids with extreme aspect ratios, have unique scattering properties in that they tend towards features observed for particles in the Rayleigh regime. This result may have important implications for remote sensing and optical particle sizing.

To test the new method in an application to atmospheric scattering, we modeled the backscattering characteristics of Polar Stratospheric Clouds (PSCs). Comparison

with results for similar computations presented in Ref. [20] revealed small differences for monodispersions that were ascribed to difference in sampling density in the resonance region. The primary conclusions drawn in Ref. [2] are valid in spite of these differences. although our results indicate that the type 1b PSC particles should be considered to be practically completely spherical. Extension of the calculations to particles of larger size revealed no significant new information in the backscatter. Most information seems to be in the resonance region, specifically at size parameters between 3 and 15. This should be taken into account when designing lidar systems for specific purposes. When modeling the backscattering characteristics of PSCs the calculations should be performed on size-shape distributions of randomly oriented spheroids. Our results show that features in the backscatter typical for monodisperse particle distributions, tend to be smeared out and replaced by more smooth curves when polydisperse distributions are used. In general the linear depolarization ratio from such particle ensembles tend to be around 0.5. As a consequence, for realistic size-shape distributions likely to occur in nature, retrieval of PSC particle size and shape with a lidar system becomes difficult, especially if only one wavelength is available. However, with a carefully chosen dual wavelength lidar system, or a variable wavelength lidar system, the size and shape of nonspherical particles in a cloud can be inferred from the co-color ratio.

The comprehensive scattering model developed in this work has the potential of becoming the equivalent of the Mie theory for non-spherical particles. Using spheroids as a simplified shape capable of representing macroscopically averaged ensembles of individual shapes, we now have a tool to investigate the optical properties of naturally occurring ensembles of randomly oriented non-spherical particles. The advantage is that such ensembles can be accurately modeled by just adding one extra parameter to the description of the particles, namely a shape parameter. The model is not limited to particles with only mildly aspherical shapes, and it is very effective at doing ensemble averages over realistic size-shape distributions. Future applications of the model include, as briefly demonstrated here, further studies on the sensitivity of optical prop-

erties on various types of distributions of randomly oriented particles, and to develop remote sensing retrieval algorithms. Another application is the development of shape-parameterizations for modeling radiative transfer in a medium containing non-spherical particles, for example for use in climate models.

Bibliography

[1] H. A. Eide, J. J. Stamnes, K. Stamnes, and M. Schulz. New method for computing expansion coefficients for spheroidal functions. *J Quant Spect Rad Tran*, 63:191–203, 1999.

[2] O. B. Toon, E. V. Browell, S. Kinne, and J. Jordan. An analysis of lidar observations of polar stratospheric clouds. *Geophys. Research Let.*, 17:393–396, 1990.

[3] H. C. van de Hulst. *Light Scattering by Small Particles*. John Wiley & Sons, Inc., 1957.

[4] K. N. Liou and R. F. Coleman. Light scattering by hexagonal columns and plates. *Izv. Akad. Nauk SSSR Fiz. Atmos. Okeana*, 16:207–218, 1980.

[5] R. F. Coleman and K. N. Liou. Light scattering by hexagonal ice crystals. *J. Atmos. Sci.*, 39:1260–1271, 1981.

[6] W. J. Glantschnig and Sow-Hsin Chen. Light scattering from water droplets in the geometrical optics approximation. *Appl. Opt.*, 20:2499–2509, 1981.

[7] Lord Rayleigh. On the incidence of aerial and electric waves upon small obstacles in the form of ellipsoids or elliptic cylinders, and on the passage of electric waves through a circular aperture in a conducting screen. *Philos. Mag.*, 44:28–52, 1897.

[8] G. Mie. Beiträge zur optik trüber medien, speziell kolloidaler metallösungen. *Ann. Phys.*, 25:377–445, 1908.

[9] K. N. Liou and Y. Takano. Light scattering by nonspherical particles: remote sensing and climatic implications. *Atmos. Res.*, 31:271–298, 1994.

[10] S. Asano and M. Sato. Light scattering by randomly oriented spheroidal particles. *Appl. Opt.*, 19:962–974, 1980.

[11] M. I. Mishchenko. Light scattering by size-shape distributions of randomly oriented axially symmetric particles of a size comparable to a wavelength. *Appl. Opt.*, 32:4652–4665, 1993.

[12] M. I. Mishchenko and L. D. Travis. Satellite retrieval of aerosol properties over the ocean using polarization as well as intensity of reflected sunlight. *J. Geophys. Res.*, 102:16,989–17,013, 1997.

[13] A. A. Lacis, J. Chowdhary, M. I. Mishchenko, and B. Cairns. Modeling errors in diffuse-sky radiation: vector *vs.* scalar treatment. *Geophys. Res. Lett.*, 25:135–138, 1998.

[14] D. L. Mitchell, A. Macke, and Y. Liu. Modeling cirrus clouds. part ii: Treatment of radiative properties. *J. Atmos. Sci.*, 53:2967–2988, 1996.

[15] M. I. Mishchenko, J. W. Hovenier, and L. D. Travis. *Light Scattering by Nonspherical Particles*. Academic Press, 2000.

[16] F. M. Schulz, K. Stamnes, and J. J. Stamnes. Scattering of electromagnetic waves by spheroidal particles: A novel approach exploiting the T-matrix computed in spheroidal coordinates. *Applied Optics*, 37:7875–7896, 1998.

[17] M. I. Mishchenko, W. B. Rossow, A. Macke, and A. A. Lacis. Sensitivity of cirrus cloud albedo, bidirectional reflectance and optical thickness retrieval accuracy to ice particle shape. *J. Geophys. Res.*, 101:16,973–16,985, 1996.

[18] M. I. Mishchenko. Light scattering by randomly oriented axially symmetric particles. *J. Opt. Soc. Am. A.*, 8:871–882, 1991.

[19] F. M. Schulz, K. Stamnes, and J. J. Stamnes. Shape-dependence of the optical properties in size-shape distributions of randomly oriented prolate spheroids, including highly elongated shapes. *J. Geophys. Res.*, 104:9413–9421, 1998.

[20] O. B. Toon, A. Azadeh, E. V. Browell, and J. Jordan. Analysis of lidar observations of arctic polar stratospheric clouds during january 1989. *J. Geophys. Res.*, 105:20589–20615, 2000.

[21] C. Niven. (no title). *Philos. Trans. A.*, 171:117, 1880.

[22] S. Asano and G. Yamamoto. Light scattering by a spheroidal particle. *Appl. Opt.*, 14:29–49, 1975.

[23] N. V. Voshchinnikov. Electromagnetic scattering by homogeneous and coated spheroids: Calculations using the separation of variable method. *J. Quant. Spectrosc. Radiat. Transfer*, 55:627–636, 1996.

[24] C. J. Bouwkamp. Theoretische en numerieke behandeling van de buiging door een runde opening. *Diss. Groningen, Groningen-Batavia*, 1941.

[25] C. J. Bouwkamp. On spheroidal wave functions of order zero. *J. Math. Phys.*, 26:79–93, 1947.

[26] J. J. Stamnes and B. Spjelkavik. New method for computing eigenfunctions (Mathieu functions) for scattering by elliptical cylinders. *Pure Appl. Opt.*, 4:251–262, 1995.

[27] E. L. Ince. (no title). *Proc. R. Soc. Edin.*, 46:20–29 and 316–322, 1925-26.

[28] E. L. Ince. (no title). *Proc. R. Soc. Edin.*, 47:294–301, 1926-27.

[29] E. L. Ince. (no title). *Proc. R. Soc. Edin.*, 52:355–362, 1931-32.

[30] P. Yang and K. N. Liou. Light scattering by hexagonal ice crystals: comparison of finite-difference time domain and geometric optics models. *J. Opt. Soc. Am. A*, 12:162–176, 1995.

[31] P. Yang and K. N. Liou. Finite-difference time domain method for light scattering by small ice crystals in three-dimensional space. *J. Opt. Soc. Am. A*, 13:2072–2085. 1996.

[32] P. Yang and K. N. Liou. Geometric-optics-integral-equation method for light scattering by nonspherical ice crystals. *Appl. Opt.*, 35:6568–6584. 1996.

[33] P. Yang and K. N. Liou. Light scattering by ice crystals of complex shapes. In *Ninth Conference on Atmospheric Radiation, Long Beach, California, February 2-7, 1997*, pages 373–377, Boston, Mass., 1997. Am. Meteorol. Soc.

[34] P. Yang and K. N. Liou. Light scattering by hexagonal ice crystals: solutions by a ray-by-ray integration algorithm. *J. Opt. Soc. Am. A*, 14:2278–2289, 1997.

[35] P. Yang, K. N. Liou, and W. P. Arnott. Extinction efficiency and single-scattering albedo for laboratory and natural cirrus clouds. *J. Geophys. Res.*, 102:21.825–21.835, 1997.

[36] P. N. Francis. Some aircraft observations of the scattering properties of ice crystals. *J. Atmos. Sci.*, 52:1142–1154, 1995.

[37] B. A. Wielicki, J. T. Suttles, A. J. Heymsfield, R. M. Welch, J. D. Spinhirne, M.-L. C. Wu, D. O'C. Starr, L. Parker, and R. F. Arduini. The 27-28 october 1986 fire ifo cirrus case study: Comparison of radiative transfer theory with observations by satellite and aircraft. *Mon. Wea. Rev.*, 118:2356–2376, 1990.

[38] M. I. Mishchenko, L. D. Travis, and D. W. Mackowski. T-matrix computations of light scattering by nonspherical particles: A review. *J. Quant. Spectrosc. Radiat. Transfer*, 55:535–575, 1996.

[39] C. Flammer. *Spheroidal Wave Functions*. Stanford University Press, 1957.

[40] M. Abramowitz and I.A. Stegun. *Handbook of Mathematical Functions*. Dover, 1965.

[41] B. P. Sinha, R. H. MacPhie, and T. Prasad. Accurate computation of eigenvalues for prolate spheroidal wave functions. *IEEE Trans. Antennas Propagat.*, 21:406–407. 1973.

[42] B. P. Sinha and R. H. MacPhie. On the computation of the spheroidal vector wave functions of the second kind. *J. Math. Phys.*, 16:2378–2381. 1975.

[43] J. Meixner and F. W. Schäfke. *Mathieusche Funktionen und Sphäroidfunktionen.* Springer-Verlag, Berlin, 1954.

[44] G. Blanch. (no title). *J. Math. Phys.*, 25:11, 1946.

[45] Wang Qinan, Chen Kiang, and Ou Yang Zi Xiang. Some keys to an accurate computation for the separation of variables method in the scattering theory. *J. Nanjing University*, 1997.

[46] E. Anderson, Z. Bai, C. Bischof, J. Demmel, J. Dongarra, J. Du Croz, A. Greenbaum, S. Hammarling, A. McKenney, S. Ostrouchov, and D. Sorensen. *LAPACK Users Guide, 2nd ed.* Society for Industrial and Applied Mathematics, 1995.

[47] S. Hanish, R. V. Baier, A. L. van Buren, and B. J. King. *Tables of Radial Spheroidal Wave Functions*, volume 1-6. Naval Research Laboratory, 1970.

[48] A. L. Van Buren, B. J. King, R. V. Baier, and S. Hanish. *Tables of Angular Spheroidal Wave Functions*, volume 1-2. Naval Research Laboratory, 1975.

[49] A. L. Van Buren, R. V. Baier, and S. Hanish. A Fortran computer program for calculating the oblate spheroidal radial functions of the first and second kind and their first derivatives. Technical report, Naval Research Laboratory, 1970.

[50] B. J. King, R. V. Baier, and S. Hanish. A Fortran computer program for calculating the prolate spheroidal radial functions of the first and second kind and their first derivatives. Technical report, Naval Research Laboratory, 1970.

[51] B. J. King and A. L. Van Buren. A Fortran computer program for calculating the prolate and oblate angle functions of the first kind and their first and second derivatives. Technical report, Naval Research Laboratory, 1970.

[52] C. Flammer. *Spheroidal Wave Functions*. Stanford University Press, 1957.

[53] P. C. Waterman. Matrix formulation of electromagnetic scattering. *Proc. IEEE*, 53:805–812, 1965.

[54] P. C. Waterman. Symmetry, unitarity, and geometry in electromagnetic scattering. *Phys. Rev. D*, 3:825–839, 1970.

[55] P. Barber. *Differential scattering of electromagnetic waves by homogeneous isotropic dielectric bodies*. PhD thesis, University of California, Los Angeles, 1973.

[56] P. Barber and C. Yeh. Scattering of electromagnetic waves by arbitrarily shaped dielectric bodies. *Appl. Opt.*, 14:2864–2872, 1975.

[57] P. C. Waterman. Matrix methods in potential theory and electromagnetic scattering. *J. Appl. Phys.*, 50:4550–4566, 1979.

[58] M. I. Mishchenko and L. D. Travis. Light scattering by polydispersions of randomly oriented spheroids with sizes comparable to wavelengths of observation. *Appl. Opt.*, 33:7206–7225, 1994.

[59] M. I. Mishchenko, L. D. Travis, and A. Macke. Scattering of light by polydisperse, randomly oriented, finite circular cylinders. *Appl. Opt.*, 35:4927–4940, 1996.

[60] D. J. Wielaard, M. I. Mishchenko, A. Macke, and B. E. Carlson. Improved t-matrix computations for large, nonabsorbing and weakly absorbing nonspherical particles and comparison with geometrical-optics approximation. *Appl. Opt.*, 36:4305–4313, 1997.

[61] N. T. Zakharova and M. I. Mishchenko. Scattering properties of needle-like and plate-like ice spheroids with moderate size parameters. *Appl. Opt.*, 2000. (in press).

[62] M. I. Mishchenko. Light scattering by nonspherical ice grains: an application to noctilucent cloud particles. *Earth Moon Planets*, 57:203–211, 1999.

[63] M. I. Mishchenko and L. D. Travis. Capabilities and limitations of a current fortran implementation of the t-matrix method for randomly oriented, rotationally symmetric scatterers. *Quant. Spect. Rad. Tran.*, 60:309–324, 1998.

[64] J. W. Hovenier and C. V. M. van der Mee. Fundamental relationships relevant to the transfer of polarized light in a scattering atmosphere. *Astron. Astrophys.*, 128:1–16, 1983.

[65] J. E. Hansen and L. D. Travis. Light scattering in planetary atmospheres. *Space Sci. Rev.*, 16:527–610, 1974.

[66] M. I. Mishchenko, L. D. Travis, R. A. Kahn, and R. A. West. Modeling phase functions for dustlike tropospheric aerosols using a shape mixture of randomly oriented polydisperse spheroids. *J. Geophys. Res.*, 102:16,831–16,847, 1997.

[67] F. M. Schulz, K. Stamnes, and F. Weng. Vdisort: An improved and generalized discrete ordinate radiative transfer model for polarized (vector) radiative transfer computations. *J. Quant. Spectrosc. Radiat. Transfer*, 61:105–122, 1998.

[68] F. M. Schulz, K. Stamnes, and J. J. Stamnes. Modeling of the radiative transfer properties of media containing particles of moderately and extremely elongated shape. *Geophys. Res. Lett.*, 25:4481–4484, 1998.

[69] F. M. Schulz and K. Stamnes. Angular distribution of the stokes vector in a plane parallel, vertically inhomogeneous medium in the vector discrete ordinate radiative transfer (vdisort) model. *J. Quant. Spectrosc. Radiat. Transfer*, 1999. (in press).

[70] M. I. Mishchenko and J. W. Hovenier. Depolarization of light backscattered by randomly oriented nonspherical particles. *Optics Letters*, 20:1356–1359, 1995.

[71] M. I. Mishchenko and K. Sassen. Depolarization of lidar returns by small ice crystals: An application to contrails. *Geophys. Research Let.*, 25:309–312, 1998.

[72] K. S. Carslaw, M. Wirth, A. Tsias, B. P. Luo, A. Dörnbrack, M. Leutbecher, H. Volkert, W. Renger, J. T. Bacmeister, and T. Peter. Particle microphysics and chemistry in remotely observed mountain polar stratospheric clouds. *J. Geophys. Res.*, 103:5785–5796, 1998.

[73] T. Azadeh and O. B. Toon. The presence of metastable HNO_3/H_2O solid phases in the stratosphere inferred from ER2 data. *J. Geophys. Res.*, 101:9071–9078, 1996.

[74] J. Goodman and O. B. Toon et al. Antarctic stratospheric ice crystals. *J. Geophys. Res.*, 94:16449–16458, 1989.

[75] I. Taesler et al. Hydrogen bond studies, XCIV diaquaoxonium ion in nitric acid trihydrate. *Acta Crystallogr., Sect B*, 31:1489–1495, 1975.

[76] E. V. Browell, C. F. Botler, S. Ismail, P. A. Robinette, A. F. Carter, N. S. Higdon, O. B. Toon, M. R. Schoebert, and A. F. Tuck. Airborne lidar observations in the wintertime arctic stratosphere: Polar stratospheric clouds. *Geophys. Res. Lett.*, 17:385, 1990.

[77] E. D. Hinkley (ed). *Laser Monitoring of the Atmosphere*. Springer, 1976.

[78] S. G. Warren. Optical constants of ice from the ultra-violet to the microwave. *Appl. Optics*, 23:1206, 1984.